The Anomalous Low State of the X-ray Binary System Hercules X-1

Edward Jurua

(Msc)

This thesis is submitted in accordance with the requirement for the Degree of

Doctor of Philosophy

in the

Faculty of Natural and Agricultural Sciences,

Department of Physics

at the

University of the Free State,

South Africa.

Promoter: Prof. P.J.Meintjes

August 2008

Acknowledgments

I wish to extend my sincere gratitude and deepest appreciation to Prof. P.J. Meintjes and Dr. M. Still for their consistent guidance, critical and constructive criticisms and encouragements from their immense accumulated knowledge and experience.

I would also like to sincerely thank and appreciate Prof. P. Charles, Dr. D. Buckley and Dr. S. Potter for their valuable discussions and input into this study.

My sincere gratitude to the South African Astronomical Observatory (SAAO) for the Stobie-SALT scholarship, without which I wouldn't have been able to do this study.

I also extend my sincere gratitude and appreciation to the Mbarara University of Science and Technology and the Department of Physics, University of the Free State for their financial and moral support throughout my period of study.

Am also deeply indebted to Prof. P.J. Meintjes for his financial and moral support and fatherly guidance during my time at the University of Free State.

I also extend my heartfelt respect and deepest love to my family for their continued support and encouragement as I have persued this course of study.

Above all, I must thank the Almighty God for blessing me abundantly and providing me with everything I needed throughout my studies. *"How we praise God, the Father of our Lord Jesus Christ, who has blessed us with every blessing in heaven because we belong to Christ..."* (Ephesians 1:3).

To my Dad Erinayo E. Lebu (Late) and Mum Neria Oworu

Abstract

The lightcurve of Hercules X-1 (Her X-1) shows a peculiar 35-day modulation of the X-ray flux cycling between low and high states. The 35-day modulation is believed to result from the occultation of the neutron star by a warped precessing disc around the central neutron star. Since the discovery of the 35-day cycle of Her X-1, it has entered the anomalous low state a number of times, with the most recent being during the 2003 - 2004 period. Using RXTE ASM observations of Her X-1 after the 2003 - 2004 anomalous low state, it is shown that Her X-1 turned on with a new precession period and main-on flux. It is further shown that there is a positive correlation between the precession period and the main-on flux.

Using optical observations of Her X-1 during both the anomalous low state and the normal high state it is shown that the orbital (1.7 day) lightcurve of Her X-1 varies systematically over the 35-day precession cycle. It is also shown that there is insignificant change in the 35-day morphology of the lightcurves between the anomalous low state and normal high state of Her X-1, suggesting a very slight change in the disc warp between the two states. Comparison of optical and X-ray lightcurves suggest that the significant amount of X-ray flux during the anomalous low state originates from the companion star.

Analysis of both RXTE PCA and XMM-Newton observations of Her X-1 during the 2003 - 2004 anomalous low state, show that Her X-1 was brighter during this period compared to the normal high state brightness, and that there are two components of X-ray flux during the anomalous low state: reflection component from the companion star and coronal component from the accretion disc corona.

keywords: accretion:accretion discs - binaries:eclipsing - stars:individual (Hercules X-1)-stars:neutron-X-rays:stars - Instabilities

Opsomming

Die ligkurwe van Hercules X-1 (Her X-1) toon ‘n sonderlinge 35-dae sikliese modulasie van die X-straal vloed tussen hoë en lae toestande. Die 35-dae modulasie (presessie periode) is waarskynlik die resultaat van die okkultasie van die neutron ster duer ’n verwronge akresie skyf die sentrale neutron ster. Sedert die ontdeking van die 35-dae siklus van Her X-1, het dit vier keer sodanige toestand getoon, met die mees onlangse gedurende die 2003 - 2004 periode. Deur gebruik te maak van RXTE ASM data van Her X-1 na die 2003 - 2004 onreëlmatige lae toestand, is aangetoon dat Her X-1 aangeskakel het met ‘n nuwe pressesie periode en hoof-aan teltempo. Daar word verder gewys dat daar ‘n positiewe korrelasie is tussen die pressesie periode en die hoof-aan tempo.

Deur gebruik maak van optiese data van Her X-1 gedurende die oneëlmatige lae toestand en die normale hoë toestand is aangetoon dat die orbitale (1.7 dae) ligkurwe van Her X-1 sistematies varieer oor die 35-dae pressesie periode. Daar is ook aangetoon dat daar ‘n onbeduidende verandering in die 35-day morfologie van die ligkurwe tussen die onreëlmatige lae en normale hoë toestand is, wat ‘n baie klein verandering in die skyf verwronging tussen die twee toestande impliseer. Vergelyking tussen die optiese en X-straal ligkurwes toon ann dat ‘n beduidende fraksie van die X-straal vloed gedurende die onreëlmatige lae toestand vanaf die sekondêre ster afkomstig is.

Analise van RXTE PCA en XMM-Newton data van Her X-1 gedurende die 2003 - 2004 onreëlmatige lae toestand toon aan dat Her X-1 helderder was gedurende hierdie periode in vergelyking met die normale hoë toestand; asook dat daar twee kompnente van die X-straal vloed is gedurende die oneëlmatige lae toestand: ‘n weerkaatsing komponent vanaf die sekondêre ster, en ‘n komponent vanaf die akkresie skyf korona.

Sluetel terme: akkresie: akkresie skyf - binêre stelsels: eklipties - sterre: indeviduel (Hercules X-1) - sterre: neutron - X-strale: sterre - onstabiliteit

Contents

List of Figures

List of Tables

Chapter 1

Introduction

Since the discovery of Hercules X-1 (Her X-1) (Tananbaum, 1972), the number of X-ray binary systems that display super-orbital periods have increased. The super-orbital period is believed to be due to the precession of a warped/tilted accretion disc around the compact object (Gerend & Boynton, 1976; Petterson, 1977; Katz, 1980; van den Heuvel, Ostriker & Petterson, 1980; and Kumer, 1986). Warped precessing discs are also observed in other astronomical objects, e.g. the precessing jets produced from Active Galactic Nuclei (AGNs) and Young Stellar Objects (YSOs) (Krolik, 1999; Reipurth & Bally, 2001; and Fender, 2003) are attributed to the precession of warped/tilted accretion discs.

The main focus of this thesis is the study of the anomalous low state of Her X-1 which is believed to result from a change in the disc shape or warp. A brief discussion of these concepts will be presented later. Her X-1 is both nearby ~ 6 kpc (i.e. bright) and above the Galactic plane by ≥ 3 kpc (i.e. there is low quantity of Galactic gas along the line of sight)(Vrtilek et al., 2001). It is an X-ray binary of which the masses of the stellar components are known and it emits over the entire electromagnetic spectrum. With this combination, Her X-1 is one of the best studied X-ray binaries and is an extremely valuable source for warped precessing accretion disc studies. The properties and mechanisms responsible for disc warping in astronomical environments will

be discussed later in Chapter 3. In the following sections the general properties of X-ray binaries and mass transfer/accretion are discussed briefly.

1.1 X-ray Binaries

The history of X-ray astronomy started about four and half decades ago with the discovery of the galactic X-ray source Sco X-1 (Giacconi et al., 1962; Sarty et al., 2007, and references therein), during a rocket flight designed for measuring X-rays from the moon. Because the Earth's atmosphere is optically thick (opaque) to X-rays, X-ray observations cannot be performed from the ground. In the early 1960's rockets and balloons were used to carry X-ray detectors to higher altitudes, above the Earth's atmosphere, to observe X-rays. However, these rocket or balloon flights only lasted a few minutes and this could not allow detailed studies of X-ray sources. This problem was overcome when astronomy satellites were introduced, the first of which was the UHURU satellite. With satellite based instruments it became possible to measure the full range of the X-ray spectrum and carry out observations on time scales of months to years.

In general, X-ray binaries are interacting (mass transferring) binaries where one of the stars (companion star) transfers material onto a compact object. In most cases the compact object is a neutron star or a black hole. The main X-ray source in these objects is the gravitational potential energy released by matter accreted onto the compact object. This results in 2 - 20 keV X-ray luminosities, $L_{\rm x} \sim 10^{36} - 10^{38}$ erg s^{-1} (Verbunt, 1993). A detailed review of the general properties of X-ray binaries can be found in Joss & Rappaport (1984); Lewin, van Paradijs & van den Heuvel (1995); White, Nagase & Parmar (1995) and Charles & Coe (2003).

1.1.1 Evolution of X-ray Binaries

Stars are born from gravitationally collapsing molecular and interstellar dust clouds. The collapse is induced through instability in the cloud which could be due to shock waves from nearby supernovae. A star develops when the core of the contracting protostar reaches temperatures high enough to ignite nuclear fusion reactions. The birth of stars in molecular clouds are driven by gravitational instabilities. The limiting density, i.e. the so called Jeans density, scales as (e.g. Kippenhahn & Weigert, 1990)

$$\rho_{\rm J} \propto \frac{T_{\rm cloud}^3}{M_{\rm cloud}^2}, \tag{1.1}$$

where $T_{\rm cloud}$ and $M_{\rm cloud}$ are the temperature and mass of the cloud respectively. Local density inhomogeneities satisfying $\rho > \rho_{\rm J}$ can condense into stars. This occurs in cold molecular clouds, i.e. $T_{\rm cloud} \rightarrow 0$, with high mass. Stars therefore form in clusters, being bound gravitationally in binaries, triples, etc (Hellier, 2001, p.45). See van den Heuvel (1977) and Joss & Rappaport (1979) for a detailed discussion of the different evolutionary scenarios.

X-ray binaries evolve from binary systems, with one star more massive than the other, in orbit around each other. The more massive star evolves faster and expands to become a giant. As a result of the gravitational interaction it becomes extended and loses some of its material to the companion star. As a result of the mass transfer (or if the mass losing star expands very rapidly), the binary separation decreases rapidly and the mass losing star engulfs its companion star (Paczyński, 1976; Verbunt, 1993). Due to friction between the motion of the companion star and the envelope, angular momentum is removed from the orbital motion and energy is released. This results in the orbit shrinking and the envelope being heated (Verbunt, 1993). This continues until enough energy has been added to the envelope and the more massive star

explodes as a supernova (Verbunt, 1993). After the supernova explosion a compact remnant, a neutron star or a black hole is orbiting the companion star. After some time, the companion star starts to expand (evolve) until the binary separation is close enough that the companion star starts to lose some of its material to the compact object, which may result in the formation of an accretion disc around the compact object.

X-ray binaries are generally divided into two main classes, the Low Mass X-ray Binaries (LMXBs) and the High Mass X-ray Binaries (HMXBs), depending on the mass and nature of the companion (optical) star. They can further be divided into persistent and transient sources depending on their temporal behaviour (or variability). The difference in X-ray behaviour between the LMXBs and HMXBs mainly results from the different mechanisms of mass transfer and accretion and the age of the system.

1.1.2 Low Mass X-ray Binaries

Low mass X-ray binary systems in general consist of a low mass companion star, mainly of spectral type G - M, which transfers material through Roche-lobe overflow onto a compact object (Figure 1.1). These systems on average have relatively short orbital periods (of the order of a day) and their optical counterparts are intrinsically faint objects. Based on the short orbital periods and the absence of luminous companion stars (Padsiadlowski, Rappaport & Pfahl, 2002), it has been inferred that the mass of companion stars in LMXBs, in most cases, are less than a solar mass (i.e. $M \leq M_{\odot}$). The short orbital periods of LMXBs are mostly determined by radial velocity measurements rather than the X-ray eclipses (White, Nagase & Parmer, 1995). These systems generally have nearly circular orbits and the compact objects, in the case of neutron stars, have magnetic fields generally of the order of $B_{*} \gtrsim 10^{8}$ Gauss (Barcons, 2003).

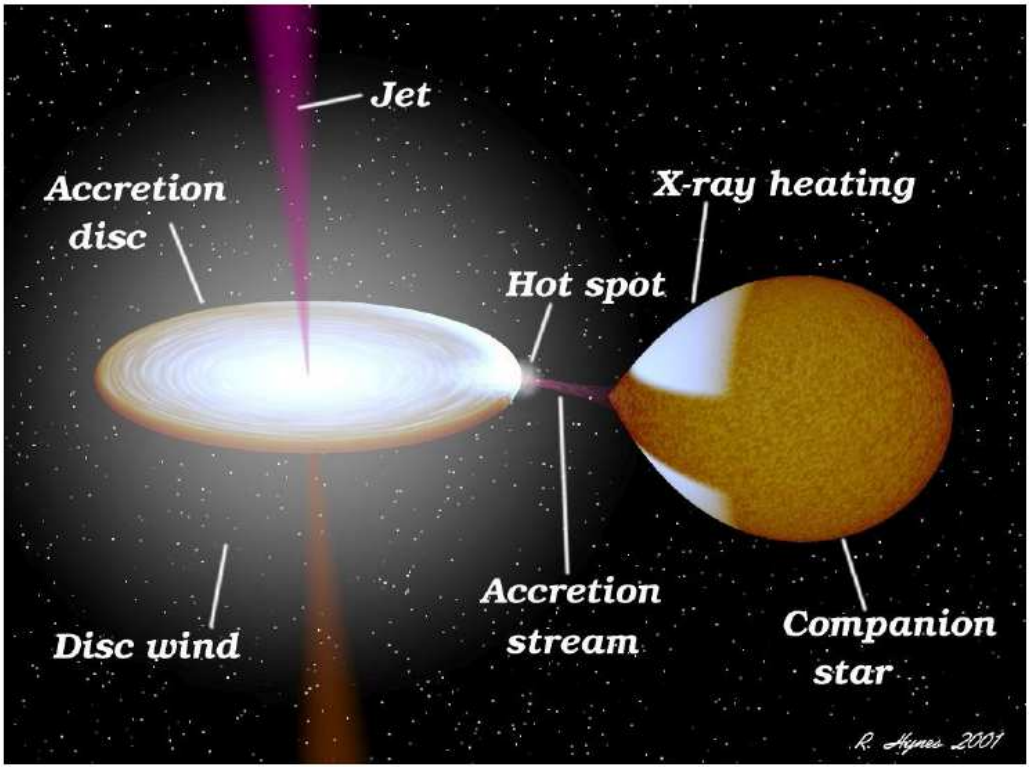

Figure 1.1: Schematic picture of a standard Low Mass X-ray Binary. (*Adopted from R. Hynes, 2001*).

The spectra of the LMXBs are soft (kT ≤ 5 keV) (Verbunt, 1993) and show a few characteristic emission lines superposed on a rather flat continuum. Since the discovery of X-ray binaries there are now about 187 known LMXBs in the Galaxy and the Magellanic clouds (Liu, van Paradijs & van den Heuvel, 2007a). The intrinsic optical luminosity of these systems is usually orders of magnitude less than the X-ray luminosity, i.e. the X-ray to optical luminosity ratio $(L_{\rm x}/L_{\rm opt}) \geq 10$. Many LMXBs also display bursts of X-rays which are interpreted as thermonuclear explosions on the neutron star surface (Lewin, van Paradijs & Taam, 1993).

1.1.3 High Mass X-ray Binaries

High mass X-ray binary systems consist of a compact object (neutron star or black hole) in orbit around a massive ($\geq 10M_{\odot}$) O - B supergiant star. They are relatively young with ages estimated in the range $10^7 - 10^8$ years (Casares, 2005). Currently, 114 Galactic HMXBs have been identified (Liu, van Paradijs & van den Hauvel, 2007b), concentrated towards the spiral arms and are considered as good tracers of star formation rates (Grimm, Gilanov & Sunyaev, 2002), and 128 discovered in the Magellanic clouds (Liu, van Paradijs & van den Heuvel, 2005). The neutron stars in HMXBs are identified by the presence of regular X-ray pulsations which are produced because of misalignment of the magnetic and rotation axes of the neutron star. In this case the X-ray pulsations are observed if the beamed emission from the magnetic pole rotates through the line of sight of the observer (White, Nagase & Parmer, 1995, and references therein). The X-ray pulsations originate from beamed radiation produced close to the magnetic poles of the accreting neutron star.

HMXBs are divided into two broad classes: Those in which the companion star is a supergiant (SG/X-ray binary) and the ones with a Be star (Be/X-ray binary) as the companion star. The two classes differ in the accretion modes with the Be/X-ray binaries accreting directly from circumstellar disc, while the SG/X-ray binaries accrete from a radially outflowing stellar wind. Reig & Roche (1999) suggested a third class of HMXBs characterised by long pulse periods (1000 s), persistent low luminosities (10^{34} erg s^{-1}) and low variability.

SG/X-ray binaries generally have short binary periods, typically 3 - 40 days (Charles & Coe, 2003) and are also called “standard” HMXBs. The X-ray luminosity of these systems is powered by the strong stellar wind of the companion star or Roche-lobe overflow, i.e. the companion

stars in SG/X-ray binary systems generally fill or nearly fill their Roche-lobes. Their luminosities are in the range $10^{34} - 10^{36}$ erg s^{-1} (Charles & Coe, 2003; Liu, van Paradijs & van den Heuvel, 2007b).

Be/X-ray binaries (also known as the hard X-ray transients) represent the largest class of HMXBs. The compact object is a neutron star (X-ray pulsar) (Zhang, Li & Wang, 2004) in a wide (17 - 263 days) (Ziolkowski, 2002) and eccentric orbit around a Be star. A Be star can be defined as an early-type star which at times shows emission in the Balmer lines (Ziolkowski, 2002); and these Balmer lines are thought to originate from circumstellar material around the Be star. In these systems there are two temporal quasi-Keplerian discs: a decretion disc around the companion (Be) star and an accretion disc around the neutron star. X-ray outbursts occur when the neutron star passes through the decretion disc around the Be star. Be/X-ray binary systems are characterised by hard X-ray spectrum.

The different behaviour and/or properties shown by X-ray binary systems largely result from the difference in the modes of mass transfer and accretion onto the compact object. In recent years significant progress has been made in our understanding of mass transfer and accretion in general, as well as the interaction between accretion disc and compact objects in X-ray binary systems. X-ray sources are accretion driven (Prendergast & Burbridge, 1968; Pringle & Rees, 1972) and the observable spectra, luminosity and temporal behaviour of X-ray binaries are dependent on the type of compact object, its magnetic field strength and the accretion mechanism in these systems. It is therefore important to discuss some basic properties and mechanisms of mass transfer, accretion disc production and disc accretion in close binary systems in general. This is briefly reviewed in the following section.

1.2 Mass Transfer and Accretion in Close Binaries

Close binary systems interact through mass transfer from the companion star onto the compact object. Mass transfer and accretion can either occur via Roche-lobe (Figure 1.2) overflow or from a strong stellar wind. Both of these are dependent on, among others, the mass of the companion star and the orbital separation of the two stars in the binary system. Since this thesis focuses on the X-ray binary Her X-1, which is believed to transfer mass primarily through Roche-lobe overflow, only mass transfer via Roche-lobe overflow will be discussed. However, there is also an indication that the companion star in Her X-1 has a wind which probably has an effect on the accretion rate (Boroson et al., 2007, and references therein).

There are two ways in which the companion star can fill its Roche-lobe (King, 1988; Frank, King & Raine, 1992, p.46 and Verbunt, 1993):

(i) The star expanding. This occurs in most close binary systems during the evolutionary process of the system, enabling the companion star to overflow its Roche-lobe.

(ii) The Roche-lobe shrinking. Loss of angular momentum from the binary system can result in a decrease of the Roche-lobe radius of the companion star resulting in the star overflowing its Roche-lobe. This process can be driven by gravitational radiation and magnetic braking (Mestel & Spruit, 1987; Campbell, 1997, pp. 258 - 259; and Hellier, 2001, p.47) or by strong stellar winds (Iben, 1991).

When the companion star fills its Roche-lobe, stellar material will be in contact with the L1 point (Figure 1.2). As a result of the thermal motions and pressure of the gas particles at the apex (L1 point) of the Roche-lobe of the companion star, material flows through the L1 point into the gravitational potential (Roche-lobe) of the compact object. Material leaves the L1 point

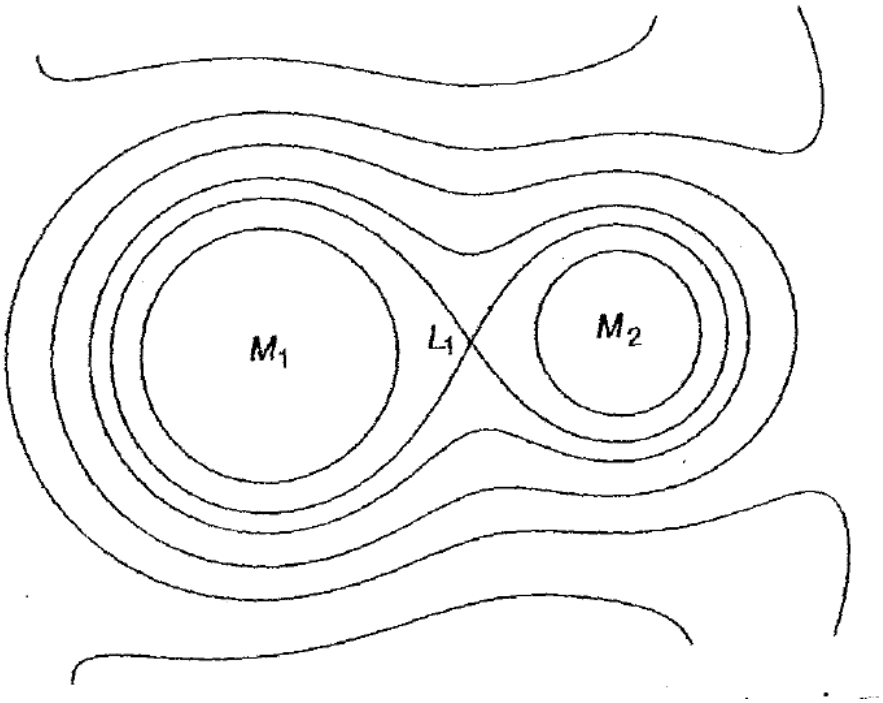

Figure 1.2: Contours of equal gravitational potential surfaces drawn around a binary system. The "eight-like" closed equipotential surface is called the critical surface (Roche surface) and the region within the critical surface is called the Roche-lobe. The common apex of the Roche-lobe is called the inner Lagrangian point (L1 point). (*Adopted from Hellier, 2001, p.25*).

at the speed of sound $c_{\rm s} \sim 10$ km s^{-1}. When material is already in the Roche-lobe of the compact object, the dynamics of the gas stream will be controlled by the strong gravitational field of the compact object. In this phase the stream attains a high velocity ($>> c_{\rm s}$) and the flow is essentially ballistic.

This inflowing gas stream initially has the orbital angular momentum of the L1 point. Conservation of angular momentum in conjunction with Coriolis effect (Frank, King & Raine, 1992, p.54) prevents it from falling directly onto the surface of the compact object. The gas stream

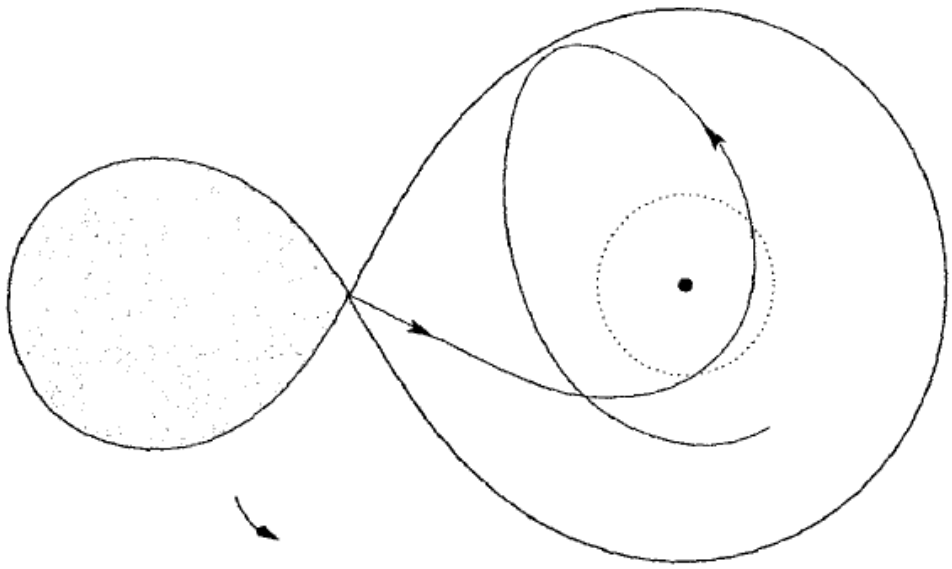

Figure 1.3: Plane view of the trajectory of the gas stream from the companion star. The dotted circle is the circularisation radius. (*Adopted from Hellier, 2001, p.25*).

rather follows a ballistic trajectory around the compact object until it intercepts itself resulting in dissipation of energy via shock formation (Lynden-Bell & Pringle, 1974; Lubow & Shu, 1975 and Spruit, 2002). The flow becomes Keplerian after the collision. On the other hand, the stream has little opportunity to rid itself of the angular momentum it had on leaving the L1 point and will tend to settle in a circular radius of the lowest energy for a given angular momentum load (King, 1988) (see Figure 1.3). The stream will therefore settle in a circular orbit (the so-called circularisation radius) at a radius conserving its initial angular momentum at the L1 point. The physical size of the orbit at the circularisation radius is determined by the intrinsic specific angular momentum of the material leaving the L1 point.

1.2.1 Accretion Disc Formation

The formation of accretion discs around compact objects is a natural result of angular momentum transfer between the mass donating (companion) star and the mass accreting (compact) star. A determining factor for the development of an accretion disc is the magnetosphere of the accreting compact object intercepting the flow after it settled in a ring around the compact object. An accretion disc is an efficient mechanism in which angular momentum is stored and processed in interacting (mass transferring) binary systems. In these systems the circularisation radius is always smaller than the Roche-lobe radius of the compact star, typically a factor of 2 -3 smaller, except for very small mass ratios, e.g. $M_2/M_1 \leq 0.005$ (Frank, King, & Raine, 1992, p.56), where M_2 is the mass of the donor star and M_1 the mass of the compact star. The captured material therefore orbits the compact star well inside its Roche-lobe (see Figure 1.3). This would be prevented however, if the compact star or its magnetosphere already occupied this space, i.e. if $R_* > R_{\rm circ}$ or $R_{\rm mag} > R_{\rm circ}$ where $R_*, R_{\rm circ}$ and $R_{\rm mag}$ represent the radii of the compact star, circularisation and the compact star magnetosphere respectively.

Within the ring of material at the circularisation radius there are dissipative processes, e.g. collision between gas elements, shocks, turbulence, viscous dissipation, etc, which convert some of the energy of the ordered bulk orbital motion about the compact star into thermal (heat) energy which is radiated away. The gas can only accommodate this drain of energy by moving deeper into the gravitational potential of the compact star and in the process some of the material moves into smaller orbits (towards the compact star). The spiralling-in process entails a loss of angular momentum, being transferred outward by viscous torques (Frank, King & Raine 1992, p.57). Thus the ring spreads into a flat disc (Figure 1.4) (fed by the mass transfer stream from the donor star) which continues spreading until the inner edge meets the compact star, or

in the case of a magnetised compact star, the radius where the disc ram pressure balances the magnetospheric pressure (i.e. the magnetospheric radius).

The interaction of the disc with the compact star may lead to a spin-up or spin-down torque that affects the rotation of the compact star (Wang, 1987). At the outer edge, the disc bulges towards the companion star resulting in a tidal interaction between the disc and companion star. This tidal interaction results in the companion star soaking up the disc angular momentum preventing the outward spreading of the disc.

1.2.2 Magnetic Accretion

In some interacting binary systems, the compact object can have a substantial magnetic field that can either intercept the mass flow from the donor star, preventing the formation of an accretion disc (Figure 1.5), or disrupting the disc, if present, preventing it from reaching down to the surface of the accreting star (Figure 1.6). The magnetospheric field also facilitates the mass inflow onto the surface of the compact object, a process called magnetic accretion. This is a direct result of the complex interaction of the ionised (or partially ionised) gas with the magnetic field. Two of the most important fluid-field interactions responsible for the dynamical effects resulting in interesting observational consequences are:

(i) In most astrophysical environments of interest the field is frozen into the plasma (e.g. Jackson, 1975, p.473). The thermal charged particles in the plasma are tied to the field via the Lorentz force ($\mathbf{v} \times \mathbf{B}$), resulting in the bulk flow not being able to cross the field readily. However, it can migrate along the field lines to the surface where it can settle, releasing gravitational potential energy in heat and radiation.

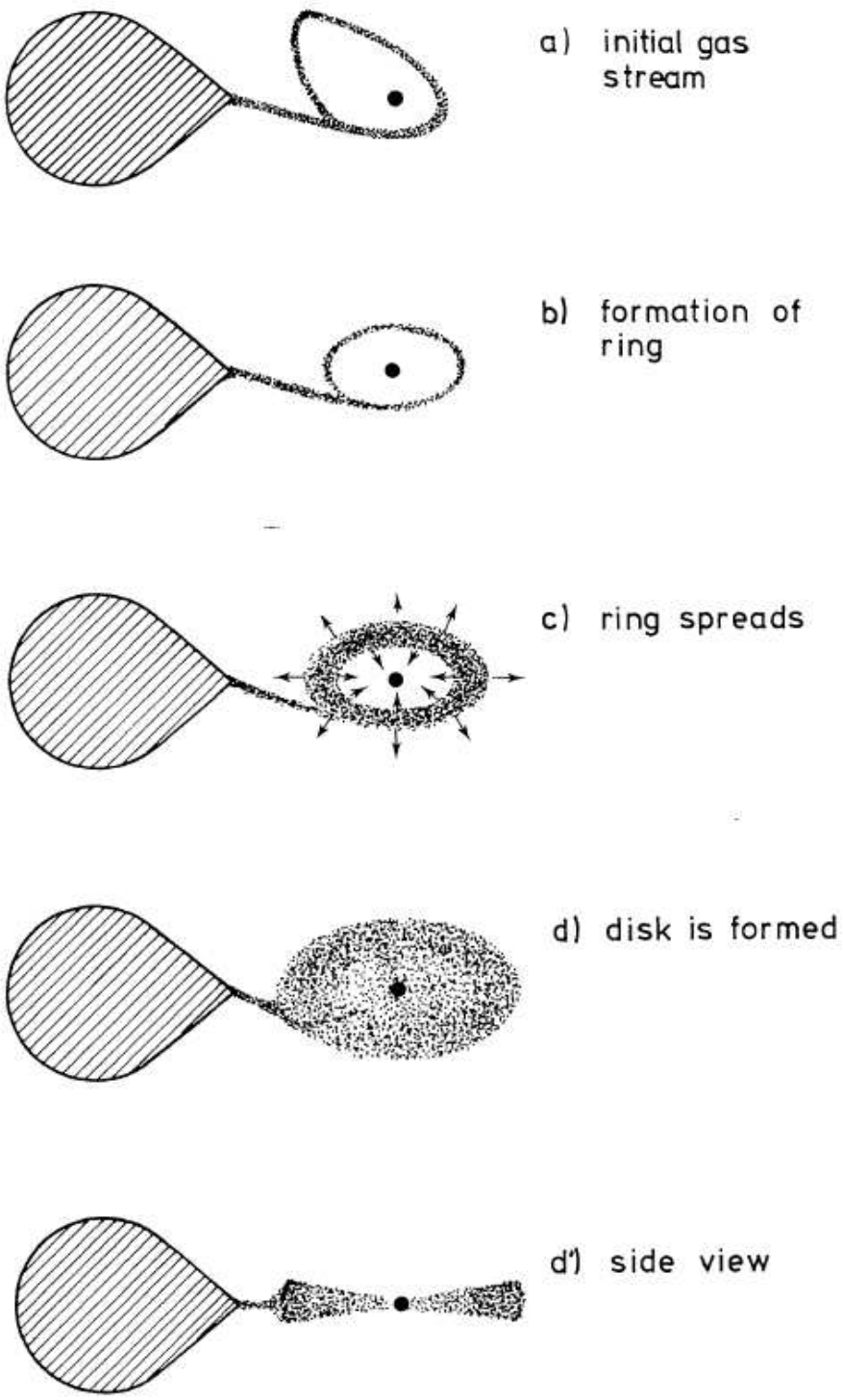

Figure 1.4: Schematic picture showing the formation of accretion disc around a compact object. (*Adopted from Verbunt, 1982*).

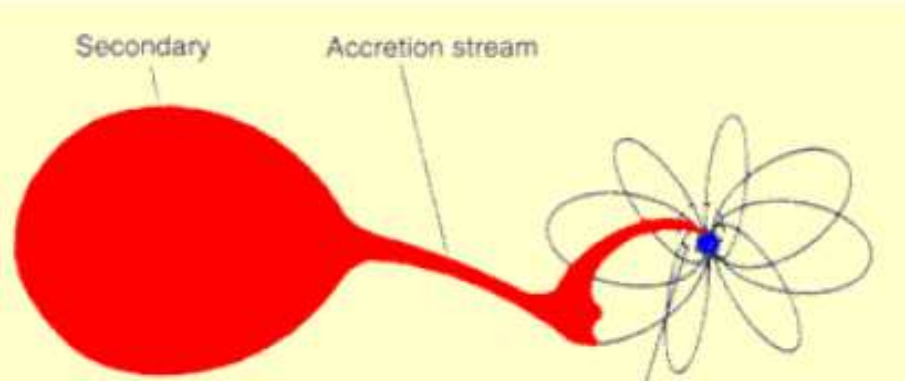

Figure 1.5: Schematic picture showing the interception of the mass transfer stream, by the strong magnetic field of the compact object, at a radius $\geq R_{\rm circ}$ preventing the formation of an accretion disc around a compact object.

(*From:http://heasarc.gsfc.nasa.gov/docs/objects/cvs/cvstext.html*).

(ii) The effective motion of the gas across the field results in a viscous drag and under certain conditions the magnetic field may be advected with the flow (Jackson, 1975, p.478).

These processes have both far-reaching consequences. The motion of the trapped thermal plasma in a magnetic field allows determining the field strength through the cyclotron emission. The frequency with which the electrons orbit the field, i.e. the Larmor frequency (e.g. Frank King & Raine, 1992, p.130) implies that most of the radiation is emitted as a spectral line centred at the fundamental frequency

$$\nu_{\rm cyc} = \frac{eB}{2\pi m_{\rm e} c} = 2.8 \times 10^{18} \left(\frac{B}{10^{12}\ \text{Gauss}} \right) \text{Hz}. \tag{1.2}$$

The second process, i.e. viscous drag, is the process leading to the loss of orbital angular momentum of orbiting satellites as they cross the earth's magnetic field lines. In astrophysical environments this process is almost a neglected process which has a very important effect on flow dynamics of material from the companion star. This may be the origin of the mysterious anomalous disc viscosity which is orders of magnitude higher than the kinematic viscosity.

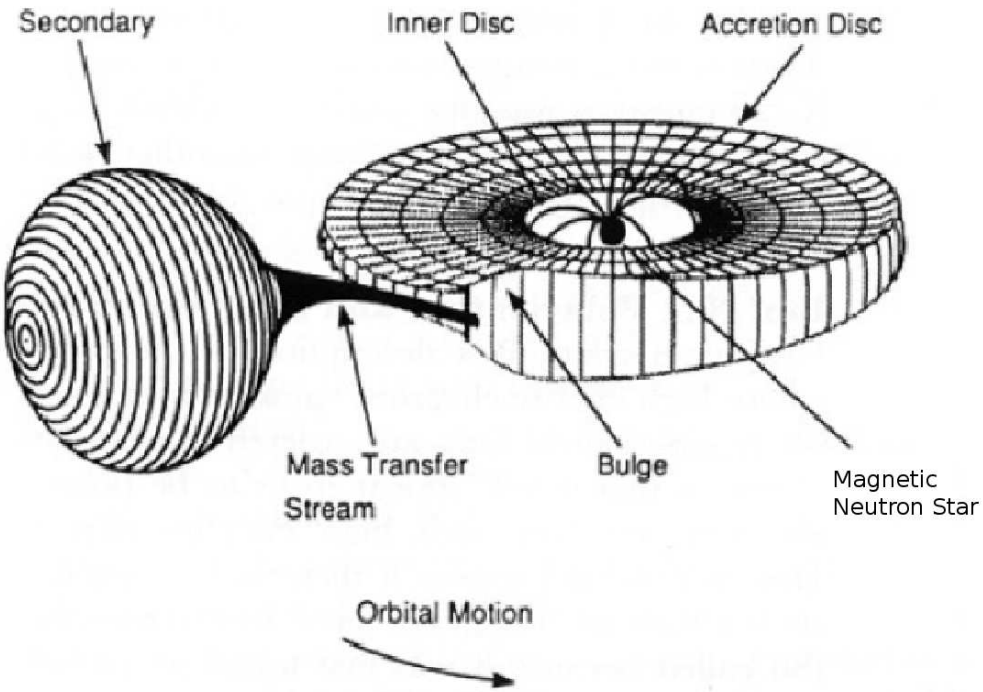

Figure 1.6: Schematic picture showing the disruption of an accretion disc, by the magnetic field of the accreting star, preventing the disc from reaching the surface of the star. (*Adopted from: http://heasarc.gsfc.nasa.gov/docs/objects/cvs/cvstext.html*).

In interacting binary systems where the compact object (e.g. neutron star or white dwarf) has a strong magnetic field, the magnetic field will dominate the inflowing gas close to the compact object. This occurs within the radius where the magnetic pressure balances the ram pressure of the in-falling gas, i.e. the so-called Alfvén or magnetospheric radius. Within the magnetospheric radius, the magnetic pressure exceeds the fluid ram pressure and the material flows along the field lines channelling the flow towards the magnetic poles of the compact object. Close to the magnetic poles of the star, the flow will be concentrated in an accretion funnel until it reaches the surface of the star at the polar caps (Basko & Sunyaev, 1976).

Close to the surface of the compact object, matter (plasma) falling in with supersonic velocities is decelerated by Coulomb interactions at the surface of the star (Basko & Sunyaev, 1976) and heated to high temperatures (Warner, 1995; Gansicke, 1998) resulting in a release of kinetic energy as radiation in the accretion column (Kuijper & Pringle, 1982; Done, Osborne & Beardmore, 1995; Beardmore, Done, Osborne & Ishida, 1995; Gansicke, Beuermann, de Martino, 1995). This process is characterised by:

(i) Strong emission at the optical/IR wavelengths.

(ii) Intense soft and hard X-ray emission.

(iii) An emission line spectrum of excitation which reflects the large streaming motion of the accreted matter in the magnetosphere of the accreting star (e.g. Beuermann, 1988). The energy released in this case can heat the companion star and cause it to expand resulting in an increased mass transfer rate.

1.2.3 Accretion Disc Torque

Ghosh & Lamb (1979a,b) provided a detailed model of the disc torque in a steady axisymmetric accretion disc surrounding a compact magnetic object. Based on the Shakura & Sunyeav (1973) α-disc model, this model provides a detailed treatment of the magnetic coupling between the accreting compact object and the accretion disc. The interaction between the magnetic field and the disc occurs in the boundary layer and the transition zone (see Figure 1.7).

For material to accrete onto the compact object, the angular velocity of the compact object, Ω_*, should be less than the Keplerian angular velocity, $\Omega_{\rm K}(r_{\rm m})$ of the material at the magnetospheric radius, $r_{\rm m}$, i.e $\Omega_* < \Omega_{\rm K}(r_{\rm m})$. This condition can conveniently be expressed in terms of the

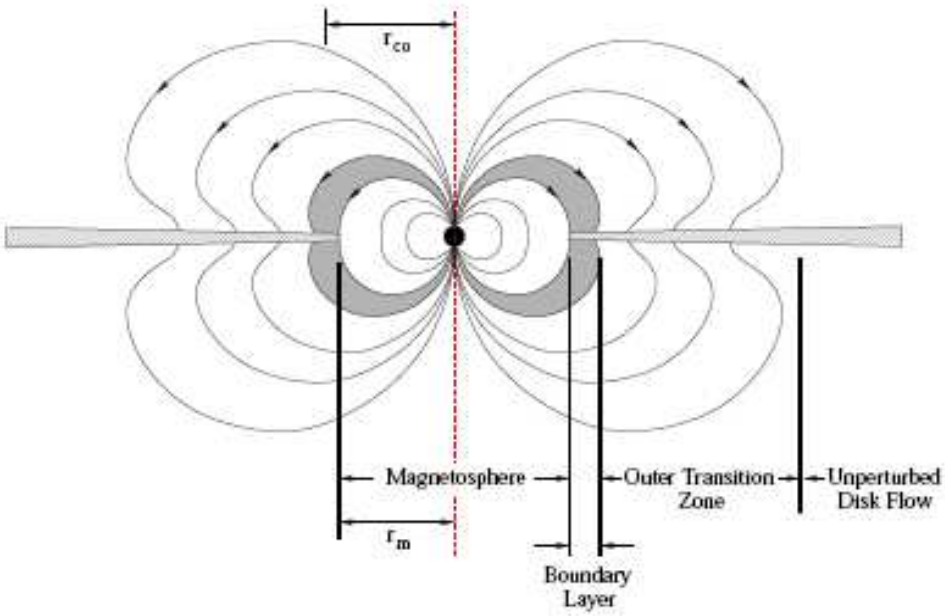

Figure 1.7: Schematic picture of an accretion disc around a magnetic compact object (*Adopted from Ghosh & Lamb, 1979b*). See text by Ghosh and Lamb (1979b) for detailed discussion.

fastness parameter, $\omega_{\rm s}$, as (Elsner & Lamb, 1977; Ghosh & Lamb, 1979b)

$$\omega_{\rm s} = \frac{\Omega_*}{\Omega_{\rm K}(r_{\rm m})} = \frac{r_{\rm m}}{r_{\rm co}} \tag{1.3}$$

where $r_{\rm co}$ is the corotation radius, i.e. the radius where the angular velocity of the magnetosphere is equal to the Keplerian angular velocity of the disc material. If $\omega_{\rm s} < 1$, steady accretion takes place while for $\omega_{\rm s} > 1$ the accreting material will be propelled outward by centrifugal forces.

Based upon the Ghosh and Lamb (1979a, b) model, Wang (1987) derived expressions for the accretion disc torques, i.e. spin-up and spin-down, in accreting magnetic compact objects. This author used a different approach to calculate the toroidal magnetic field induced in the accre-

tion disc. The spin-up torque results from the angular momentum flux of the accreted material and the magnetic stress inside the corotation radius being transmitted to the central accreting compact object. The spin-down torque results from the magnetic stress outside the corotation radius that attempts to force the disc material into corotation with the compact object.

It can be shown (Wang, 1987) that the net torque, N, on the compact object resulting from the spin-up and the spin-down torques is given by

$$N = \dot{M}_*(GM_*r_{\rm co})^{1/2}\left[x_{\rm o}^{1/2} + \frac{2}{9}x_{\rm o}^{31/80}\left(1 - x_{\rm o}^{3/2} - \frac{x_{\rm o}^{9/4}}{(1-x_{\rm o}^{3/2})^{1/2}}\right)\right], \tag{1.4}$$

where $x_{\rm o} = r_{\rm o}/r_{\rm co} < 1$ and $r_{\rm o}$ represents the radial distance where material is guided by field lines onto the compact object. It was further shown that the net torque on the compact object vanishes when $x_{\rm o} = 0.971$. For $x_{\rm o} < 0.971$ the net torque is positive (i.e. $N > 0$) and the compact object spins up; while for $x_{\rm o} > 0.971$, the net torque is negative (i.e. $N < 0$) and the object spins down.

For an accreting compact object having a moment of inertia $I = 2M_*R_*^2/5$, where R_* and M_* represent the radius and mass respectively, the rate of change of the rotation (spin) period is expressed as (Wang, 1987)

$$-\frac{\dot{P}}{P} = \frac{N}{I\Omega_*} \simeq \frac{5}{2}\frac{\dot{M}_*}{M_*}\left(\frac{r_{\rm co}}{R_*}\right)^2 f(x_{\rm o}), \tag{1.5}$$

where $f(x_{\rm o}) = x_{\rm o}^{1/2} + \frac{2}{9}x_{\rm o}\left[1 - x_{\rm o}^{3/2} - \frac{x_{\rm o}^{9/4}}{(1-x_{\rm o}^{3/2})^{1/2}}\right]$, with $\dot{M}_*$ representing the accretion rate.

1.2.4 Accretion Disc Corona

Observational spectral features of active galactic nuclei, X-ray binaries and cataclysmic variables seem to show strong observational evidence that the disc is embedded in a hot corona.

Examples of these spectral features include the fluorescent iron (6.5 - 6.7 keV) emission lines, the power-law spectrum extending to high energies, soft X-ray excess and partial X-ray eclipses (White, Nagase & Parmer, 1995; Liu & Mineshige, 2000; Church & Balucink-Church, 2004 and Belmont & Tagger, 2005).

In recent studies, theoretical models and numerical simulations have been proposed to explain the origin of the disc corona:

(i) External irradiation of the disc by X-rays from the compact object or the central hotter region of the disc itself, evaporating the disc material (Dove, Wilms & Begelman 1997; Miller & Stone, 2000 and Church & Balucinske-Church, 2004) forming the accretion disc corona.

(ii) Numerical simulations of fully magnetohydrodynamical accretion discs (Merloni & Fabian, 2001, and references therein) have shown that the most efficient process for angular momentum transport involves some kind of turbulent magnetic viscosity. Miller & Stone, (2000) have further shown that the dissipation of the magnetic energy built up by the magnetorotational instability (e.g. Balbus & Hawely, 1991, 1998; Balbus, Hawely & Stone, 1996) in the accretion disc can produce a non-uniform active corona which extends a few scaleheights above the flux tubes (Rozanska, Sobolewska & Czerny, 2007, and references therein) which dissipate and magnetise the corona while rising upwards from the disc.

1.3 Outline of Thesis

The discussion presented in this Chapter is intended to provide a basic framework related to the basic properties of X-ray binaries, in particular Her X-1. The rest of the thesis will be structured

as follows: Since the anomalous low state of Her X-1 (the topic of this thesis) is associated with a warped accretion disc, which is possibly the result of a radiation driven process, basic radiation processes in disc accreting pulsars will be presented in Chapter 2. This is also important for understanding and interpreting the lightcurves and energy spectrum presented later in this thesis. In Chapter 3 attention will be given specifically to warped accretion discs. In Chapter 4 a detailed discussion of the 35-day cycle of Her X-1 is presented. The optical and X-ray lightcurves of Her X-1 are discussed in Chapter 5 and the spectral analysis of the anomalous low state of Her X-1 is presented in Chapter 6. Chapter 7 is the conclusion.

Chapter 2

Radiation Mechanisms

2.1 Introduction

To understand and interpret the X-ray spectra that will be discussed in Chapters 6, it is important to understand the mechanisms underlying these radiations. In this section, only processes relevant to the analysis presented in this thesis will be discussed briefly. The discussion related to these radiation mechanisms are based on the texts by Rybicki & Lightman (1979, pp.15 - 27, 167 - 222) and Longair (1992, pp.89 - 118, 1994, pp.229 - 262). Detailed discussion of the radiation processes can be obtained in these texts. Brief discussions of a typical X-ray binary energy spectrum and time variability are included in this chapter in Sections 2.6 and 2.7 respectively.

2.2 Thermal Blackbody Radiation

Radiation emitted by a body as a result of its temperature is called thermal radiation. All objects with temperatures above absolute zero, i.e. 0 K or -273°C, emit thermal radiation. In an idealised case of a body which is in thermodynamic equilibrium with its surrounding, the radiation occupies a significant part of the electromagnetic spectrum. A blackbody can be

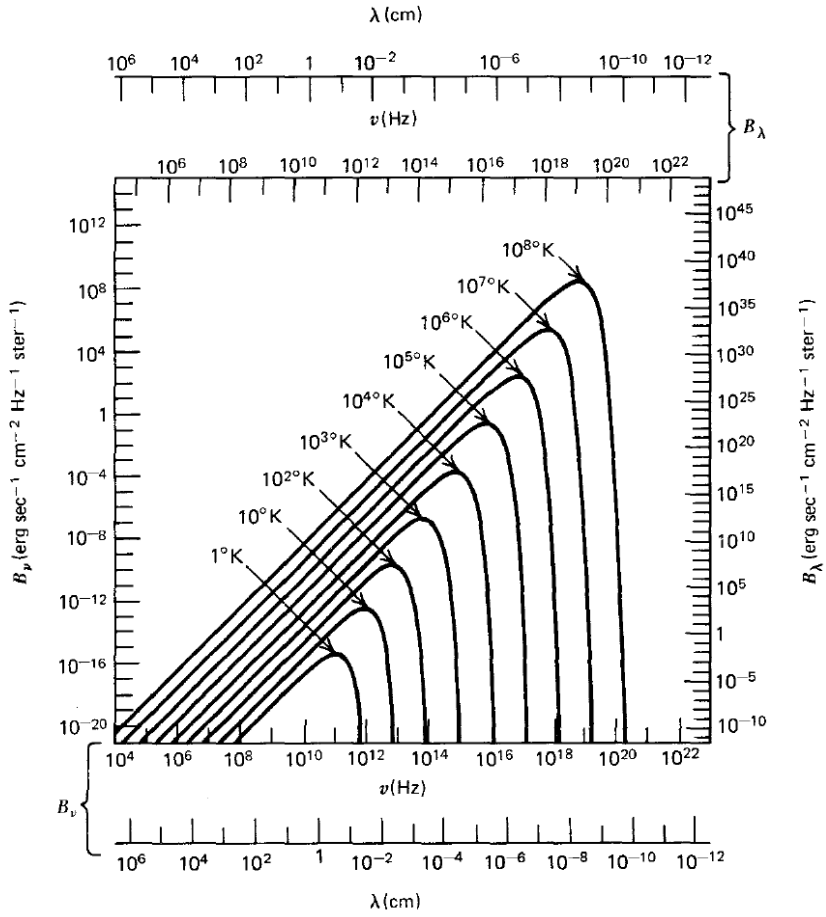

Figure 2.1: Blackbody spectrum at different temperatures. (*Adopted from Rybicki & Lightman, 1979, p.22*).

defined as a hypothetical body that absorbs and emits electromagnetic radiation.

The observed spectrum of a blackbody can be given as a function of temperature, T, and frequency (or wavelength) by Planck's law as

$$B_\nu(T) = \left(\frac{2h}{c^2}\right) \frac{\nu^3}{\left[exp\left(\frac{h\nu}{kT}\right) - 1\right]}, \tag{2.1}$$

where $k = 1.38 \times 10^{-15}$ erg K^{-1} is the Boltzmann constant and $h = 6.625 \times 10^{-27}$ erg s is the Planck constant. The Planck spectrum of a blackbody at various temperatures is shown in Figure 2.1. In the limit of low photon energies (i.e. $h\nu << kT$), Planck's law is approximated

by the Rayleigh-Jeans law, which is expressed as

$$B_\nu(T) \simeq \left(\frac{2\nu^2}{c^2}\right) kT. \tag{2.2}$$

From the Rayleigh-Jeans law (Equation 2.2) it is noted that for a given temperature the blackbody intensity increases as ν^2 rather than falling to zero at higher frequencies. This is a result of classical treatment of photons, ignoring the quantum nature of photons.

In the case where the photon energy is very large (i.e. $h\nu >> kT$) Planck's law can be expressed in the form

$$B_\nu(T) \simeq \frac{2h\nu^3}{c^2} exp\left(-\frac{h\nu}{kT}\right), \tag{2.3}$$

which is called Wien's law. From Wien's law it can be noted that $B_\nu(T)$ decreases exponentially with increasing frequency. The wavelength, $\lambda_{\max}$, where the blackbody has its maximum brightness can be expressed as a function of temperature as

$$\lambda_{\max} = \frac{0.29}{T} \text{ cm K}, \tag{2.4}$$

which is called Wien's displacement law. In astrophysical environments the radiation (soft X-rays) emitted from accretion discs in X-ray binaries can be accounted for by the Planck spectrum.

2.3 Cyclotron Radiation

When a charged particle, e.g. an electron, is bound to a magnetic field and has velocity components parallel and perpendicular to the magnetic field, it is forced to move in a circular path along the magnetic field, i.e. spirals around the magnetic field. In this case the force acting on the charged particle is the Lorentz force and it acts perpendicular to both the magnetic field and

the direction of the particle velocity. The effect of this force causes the particle to spiral in a helix-like path around the field line. The Lorentz force accelerates the charged particle, and this in turn, generates radiation.

For a particle moving with a relativistic velocity (with speed close to the speed of light), e.g. in pulsar magnetosphere, the radiation emitted is called synchrotron radiation; while for the case where a particle moves with non-relativistic speed the radiation emitted is called cyclotron radiation. From classical electrodynamics, an accelerated charged particle in a magnetic field emits a narrow line at a frequency given by (e.g. Frank, King & Raine, 1992, p.130)

$$\nu_{\rm cyc} = \frac{eB}{2\pi m_{\rm e} c}, \tag{2.5}$$

called the cyclotron frequency. Here $m_{\rm e}$ represents the electron mass and B the magnetic field strength.

In astrophysical environment, cyclotron emission occurs in the polar caps of rotating compact objects, e.g. neutron stars in X-ray binaries, and this allows direct measurement of magnetic field strengths in neutron stars. From observations of Her X-1 in 1975, Trümper et al. (1977) discovered a strong cyclotron emission feature in the X-ray spectrum of Her X-1 at ~ 53 keV (see Figure 2.2). This is consistent with observations of Gnedin & Sunyeav (1974) and Basko & Sunyeav (1975) who predicted that such emission occurs in the hot highly magnetised plasma at the polar caps of accreting neutron stars. Trümper et al. (1977) showed that the corresponding magnetic field strength in the emitting region in the case of Her X-1 is 4.6×10^{12} Gauss. This spectral line, i.e. the cyclotron emission, will not appear in the X-ray spectrum of Her X-1 discussed in Chapter 6 given the energy range discussed in this thesis.

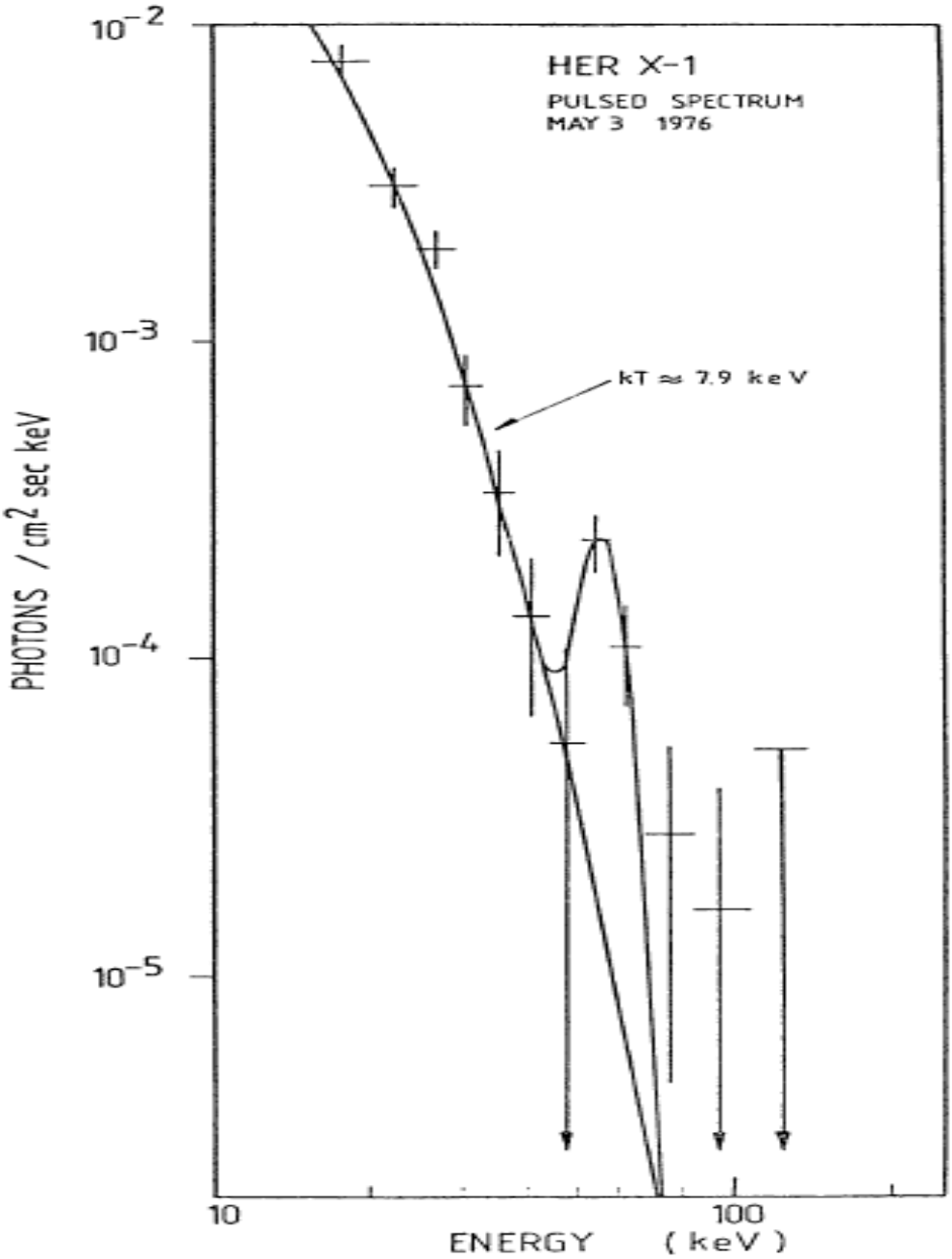

Figure 2.2: X-ray spectrum of Her X-1 showing the cyclotron feature. (*Adopted from Trümper et al., 1977*).

2.4 Compton Scattering

Compton scattering refers to the process of interaction between a photon and an electron. The low frequency limit of Compton scattering is usually referred to as Thomson scattering, i.e. scattering of a photon with low energy ($h\nu << m_{\rm e}c^2$) by a free electron at rest. The differential cross-section for Thomson scattering is given by the equation

$$\frac{d\sigma_{\rm T}}{d\Omega} = \frac{r_{\rm e}^2}{2}(1+\cos^2\theta), \tag{2.6}$$

where $\sigma_{\rm T}$ is the Thomson cross-section, Ω the solid angle and θ the angle between the trajectories of the incident and the scattered photons. The classical electron radius, $r_{\rm e}$, is given by

$$r_{\rm e} = \frac{e^2}{m_{\rm e}c^2}. \tag{2.7}$$

In Thomson scattering the energy of the incident photon is equal to that of the scattered photon. The only change is in direction and momentum and this scattering is called elastic or coherent scattering. It can be shown that the total cross-section for Thomson scattering, obtained from integrating Equation 2.6, is given by

$$\sigma_{\rm T} = \frac{8\pi}{3}r_{\rm e}^2, \tag{2.8}$$

which is dependent only on the classical electron radius and is therefore constant.

In the case where energy of the photon is comparable to or greater than the electron rest mass, $m_{\rm e}c^2$, there is transfer of energy from the photon to the electron, and relativistic and quantum electrodynamic effects, e.g. interaction of spin and magnetic moments of the electron with the photon, have to be taken into account. This process is called Compton scattering. In Compton scattering the incident photon scatters an electron initially at rest and in the process the electron gains energy and the scattered photon has a frequency lower than that of the incident photon

(Figure 2.3).

From the conservation of energy and momentum, it can be shown that the change in wavelength of a photon after Compton scattering is given by

$$\Delta\lambda = \frac{h}{m_{\rm e}c^2}(1-\cos\theta). \tag{2.9}$$

Using the relation between energy and wavelength, i.e. $E = hc/\lambda$, and Equation 2.9, the energy of the scattered photon, E' can be expressed in the form

$$E' = \frac{E}{1-\epsilon(1-\cos\theta)}, \tag{2.10}$$

with $\epsilon = E/m_{\rm e}c^2$. In the scattering event, energy can also be transferred from an electron to the photon, a process called inverse Compton scattering, which is most applicable in high energy astrophysics. This is discussed in section 2.4.1.

Compton scattering increases the photon wavelength and the photon energy decreases accordingly. In astrophysical environments Compton scattering may be considered an important source of opacity in a typical accretion disc where temperatures are high enough to keep the gas in the disc ionised.

2.4.1 Inverse Compton Scattering

When electrons are no longer considered to be at rest (electrons moving at high velocities), e.g. the hot electron plasma in accretion discs and accretion disc coronae, the thermal motion of electrons become important. In this case energy is transferred from the electrons to the photons, i.e. the photons are being up-scattered, carrying away energy (energy is being transferred from the electrons to the photons) (Figure 2.4). This is the reverse process of Compton scattering

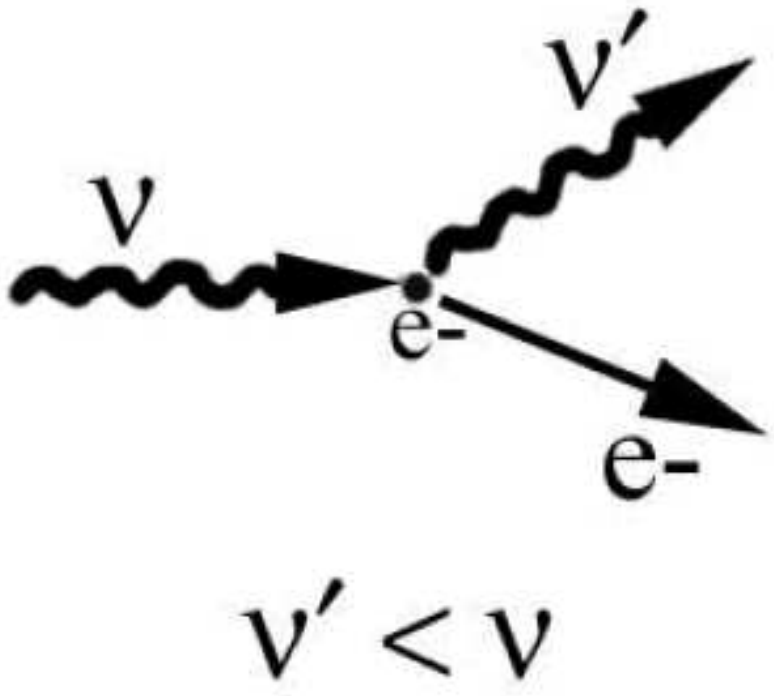

Figure 2.3: Schematic picture showing Compton scattering, where an incident photon is scattered by an electron initially at the rest. In the process the photon loses part of its energy which is gained by the electron. (*From http://venable.asu.edu/quant/proj/compton.html).*

and is called Inverse Compton scattering (or Comptonisation). Inverse Compton scattering is a common occurrence in astrophysical objects where low energy photons are up-scattered by high energy (relativistic) electrons.

In inverse Compton scattering, assuming a thermal velocity distribution of electrons and in the non-relativistic limit ($h\nu << m_{\rm e}c^2$), the energy transfer per scattering is given by

$$\frac{\Delta E}{E} \sim \frac{4kT_{\rm e} - E}{m_{\rm e}c^2}, \tag{2.11}$$

with $T_{\rm e}$ representing the electron temperature. From Equation 2.11, it is noted that transfer of energy to a photon only occurs when $E < 4kT_{\rm e}$, i.e. the condition for a photon to gain energy

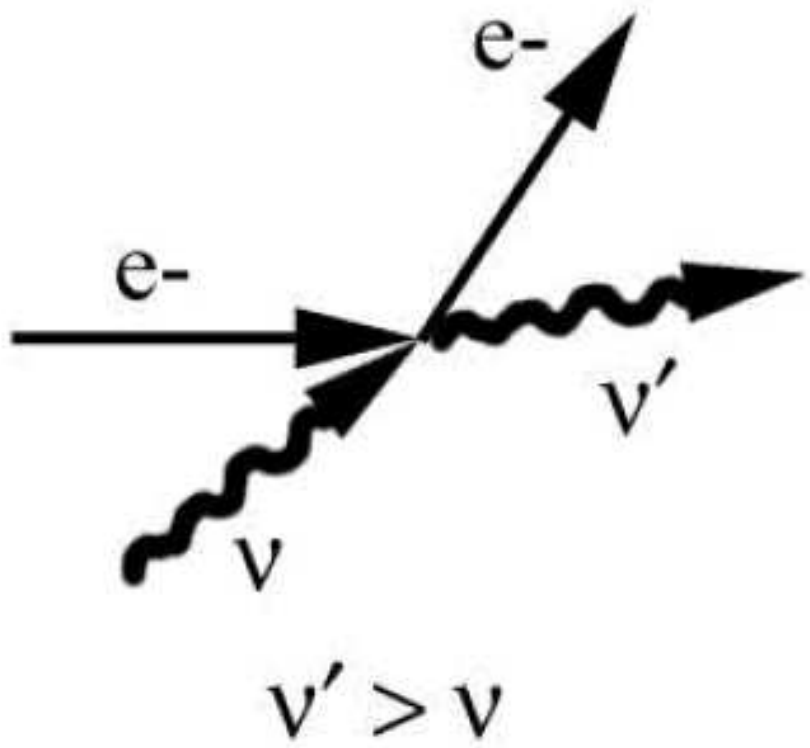

Figure 2.4: Schematic picture showing Inverse Compton scattering where a high energy electron interacts with a photon and in the process the electron loses energy which is gained by the photon. (*From http://venable.asu.edu/quant/proj/compton.html).*

during the scattering.

In inverse Compton scattering, relativistic effects become important when high energy electrons are involved. In this case the total angle-integrated cross-section, known as the Klein-Nishina cross-section, is given by the equation

$$\sigma_{\mathrm{K-N}} = \frac{\pi r_{\mathrm{e}}^2}{\epsilon_{\mathrm{rel}}} \left[\left(1 - \frac{2(\epsilon_{\mathrm{rel}}+1)}{\epsilon_{\mathrm{rel}}^2} \right) \ln(2(\epsilon_{\mathrm{rel}}+1) + \frac{1}{2} + \frac{4}{\epsilon_{\mathrm{rel}}} - \frac{1}{2(2\epsilon_{\mathrm{rel}}+1)^2} \right] \tag{2.12}$$

where $\epsilon_{\mathrm{rel}} = \gamma h\nu / m_{\mathrm{e}}c^2 = \gamma E / m_{\mathrm{e}}c^2$. For low energy photons ($\epsilon_{\mathrm{rel}} << 1$), the Klein-Nishina

cross-section reduces to the Thomson cross-section, i.e.

$$\sigma_{\mathrm{K-N}} \approx \frac{8\pi}{3} r_{\mathrm{e}}^2 (1 - 2\epsilon_{\mathrm{rel}}) = \sigma_{\mathrm{T}}(1 - 2\epsilon_{\mathrm{rel}}) \approx \sigma_{\mathrm{T}}; \tag{2.13}$$

while at high energies ($\epsilon_{\mathrm{rel}} >> 1$) the cross-section becomes smaller than the Thomson cross-section, and is given by

$$\sigma_{\mathrm{K-N}} \approx \frac{\pi r_{\mathrm{e}}^2}{\epsilon_{\mathrm{rel}}} \left[\ln(2\epsilon_{\mathrm{rel}}) + \frac{1}{2} \right]. \tag{2.14}$$

In this case the maximum energy gained by a photon in inverse Compton scattering, in the laboratory (observer's) frame, is given by

$$E_{\max} \approx \gamma^2 h\nu. \tag{2.15}$$

This, i.e. equation 2.15, refers to the Thomson limit. The corresponding energy of the photon scattered by the relativistic electron, in the photon frame, is given by

$$\nu' \approx \gamma m_{\mathrm{e}} c^2. \tag{2.16}$$

In astrophysical environments there are electrons with γ in the range 100 to 1000, resulting in low energy photons scattered to very high energies, e.g. optical photons of frequency $\sim 10^{14}$ Hz ($\varepsilon_\gamma = 1$ eV) can be up-scattered to gamma-rays with frequency $\sim 10^{20}$ Hz, ($\varepsilon_\gamma = 10^6$ eV) which is an increase in frequency (or energy) by a factor of 10^6. It is unlikely that ultra-relativistic electron (with $\gamma >> 1$) exist in Her X-1 since there is no confirmation of earlier reports of very high energy gamma-rays from Her X-1. It is therefore questionable whether this process is applicable to Her X-1.

In high energy astrophysics multiple inverse Compton scattering events are a common occurrence. When a photon passes through a region of high charge particle density, it experiences

multiple scattering. Given a region with electron density $n_{\rm e}$ and size l, the optical depth ($\tau_{\rm e}$) for scattering through the region is given by

$$\tau_{\rm e} = \int n_{\rm e}\sigma_{\rm T}\, dl. \tag{2.17}$$

Equation (2.17) gives a measure of the number of scattering events a photon undergoes when escaping from the region. For an optically thick region ($\tau_{\rm e} >> 1$) a photon follows a random walk path, resulting in the photon being scattered several times. This results in a significant increase in the photon energy. This process is also called comptonisation and the spectrum produced in this manner is said to have been comptonised.

If the mean free path of a photon is $\lambda_{\rm e} = (n_{\rm e}\sigma_{\rm T})^{-1}$, the total number of scatterings a photon experiences while traversing a region of size l is

$$i = \left(\frac{l}{\lambda_{\rm e}}\right)^2. \tag{2.18}$$

If the frequency of the incident photon is ν and that of the scattered photon is ν', with the frequency of the scattered photon boasted by a factor of ϖ for each scattering, the photon frequency after a single scattering event is

$$\nu' = \varpi\nu. \tag{2.19}$$

After i scatterings, the frequency of the scattered photon becomes

$$\nu'_i = \varpi^i\nu. \tag{2.20}$$

If the probability that a photon will escape after a single scattering event in an optically thick medium is given by $p \approx \tau_{\rm e}$, then probability of escape after i independent scattering events is $p_i \approx \tau_{\rm e}^i$. The spectrum of the emergent photon I' can therefore be expressed in the form

$$I' = I\tau_{\rm e}^i. \tag{2.21}$$

Using Equations 2.20 and 2.21 it can be shown that

$$I' = I\left(\frac{\nu_i}{\nu}\right)^{log\tau_e/log\varpi} \tag{2.22}$$

$$= I\left(\frac{\nu_i}{\nu}\right)^{-\alpha} \tag{2.23}$$

where $\alpha = -log\tau_e/log\varpi$. This shows that the comptonised spectrum in this case follows a power law with energy spectral index given by α.

An example of this comptonised spectrum is a photon leaving a hot plasma being up scattered, carrying away energy and in the process cooling the plasma, a process also called Compton reflection. Compton reflection is normally accompanied by an iron emission line (Schultz, 2004). This emission line results from the absorption of photons near the iron absorption edge and part of their energy is re-emitted as fluorescent photons.

2.5 Photoelectric Absorption

Photoelectric absorption is the dominant process by which low energy photons ($h\nu << m_{\rm e}c^2$) lose their energy. It is one of the principal sources of opacity in stellar interiors and atmospheres. In photoelectric absorption, a photon interacts with an atom and in the process it may be completely absorbed. In this process the photon's energy ejects an inner shell electron, called a photoelectron. Part of the photon energy is used to overcome the binding energy of the photoelectron and the rest manifests as kinetic energy. If an incident photon of energy $h\nu$ ejects an electron with binding energy $E_{\rm bind}$ ($E_{\rm bind} < h\nu$) the photoelectron will have kinetic energy $E_{\rm e}$ given by

$$E_{\rm e} = h\nu - E_{\rm bind}. \tag{2.24}$$

Energy levels within an atom for which $h\nu = E_{\rm bind}$ are called absorption edges because the ejection of electrons from these energy levels is unlikely.

The characteristic features of X-ray absorption spectra observed in X-ray sources are understood in terms of photoelectric absorption. Each atom has a characteristic X-ray term that shows the energies of the different stationary states within the atom for the removal of an electron. The X-ray photoelectric absorption cross-section for hydrogen (H), carbon (C), argon (Ar) and oxygen (O) as a function of wavelength is shown in Figure 2.5. Curves like in Figure 2.5 are useful in the construction of proportional counters used in X-ray detectors. This is because the photoelectric absorption spectra of the detector gas and the window materials are useful in determining the efficiency and sensitivity of proportional counters.

Photoelectric absorption is also important in determining the X-ray absorption coefficients for stellar material. This is done by adding together curves of the form presented in Figure 2.5 for the cosmic abundance of the elements. In this case the dominant source of opacity is provided by the K-edges which correspond to the ejection of electrons from the 1s shell of the atom or ion. Figure 2.6 shows the total absorption coefficient for X-rays with the K-edges of the elements contributing to the total absorption indicated. In the studies of low resolution X-ray spectra, it is not possible to resolve the K-edges individually as distinct features. In this case a linear interpolation formula for X-ray absorption coefficient $\sigma_{\rm x}$ and optical depth $\tau_{\rm x}$ is used and is given by

$$\tau_{\rm x} = 2 \times 10^{-26} \left(\frac{h\nu}{1{\rm KeV}} \right)^{-8/3} \sigma_{\rm x}. \tag{2.25}$$

The X-ray absorption coefficient is related to the optical depth by the equation

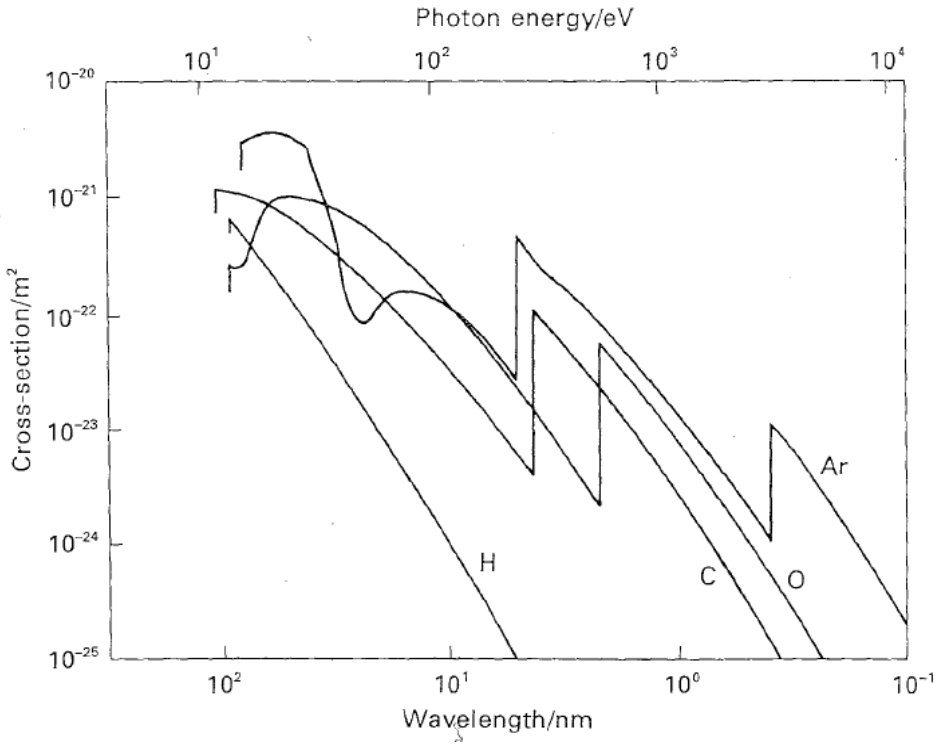

Figure 2.5: Graph showing the absorption coefficients of hydrogen, carbon, oxygen, and argon atoms as a function of wavelength. (*Adopted from Longair, 1992, p.90).*

$$\tau_{\mathrm{x}} = \sigma_{\mathrm{x}} \int N_{\mathrm{H}} dl, \tag{2.26}$$

with N_{H} representing the number density of hydrogen atoms and is expressed in particles per cubic metre. Photoelectric absorption is responsible for the absorption of X-ray by chemical elements (e.g. the oxygen absorption edge seen near 0.55 keV in Figures 6.14 and 6.15 in Chapter 6), and is applicable to the accretion material as well as in the interstellar medium.

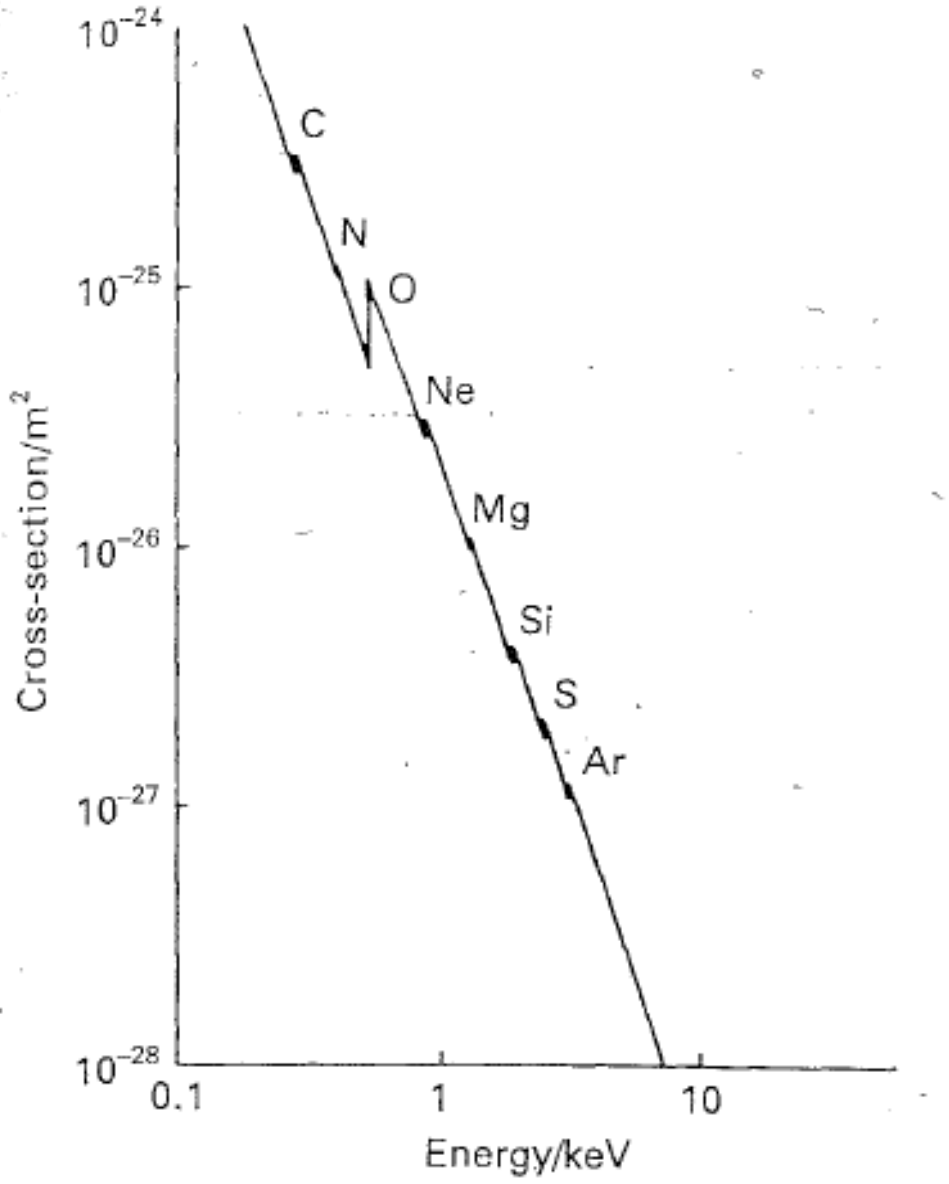

Figure 2.6: Graph showing the absorption cross section for interstellar gas with typical cosmic abundance of chemical elements. (*Adopted from Longair, 1992, p.91).*

2.6 Energy Spectrum of X-ray Binaries

The X-ray spectrum of a typical X-ray binary consists of both thermal and non-thermal emission from the system and is modified by interstellar absorption. Based on the total luminosity and

relative contribution of these two main radiation components, the X-ray spectra of these systems can in general be represented by two main components:

(i) The soft component (high/soft state), where the X-ray emission is dominated by thermal blackbody emission, related to the optically thick and geometrically thin accretion disc (Dal Fiume et al., 1998).

(ii) The hard component (low/hard state), which is associated with the accretion disc corona. This hard component is associated with inverse Compton scattering in the accretion disc corona, i.e. soft photons from the accretion disc are up-scattered in the disc corona by high energy electrons. It is dominated by hard (photon index < 2) power laws with a marked high-energy cut-off at high energies (> 10 keV) (White, Swank & Holt, 1983) (see Figure 2.7).

Interstellar absorption plays a significant role in the overall spectra of X-ray binaries, i.e. significant flux $\lesssim 0.2$ keV is removed by interstellar absorption. Mistuda et al. (1984) showed that the energy spectra of LMXBs harden with increasing intensity and the difference of the spectra before and after an intensity increase shows invariably a blackbody spectrum of kT $\backsimeq$ 2 keV. These authors showed that the observed spectra of LMXBs can be expressed as a sum of two fixed spectral components: a hard component with a blackbody spectrum of kT $\backsimeq$ 2 keV and a soft component with a "multicolour" spectrum expected from the optically thick accretion disc. The hard component was interpreted as emission from the neutron star surface while the soft component as emission from the optically thick accretion disc (Church, 2004 and references therein). This is the so called "Eastern model".

In another model, i.e. the so called western model (White, Stellar & Parmar 1988), the dominance of comptonisation in LMXB spectra was described in terms of the generalised thermal

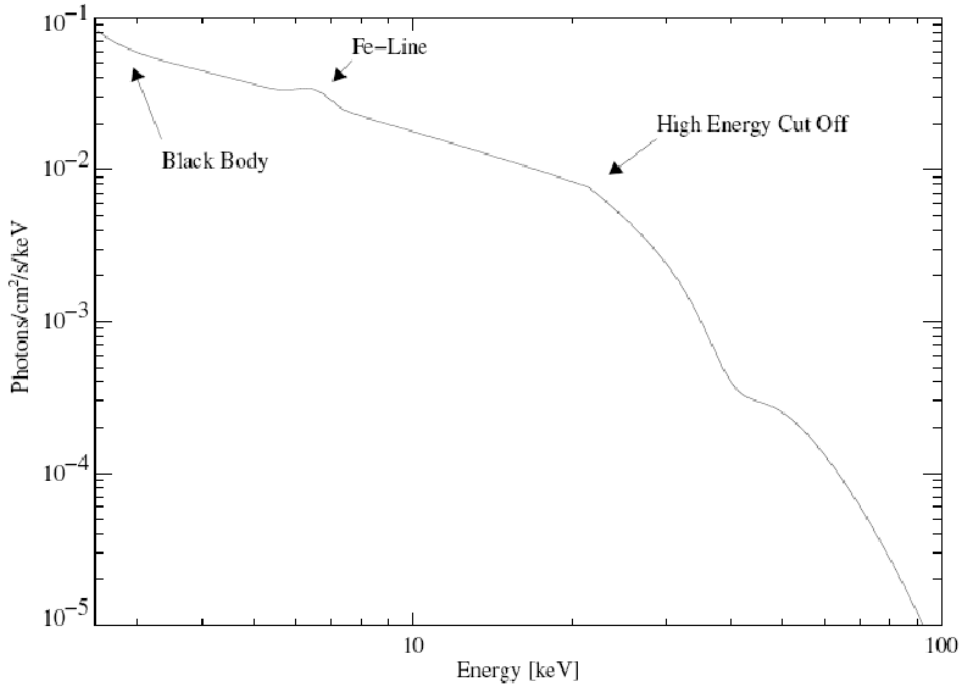

Figure 2.7: Typical X-ray spectrum of X-ray binary. (*Adopted from Kuster, 2004).*

model consisting of a power law with high energy exponential cut-off corresponding to the energy limit of comptonising electrons. Church & Baluciństa-Church (1995) proposed another model, i.e. the Birmingham model, closely related to the western model. In the Birmingham model two continuum components exist in all LMXBs: a simple blackbody emission from the neutron star and comptonised emission from the extended accretion disc corona.

Church (2004) observed that the key to resolving the controversy of the correct emission model has lain with the dipping LMXBs and this provides more diagnostics (Church, 2001) for the emission region. During X-ray dips flux is removed across all energies as the disc rim blocks the inner region from the observer. Church et al. (1997) showed from comparison of dip ingress lightcurves with X-ray spectra that the blackbody component is rapidly blocked, while

more gradual removal of comptonised component suggests that it must originate in a region $\gtrsim 5 \times 10^4$ km in extent. The Birmingham model seems to provide evidence for the presence of blackbody component and it has been shown (e.g. Church et al., 1997, 1998 and Balucińska-Church et al., 2001) that the model provides very good fit to a number of LMBXs.

Emission lines, in addition to the continuum flux, also contribute to the overall spectrum of X-ray binaries. The most interesting emission line is the fluorescent iron K_α line observed between ~ 6.4 keV and ~ 6.7 keV (e.g. White, Swank & Holt, 1983). In some X-ray binaries, e.g. Her X-1, there is evidence for double line structure at ~ 6.4 keV and ~ 6.7 keV (Pravdo et al. 1979; Endo, Nagase & Muhara, 2000; and Still et al., 2001b). Ohashi et al. (1984), Hirano et al. (1987) and Endo, Swank & Holt (2000) interpreted the ~ 6.4 keV line as fluorescent emission from cooler matter, e.g. the irradiated face of the donor star (Still et al., 2001b) and the ~ 6.7 keV as emission from the hot accretion disc corona.

X-ray spectra in the lower energy range are normally subjected to photoelectric absorption, attributed to the interstellar or circumstellar matter (Nagase, 1989). These absorption features change with time depending on the orbital phase and in some cases sporadically (Sato et al., 1986). Sato et al. (1986) and Leahy & Matsuoka (1989) detected an absorption edge of iron at ~ 7.3 keV in some X-ray binaries with strong low energy absorption. This absorption edge and the soft X-ray absorption are attributed to the flow and distribution of accreting matter in the binary system (Nagase, 1989).

The power law hard X-ray component in the X-ray spectrum of AGNs and X-ray binaries is produced by the Compton up-scattering of soft disc photons by the optically thin disc corona (Zdziarski, 1999). Liu & Mineshige (2002) noted that the relative strength of the hard X-ray

component with respect to the UV - soft X-ray component is ascribed to the dominance of the thermal emission or comptonisation from the accretion disc corona. Only half of the radiation emitted from the disc corona is emitted as hard X-rays and the other half illuminates the disc and is reprocessed and radiated as soft disc radiation.

The optical spectra of X-ray binaries are dominated by emission from the accretion disc and the irradiated face of the companion star. This emission is a result of the reprocessing of the incident X-rays to optical wavelengths. In addition to the continuum flux, emission lines also contribute to the overall spectrum (van Paradijs & McClintock, 1995; Nelemans et al., 2003 and Hutchings et al., 2005). The origin of the emission lines is probably the irradiated accretion disc or the irradiated donor star.

2.7 Time Variability in X-ray Binaries

X-ray binaries show variability in intensity and spectral shape on timescales ranging from milliseconds to months and years. Some of these variations are periodic, e.g. spin (pulse) and orbital periods, while others are not necessarily periodic, e.g. super-orbital periods observed in some X-ray binaries.

Pulse periods range from less than 0.1 s to nearly 1500 s (Joss & Rappaport, 1984; White, Nagase & Parmer, 1995). These authors also observed that the driving mechanism of X-ray pulsations is the material accreted onto the magnetic polar caps of the rotating compact star. This is different from the energy source of radio pulsars, which draw their energy from the rotational kinetic energy of the compact star. Observations have shown that over long periods of time, the pulse period changes, i.e. it either increases or decreases linearly with time and in

some cases no long term trend is seen but only a random walk in the period (Joss & Rappaport, 1984 and references therein). The change in pulse period over a long period of time can be understood in terms of torque exerted on the compact object resulting from the interaction of the magnetic field of the compact object and the accretion disc as already discussed in Section 1.2.3.

Orbital periods in X-ray binaries range in the order of hours to days (Joss & Rappaport, 1984 and Charles & Coe, 2003). This is seen in both X-ray and optical wavelengths. The X-ray modulation is seen when the binary system is viewed close to the orbital plane and in this case eclipses by the companion star and obscuration by material in the accretion flow can take place. In the optical the modulation can be caused by the rotation of the irradiated face of the companion star. In some X-ray binary systems, e.g. Her X-1, pre-eclipse (X-ray absorption) dips are observed in the X-ray wavelengths (Crosa & Boynton, 1980; White & Swank, 1982). These dips are probably the result of absorption from cold matter in the line of sight of the observer (İnam & Baykal, 2005, and references therein).

Super-orbital periods have been observed in a number of X-ray binaries. These variations are on timescales of tens to hundreds of days. These variations are associated with precession of a warped/tilted disc around the central accreting compact object (see Chapter 3 for a discussion related to warped precessing discs). In some binary systems, e.g. Her X-1 and LMC X-4, the

variation is stable and periodic while in some, e.g. X1916-053 (Paul et al., 2000; Homer et al., 2001) the variation is “quasi-periodic” and this may be attributed to variations in mass transfer rates (Priedhorsky & Terrell, 1984). The focus now shifts to mechanisms resulting in warped accretion discs.

Chapter 3

Warped Precessing Accretion Discs

3.1 Introduction

As mentioned in the previous chapter, warped and precessing accretion discs are a common occurrence in many astronomical objects or systems, e.g. AGNs, YSOs and X-ray binaries. Warped and precessing discs, observed close to edge-on, have been used to explain the long term periodicities (super-orbital periods) in X-ray binaries (Katz, 1973). Although there still exists uncertainty about the exact mechanism responsible for causing the warp and precession of discs, many theoretical models have been proposed to explain the mechanisms responsible for the warping and precession of accretion discs in astrophysical environments. Katz (1973) proposed that the precession is forced by the tidal torque from the companion star which results from a misalignment between the inclination of the compact object and the outer parts of the accretion disc, e.g. in the X-ray binary GRO J 1665-40 (Martin, Pringle & Tout, 2007 and references therein). More studies have suggested other mechanisms responsible for producing warped precessing accretion discs in astrophysical objects; e.g. radiation-driven warping (Pringle, 1996, 1997; Maloney & Begelman, 1997; Wijer & Pringle, 1998, 1999); wind pressure (Schandl & Meyer, 1994; Schandl, 1996); magnetically driven warping (Lai, 1999; Murray et al., 2002; Terquem & Papaloizou, 2000) etc. To illustrate the complexity of the phenomenon, a brief

discussion of the relevant models driving disc instabilities is presented in the following section.

3.2 Accretion Disc Instabilities

In this section, accretion disc instabilities that lead to warping of accretion discs will be discussed briefly. The main focus will be on the radiation-driven instability which has been proposed (Pringle, 1996, 1997) as the main mechanism behind the disc warp in the X-ray binary Her X-1.

3.2.1 Radiation-driven Instability

Radiation instability (or radiation pressure) has been suggested as one of the mechanisms driving disc warp (e.g. Petterson, 1977). This study showed that an initially warped/tilted optically thick disc that is illuminated by the X-ray flux from the central accreting compact object will re-radiate the intercepted X-ray flux perpendicular to the disc plane. The resulting radiation pressure produces a nonaxisymmetric torque leading to a warp or modification of a warp. This was later supported by a study by Pringle (1996) who showed that for a range of accretion luminosities, radiation pressure alone is sufficient to drive and maintain a disc warp. Although a nonaxisymmetric torque (or nonuniform distribution of forces) could mean that the disc should not be flat initially, Pringle (1996) and Maloney, Begelman & Pringle (1996) showed that an accretion disc can still be warped even if it is initially flat as long as the disc is optically thick and the radiation received at a given point on the disc surface is re-radiated from the same point. The resulting back reaction from the re-radiated flux then gives rise to an uneven distribution of forces on the disc surface resulting in substantial warping, provided the luminosity of the central source is high enough, i.e. exceeding a critical value (Pringle, 1996,1997) to overcome the viscous torque that resists warp, driving a warping mode which grows with time (see Iping

& Pertterson, 1990, for detailed discussion).

Assuming the re-radiation is isotropic over the disc surface, the resulting reaction force on an element of area dA on the disc surface at radius R produces a force dF given by (Frank, King & Raine, 2002, p.136)

$$dF = \frac{2}{3}\frac{L_*}{4\pi R^2 c}\ dA, \tag{3.1}$$

where L_* represents the central irradiation luminosity. This force acts inwards on the disc along the normal to the disc. As mentioned above, if the disc is symmetric, the resultant force on the disc surface will balance and the net torque on the disc will be zero and no warping takes place.

Frank, King & Raine (2002, p.136) considered the case where a small perturbation in the disc can cause one side of the disc to receive more radiation and begin to warp at some radius. This was done by comparing the radiation torque producing the warp, $d\Gamma_{\rm rad} \sim RdF$, with the viscous torque resisting the warp, $d\Gamma_{\rm visc}$, at a disc radius R. The viscous torque can be considered to have two components (Pringle, 1992): one associated with the usual disc viscosity ν_1 (corresponding to azimuthal shear), which acts between annuli rotating at different angular velocity, and the other associated with the viscosity ν_2 (corresponding to the vertical shear) that acts to reduce or resist any disc warp or tilt.

Taking the element of area $dA = 2\pi RdR$ and using Equation (3.1), Frank, King & Raine (2002, p.136) expressed the radiation torque as

$$\frac{1}{2\pi R}\frac{\partial \Gamma_{\rm rad}}{\partial R} \sim \frac{L_*}{6\pi Rc}. \tag{3.2}$$

The viscous torque always tries to restore the disc to a flat shape, i.e. resists any warp resulting from the radiation torque. Therefore for the disc to warp the radiation torque should exceed the

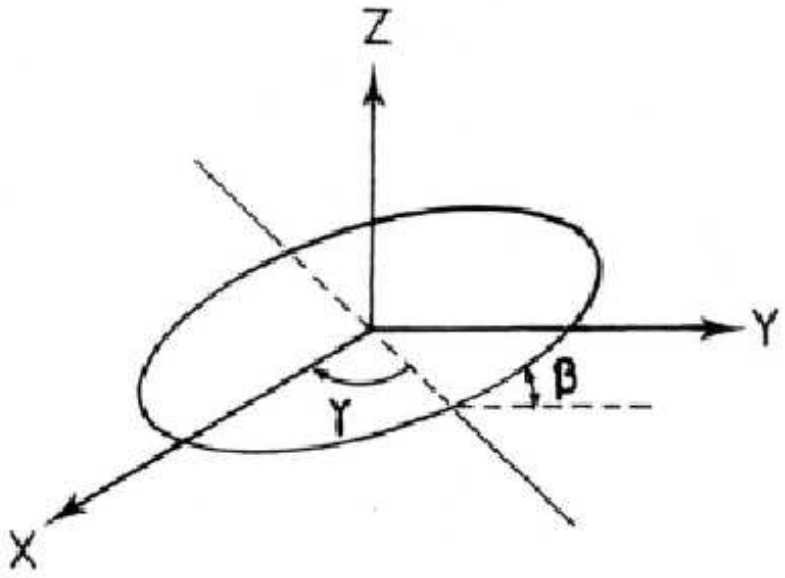

Figure 3.1: Orientation of a disc described by the angles $\beta(R,t)$ and $\gamma(R,t)$. (*Adopted from Iping & Petterson, 1990).*

viscous restoring torque, i.e. $d\Gamma_{\rm rad} > d\Gamma_{\rm visc}$.

In an accretion disc mass flows inwards (towards the central accreting object) carrying with it mass and angular momentum. Considering an accretion disc divided into annuli of width $\triangle R$, i.e. lying between radii R and $\triangle R$, the total mass and angular momentum of an annulus are given by $2\pi R\triangle R\Sigma$ and $2\pi R\triangle R\Sigma R^2\Omega$ respectively, where $\Sigma(R,t)$ is the surface density of the disc and $\Omega(R,t)$ the angular velocity.

If the angle of tilt of the disc plane is $\beta(R,t)$ and $\gamma(R,t)$ describes the azimuth of the tilt (Figure 3.1), the unit tilt vector normal to the disc plane at radius R is given by (Pringle, 1996)

$$\hat{l}(R,t) = (\cos\gamma\,\sin\beta,\ \ \sin\gamma\,\sin\beta,\ \ \cos\beta). \tag{3.3}$$

From the conservation of angular momentum, taking into account the effects of the net restoring viscous torque, the resultant restoring viscous torque on the disc annulus of radial extent dR can be expressed in the form (e.g. Frank King & Raine, 2002, p.136)

$$\frac{1}{2\pi R}\frac{\partial \Gamma_{\rm visc}}{\partial R} = \Sigma R^2 \Omega \left(\frac{\partial}{\partial R}\right)\left(\nu_2 \frac{\partial \hat{l}}{\partial R}\right) \sim \nu_2^2 \Sigma \Omega. \tag{3.4}$$

The discussion presented above laid the foundation for the Pringle (1996, 1997) disc dynamics analysis that leads to warping of an accretion disc which will be briefly reviewed.

The equation of the evolution of a local disc tilt $\hat{l}(R,t)$ (Pringle, 1992) can be expressed, including the radiation-driven back-reaction, by adding a term describing radiation torque (Pringle, 1996, 1997) as

$$\begin{array}{l} \frac{\partial \hat{l}}{\partial t} + \left(v_R - \frac{\nu_1}{\Omega}\frac{\partial \Omega}{\partial R} - \frac{1}{2}\frac{\nu_2}{\Sigma R^3 \Omega}\frac{\partial}{\partial R}(\Sigma R^3 \Omega)\right)\frac{\partial \hat{l}}{\partial R} \\ = \frac{\partial}{\partial R}\left(\frac{1}{2}\nu_2 \frac{\partial \hat{l}}{\partial R}\right) + \frac{1}{2} \mid \frac{\partial \hat{l}}{\partial R} \mid^2 \hat{l} + \frac{1}{\Sigma R^2 \Omega}\frac{\partial \mathbf{L}}{\partial t}, \end{array} \tag{3.5}$$

where $\mathbf{L}(R,t)$ is the angular momentum per unit surface area defined by $\mathbf{L} = (GM_* R)^{1/2}\Sigma \hat{l}$, with M_* representing the mass of the compact accreting object and $v_{\rm R}$ the radial velocity.

By taking a very small approximation of the angle β such that $\beta << 1$, Pringle (1996) expressed the unit tilt vector (Equation (3.3) as

$$\hat{l} = (\beta \cos\gamma,\ \ \beta \sin\gamma,\ \ 1). \tag{3.6}$$

This allowed the evolution of $\hat{l}$ to be re-written in the form

$$W = \beta e^{i\gamma}. \tag{3.7}$$

For a steady disc, to investigate the evolution of an initially small warp, Pringle (1996) showed that the equation for $\hat{l}$, (i.e. Equation(3.5)), assuming a constant ν_2, can be expressed in the

form

$$\frac{\partial W}{\partial t} + i\Gamma_{\rm rad}\frac{\partial W}{\partial R} - \frac{1}{2}\nu_2\frac{\partial^2 W}{\partial R^2} = 0, \tag{3.8}$$

where the radiation torque is measured by

$$\Gamma_{\rm rad} = \frac{L}{12\pi\Sigma R^2\Omega c}. \tag{3.9}$$

Assuming a solution of the form

$$W \propto exp[i(\sigma t + kR)], \tag{3.10}$$

where $kR \gg 1$, Equation (3.8) gives the relation

$$\sigma = -i\left(\Gamma_{\rm rad}k - \frac{1}{2}\nu_2 k^2\right). \tag{3.11}$$

From Equation (3.11) the instability (warp) will decay with time for all values of the wave number k if $\Gamma_{\rm rad} = 0$, i.e. Im$(\sigma) > 0$; while an initially small instability (warp) will grow with time for all values of the wave number in the range

$$0 < k < \frac{2\Gamma_{\rm rad}}{\nu_2}, \tag{3.12}$$

as long as Im$(\sigma) < 0$. It is therefore physically possible that over large enough lengthscales in the disc, the radiation pressure can cause an initially flat disc to become warped. The radial wavelength of the perturbation $\lambda_{\rm R} = 2\pi/k$ ($\lambda_{\rm R} \leq R$ for cylindrical geometry), together with the definition of the radiation torque $\Gamma_{\rm rad}$ allows the condition for radiation-driven warping to be expressed as

$$L_* \geq 12\pi^2\nu_2\Sigma v_\phi c, \tag{3.13}$$

where $v_\phi = R\Omega$ is the azimuthal disc velocity. Using the simple argument that $\Gamma_{\rm rad} > \Gamma_{\rm visc}$, from Equations 3.2 and 3.4, it can be shown that the condition for warping to occur is $L_* > 6\pi^2\nu_2\Sigma v_\phi c$ (e.g. Frank, King & Raine 2002, p.137). This analysis did not take into account the

decay and growth of the warping and this makes the analysis of Pringle (1996) more appropriate.

Expressing the surface density (Pringle, 1996) as $\dot{M} = 3\pi\nu_1\Sigma$ and the efficiency of the accretion process by $\varepsilon = L_*/\dot{M}c^2$, the condition for an instability to grow at a given radius R can be expressed as

$$R \geq \frac{8\pi^2\eta^2}{\varepsilon^2} R_{\rm s}, \tag{3.14}$$

where $R_{\rm s} = 2Rv_\phi^2/c^2$ and $\eta = \nu_1/\nu_2$. This gives the critical radius beyond which discs are unstable to warping as

$$R_{\rm c} \gtrsim \frac{8\pi^2\eta^2}{\varepsilon^2} R_{\rm s}. \tag{3.15}$$

Assuming that for an accretion-powered central object of radius R_* the accretion efficiency is $\varepsilon \sim R_{\rm s}/R_*$, the critical radius beyond which warping modes take place is given by

$$R_{\rm c} \gtrsim 8\pi^2\eta^2 \frac{R_*^2}{R_{\rm s}}. \tag{3.16}$$

Using Equation (3.16) and the parameters applicable to neutron stars, Pringle (1996) showed that for $\eta \sim 1$, warping occurs in the outer regions of the accretion disc which confirmed the calculations of Iping & Petterson (1990), who showed that radiation-driven warping occurs in the outer regions of the accretion discs in X-ray binaries.

Maloney, Begelman & Pringle (1996), applied the Pringle (1996) radiation-driven instability to the disc of the maser in NGC 4258 and the eclipsing X-ray binary system SS 433. They found that the predictions of the Pringle radiation-driven warping instability model are in good agreement with the observations of NGC 4258 (Miyoshi et al., 1995) for $\varepsilon \sim 0.1$; although the model cannot explain the warp for the case where NGC 4258 possesses an advective-dominated accretion disc with $\varepsilon \sim 10^{-3}$ suggested by Lasota et al. (1996). They also showed that the Pringle model can explain the 164-day precession period in SS 433 for reasonable values of α

(dimensionless viscosity parameter, Shakura & Sunyaev (1973)) and R/h, where h is the disc scale height.

Radiation-driven warping therefore provides a mechanism for producing warped precessing accretion discs in accreting X-ray binaries (e.g. Ogilvie & Dubus, 2001) and AGNs (Caproni et al., 2006b). Since the warp adjusts itself so as to precess at a uniform rate at all radii (Maloney, Begelman & Pringle 1996), radiation-driven disc precession is a global disc mechanism. It was noted (Maloney Begelman & Nowak, 1998) that radiation-driven disc precession must be prograde in the absence of external forces. In the X-ray binaries SS 433, Her X-1, and LMC X-4 the disc precession is retrograde. Studies by Maloney & Begelman (1997) and Maloney, Begelman & Nowak (1998) have shown that the quadrupole torque from a companion star allows for the existence of prograde and retrograde precession modes. This implies that retrograde precession due to the radiation-driven mechanism is possible only if some additional force acts on the disc. Although Maloney, Begelman & Pringle (1996) pointed that the radiation-driven instability model can produce warped precessing discs in AGNs, Caproni et al. (2006b) showed that for $\eta \neq 1$, the critical radius is larger than the outer disc radius for all the AGNs considered in their sample, suggesting that AGN disc are stable against radiation torque (stable to radiation-driven warping).

3.2.2 Magnetically-driven Instability

Several studies have been carried out on the interaction between the magnetic field of an accreting compact object and the accretion disc in close binary systems. These include the following: Pringle & Rees (1972) outlined the disc-magnetosphere interaction following the discovery of accretion powered X-ray pulsars; Terquem & Papaloizou (2000) showed that a warp might be induced in a circumstellar disc by the stellar magnetic field if the magnetic field axis is mis-

aligned with the binary rotation axis; Murray et al. (2002) demonstrated that a warp can be excited in an accretion disc in close binary systems by a dipolar magnetic field centred on the companion star; Lai (1999) described the mechanism by which stellar magnetic field can couple with the disc to induce warping in accretion discs in close X-ray binaries. Similar studies to that of Lai (1999) were done by Shirakawa & Lai (2002a, b) and Lai (2003).

According to the detailed study by Lai (1999), the inner region of an accretion disc around a rotating magnetised compact object is subjected to magnetic torques that induce warping and precession of the accretion disc. Lai (1999) noted that the warping torque results from the interaction of the azimuthal component of the stellar magnetic field and the radial surface current in the disc, generated by twisting of the threaded vertical field component. The precession torque results from the screening current, resulting from the diamagnetic response of the disc.

Following an analysis similar to Pringle (1996), Lai (1999) showed that the equation of evolution of disc tilt, taking into account magnetic torque, can be expressed in the form (e.g. Equation 3.8)

$$\frac{\partial W}{\partial t} = \frac{3\nu_2}{4R}\frac{\partial W}{\partial R} + \frac{1}{2}\nu_2\frac{\partial^2 W}{\partial R^2} - i\Omega_p W + \Gamma_{\rm mg} W \tag{3.17}$$

where $W \equiv \beta e^{i\gamma}$. Assuming a solution of the form in Equation (3.10), the dispersion relation is expressed as (Lai 1999)

$$\sigma = \left(\frac{3\nu^2}{4R}k - \Omega_p\right) + i\left(\frac{1}{2}\nu_2 k^2 - \Gamma_{\rm mg}\right). \tag{3.18}$$

From this dispersion relation, the condition for an instability to grow requires $\mathrm{Im}(\sigma) < 0$), and this gives the magnetic torque as

$$\Gamma_{\rm mg} > \frac{1}{2}\nu_2 k^2. \tag{3.19}$$

Since the radial wavelength is restricted to $\lambda \leq R$, i.e. $k \geq 2\pi/R$, the instability condition can be expressed as

$$\Gamma_{\rm mg} > 2\pi^2 \frac{\nu_2}{R^2}. \tag{3.20}$$

Lai (1999) interpreted this instability condition to mean that the magnetic torque drives the growth of disc tilt on a timescale $\Gamma_{\rm mg}^{-1}$, while viscosity tries to reduce the tilt on a timescale R^2/ν_2. Instability therefore requires

$$\Gamma_{\rm mg}^{-1} \leq \frac{R^2}{\nu_2}. \tag{3.21}$$

Caproni et al. (2006b) examined the compatibility between precession periods and predictions for warping/precession based on the magnetically-driven warping and/or precession to a sample of four X-ray binaries (SS 433, Her X-1, LMC X-4 and SMC X-1) and observed that the magnetically-driven instability produces the observed precession periods in these systems. These authors also noted that the magnetic-driven torque can induce precession in the inner parts of the accretion disc at the observationally inferred rates. Similarly, Boroson et al. (2000) applied the magnetically-driven instability to explain the milli-Hertz quasi periodic oscillations (QPOs) seen in X-ray binaries. Lai (2003) also showed that the magnetically-driven warping and precession effects can explain the jet precession from X-ray binaries, AGNs, and YSOs. The model also predicts a retrograde precession in warped discs (and jets) in agreement with observations in some X-ray binaries, e.g. Her X-1.

3.2.3 Tidally-driven Instability

Tidal effects that result in warping and precession of discs in astronomical objects have been extensively studied (e.g. Goldreich & Tremaine, 1978; Papaloizou & Terquem, 1995; Larwood et al., 1996; Larwood 1997; 1998 Terquem, Papaloizou & Nelson, 1999; Caproni et al., 2006a and references therein; Ann, 2007). These studies have shown that tidal torques induced by the

companion star in binary systems can cause the warping and precession of accretion discs. The tidal interaction between the companion star and the accretion disc also results in truncation of the accretion disc in binary systems (Paczyński 1977; Papaloizou & Pringle, 1977).

Katz (1973) used a model consisting of a tilted accretion disc with respect to the binary plane and a tidally forced model precession to explain the 35-day period in the lightcurve of Her X-1. Waves develop in the disc due to the tidal perturbations of the companion star. In the case where the disc and the orbital plane are coplanar, the waves excited in the disc by tidal perturbations of the companion are density waves (Terquem, Papaloizou & Nelson, 1999). The wavelength of these waves is very small compared to the disc thickness and therefore most of the exchange of angular momentum between the disc and the perturbing companion is likely to take place near the disc edge (Papaloizou & Terquem, 1995). But when the disc and the orbital plane are not aligned (i.e. non-coplanar), the perturbations by the companion star excites both density and bending waves in the disc which give rise to a warped disc.

Caproni et al. (2006b) show that for the case where the orbital plane and the disc are non-coplanar the precession period $P_{\rm p}$ of the disc, induced by tidal torque of the companion star, is given by

$$P_{\rm p} \geq -\frac{8\pi}{3}\left(\frac{5-n}{7-2n}\right)\left(\frac{a^3}{R_{\rm d}}\right)(\sqrt{GM_*}\, q\, \cos\beta)^{-1}, \tag{3.22}$$

where a is the separation of the companion and compact stars, $R_{\rm d}$ the radius of the precessing disc, n the polytropic index of gas, M_* the mass of the compact star, $q = M_{\rm c}/M_*$ with $M_{\rm c}$ representing the mass of the companion star, and β the inclination of the orbit with respect to the disc plane. In Equation 3.22, the negative sign indicates that the disc precession is retrograde.

Caproni et al. (2006b) showed that tidal torques from the companion star can provide precession

timescales in agreement with those observed in the X-ray binaries SS 433, Her X-1, LMC X-4 and SMC X-1 as previously suggested (Katz, 1973; Larwood, 1998). They also showed that tidal torques can drive precession in 4U 1907+09. Lachowicz et al. (2006) noted that precession in Cyg X-1 is in the prograde direction and this rules out the tidally driven precession in Cyg X-1 in agreement with the study by Caproni et al. (2006b).

3.2.4 Wind-driven Instability

Schandl & Mayer (1994) and Schandl (1996) proposed the wind-driven instability as a probable mechanism to explain the warped precessing disc in the X-ray binary Her X-1. When X-ray flux from the central accreting source strikes the accretion disc surface it produces a hot corona (Shakura & Sunyaev, 1973). They noted that at the outer radii the sound velocity of the hot gas exceeds the escape velocity in the gravitational potential at the outer regions of the disc, thus forming a coronal wind. The wind carries off momentum and this provides a back-force on the disc surface, similar to the radiation-driven mechanism.

Although the Schandl & Mayer (1994) coronal wind model is likely to produce a disc warp, from later studies (Pringle, 1996; Wijers & Pringle, 1999) it was noted that simple calculations based on the Schandl & Mayer model are not adequate for the proper analysis of such a physical configuration. Wijers & Pringle (1999) further noted that Schandl & Mayer (1994) neglected self-shadowing and used an older and incorrect equation of motion for the disc.

3.2.5 Frame Dragging and Disc viscosity: The Bardeen-Petterson Effect

The Lense-Thirring (or frame dragging) effect by a spinning compact object causes a precession of the inner accretion disc if the disc is not in the equatorial plane of the compact object (Bardeen & Petterson, 1975). Later studies (Stella & Vietri, 1998; Markovic & Lamb, 1998) have subsequently suggested the Lense-Thirring effect as the probable physical mechanism responsible for the observed periodic oscillations in astrophysical systems. It has been pointed out (Bardeen & Petterson, 1975) that the differences in structure between a disc in the equatorial plane and a disc in a tilted plane arises because the gravitational field of the compact object is not spherically symmetric, and the dominant non-spherically symmetric effect on test-particle at radii $R \gg R_*$ (R_* is the radius of the compact object) is the coupling between the spin of the compact object and the orbital angular momentum of the test particle. This causes the precession of the plane of a circular geodesic orbit about the rotation axis of the compact object. The precession frequency produced by the Lense-Thirring effect can be expressed as (Wilkins, 1972)

$$\omega_{\rm LT} = \frac{2GJ}{c^2 R^3}, \tag{3.23}$$

where J is the angular momentum of the compact object and G the gravitational constant. Using gravitational units (Bardeen & Petterson, 1975) $G = c = 1$ the equation for $\omega_{\rm LT}$ simplifies to

$$\omega_{\rm LT} = 2JR^{-3}. \tag{3.24}$$

A combined effect of the Lense-Thirring and internal viscosity of an accretion disc tends to smooth out such precession which results in an equilibrium state in which the inner disc is aligned with the spin axis of the compact object at a transition radius called the Bardeen-Petterson radius, $R_{\rm BP}$. Papaloizou & Lin (1995) suggested that the transition between the diffusive and wave-like regimes occurs approximately at a radius $R_{\rm T} \sim h/\alpha$; and Demianski & Ivanov (1997), and Lubow, Ogilvie & Pringle (2002) suggested that a warped configuration may

persist indefinitely within $R_{\rm BP} \leq 200R_{\rm s}$ ($R_{\rm s}$ is the Schwarzchild radius). Caproni et al. (2006b) observed that the Lense-Thirring effect produces precession timescales in good agreement with those observed in a sample of X-ray binaries and AGN sources, considering that alignment of the accretion disc evolves on a similar timescale as was also observed by Scheuer & Feiler (1996). Their work is also in support of the analysis of Caproni et al. (2006a) who showed that the Lense-Thirring effect is consistent with the warping morphology proposed by Gallimore, Baum & O'Dea (2004). Caproni et al. (2007) have shown that the Bardeen-Petterson effect is responsible for warping of the disc in NGC 4258, and can produce the required precession period.

3.3 Summary

As already mentioned above, warped precessing accretion discs are now believed to occur in many astrophysical systems such as X-ray binary systems, AGNs and YSOs, and this has resulted in long term (super-orbital) variations in these systems. In X-ray binaries, the super-orbital variation is divided into two observational classes (Clarkson et al., 2003a): one class has stable X-ray intensity variation giving precession periods on timescales in the range of tens of days. X-ray binaries in this group include Her X-1 with a precession period of ~ 35 days (Giacconi et al., 1973), SMC X-1 with a precession period of ~ 55 days (Wojdowski, Woo & Zhang, 1998; Wijers & Pringle, 1999) and LMC X-4 with a precession period of ~ 30 days (Wijers & Pringle, 1999). In the case of SMC X-1, it was observed (Clarkson et al., 2003b) that

Table 3.1: Table showing super-orbital periods of some astronomical systems.

Name	Super-period	Reference
XRBs		
LMC X-4	30 days	Wijers & Pringle, 1999
Her X-1	35 days	Giacconi et al., 1973
SMC X-1	55 days*	Wojdowski, Woo & Zhang, 1998; Wijers & Pringle 1999
Cyg X-2	70 - 80 days	Paul, Kitamoto & Makino, 2000
GX 354-0	70 days	Kong, Charles & Kuulker, 1998
SS 433	164 days	Margon, 1984
X1820-30	171 days	Chou & Grindly, 2001
AGNs		
Arp 102B	2years	Newman et al., 1997
OJ 287	9 years	Sillanpää et al., 1988; Abraham, 2000
3C 120	12 years	Caproni & Abraham, 2000
YSOs		
Cep E	400 years	Terquem, Papaloizou & Nelson, 1999
V1331 Cyg	2300 years	Terquem, Papaloizou & Nelson, 1999
RNO 15-FIR	9000 years	Terquem, Papaloizou & Nelson, 1999

*The period is not constant, but varies between 40 and 60 days (Clarkson et al., 2003b).

the precession period is not constant, but varies between 40 and 60 days. More recently, Trowbridge, Nowak & Wilms (2007) showed that the length of the super-orbital period in SMC X-1

can vary by a factor of two across adjacent precession cycles. Clarkson et al. (2003b) proposed that the wide range of variation in the super-orbital period in SMC X-1 could possibly be due to multiple warp modes in the accretion disc.

The second class of X-ray binary systems have super-orbital periods on timescales up to hundreds of days (Smale & Lochner, 1992). The modulations in this second class are distinctly quasi-periodic and are much lower in amplitude (Clarkson et al., 2003). These include Cyg X-2 with period $\sim 70 - 80$ days (Paul, Kitamoto & Makino, 2000), GX 354-0 with period ~ 70 days (Kong, Charles & Kuulkers, 1998), X1820-30 with period ~ 171 days (Chou & Grindly, 2001), SS 433 with period ~ 164 days (Margon, 1984).

In some X-ray binaries, e.g. Cyg X-2, the super-orbital periods have been found to be equal to integer or half integer multiples of the orbital period (Klochkov et al., 2006). Since X-ray binaries are in our galaxy, they are the best nearby examples of warped precessing discs and most studies on warped precessing discs have been done on them.

Warped precessing discs have also been observed in AGNs in the form of variations in jet orientation and velocity (Storchi-Bergmann et al., 2003; Caproni & Abraham, 2004 and Caproni et al., 2007). The precession periods in AGNs are on timescales of years, e.g. 3C 120 with precession period of 12 years (Caproni & Abraham, 2004), OJ 287 with period of ~ 9 years (Sillanpää et al., 1988; Abraham, 2000), Arp 102B with a period of ~ 2 years (Newman et al., 1997). Like AGNs, the evidence for jet precession in YSOs, also as a result of precessing warped discs, is steadily increasing (Terquem et al., 1999; Bate et al., 2000; Lai, 2003). In YSOs the timescale for the precession is of the order of hundreds of years, e.g. Cep E has a precession period of ~ 400 years, V1331 Cyg ~ 2300 years and RNO 15-FIR ~ 9000 years

(Terquem, Papaloizou & Nelson, 1999). Table 3.1 shows super-orbital periods of some of the systems mentioned in this thesis. Since this thesis focuses on the anomalous low state of Her X-1, a general discussion of Her X-1 is presented below.

3.4 Hercules X-1

Her X-1 is an eclipsing X-ray binary containing a $1.4M_{\odot}$ (Reynolds et al., 1997) pulsar (neutron star) and the companion (optical) star HZ Hercules (HZ Her) is a $2.2M_{\odot}$ A7 Roche-lobe filing star (Middleditch & Nelson, 1976; Leahy & Scott, 1998). It is viewed close to edge-on, i.e. has an inclination of $\sim 80^{\circ} - 90^{\circ}$ (Schandl, 1996, and references therein). Although mass transfer in Her X-1 is believed to occur primarily through Roche-lobe overflow (Figure 3.2), there seems to be also observational and theoretical evidence for mass transfer through stellar wind (Boroson et al., 2007, and references therein). Her X-1 has a pulse period of 1.24 s and an orbital period of 1.7 days (Tananbaum et al., 1972). In addition, it displays a ~ 35 day super-period detected in the X-ray (Giacconi et al., 1973; Scott, Leahy & Wilson, 2000) and optical (Deeter et al., 1976; Gerend & Boynton, 1976; Leahy & Marshall, 1999) wavelengths.

Photometric variations show a 1.62 day beat period between the super-period and the orbital period. The photometric variations are a result of the change in the area of the disc facing the observer and also the variation in the fraction of the secondary star being eclipsed by the disc resulting in a variation in X-ray illumination of the star (Gerend & Boynton, 1976). It has been observed (Giacconi et al., 1973; Schandl, 1996; Scott & Leahy, 1999; Klochkov et al., 2007, and references therein) that in addition to the super-orbital variation and eclipses by the companion star, the X-ray intensity displays three types of dips:

(i) The pre-eclipse dips which occur just before eclipse and are observed up to several binary

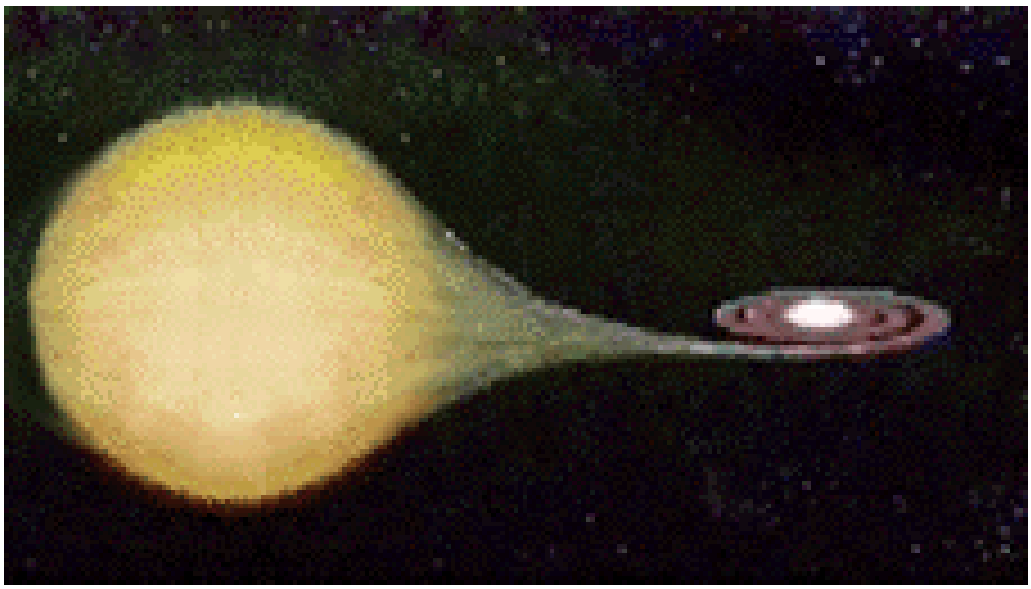

Figure 3.2: Schematic picture of a standard X-ray binary transferring mass by Roche-lobe overflow. (*Adopted from* www.mssl.ucl.ac.uk/www_astro/gal/gal_title.html).

orbits after turn-on at orbital phases $\phi_{\rm orb} = 0.6 - 0.9$ and lasts for $\sim$2 to 5 hours. It has been shown (Boroson et al., 2007 and references therein) that the pre-eclipse dips occur with a period of 1.65 days

(ii) The anomalous dips which occur just after turn-on at orbital phases around $\phi_{\rm orb} = 0.45 - 0.65$.

(iii) The post-eclipse recoveries observed occasionally as a short delay after egress from the X-ray eclipse in the first orbit after turn-on.

The anomalous dips are attributed to the interaction between the accretion stream and the precessing warped accretion disc (Schandl, 1996). More recently, Klochkov et al., (2007), using RXTE/ASM X-ray lightcurves showed that the anomalous dips and post-eclipse features are stable in the X-ray lightcurve and argued that these features could be caused by a warp/tilt of

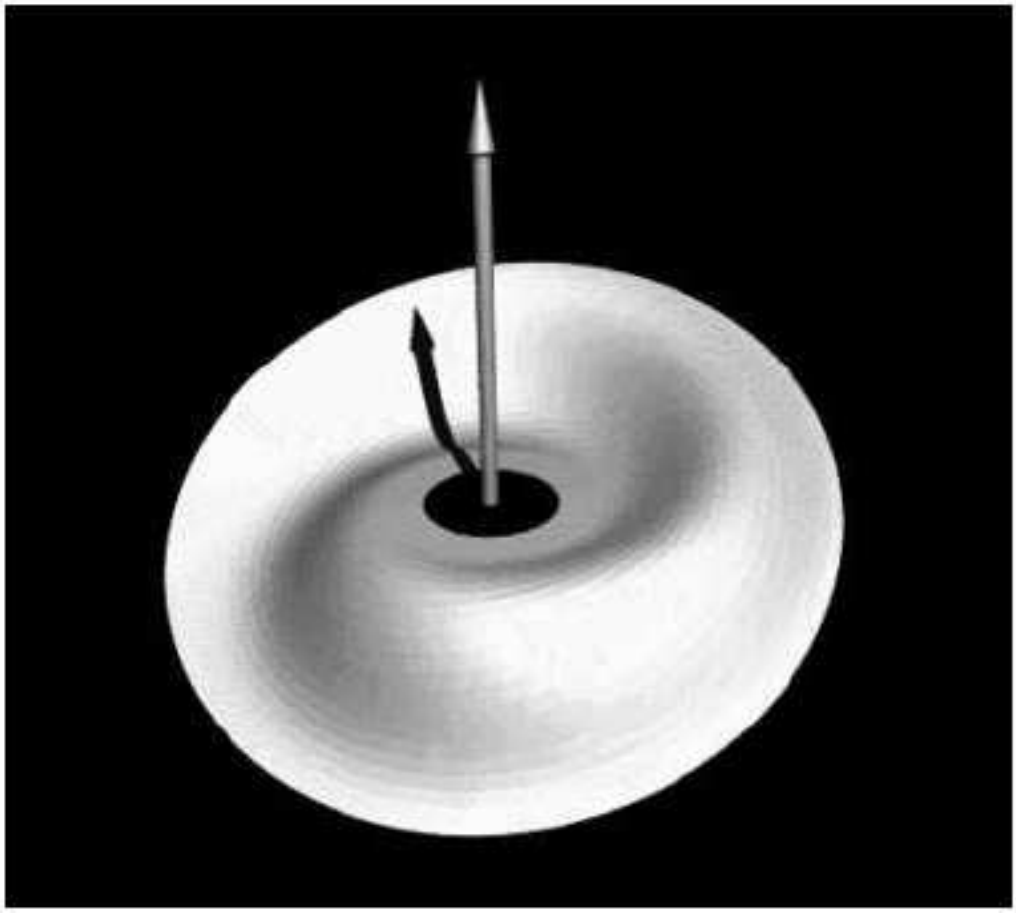

Figure 3.3: Schematic picture of a warped precessing disc. (*Adopted from Wijers & Pringle, 1999*).

the accretion disc which changes over the 35-day cycle.

Since the discovery of Her X-1 (Tananbaum et al., 1972) by *Uhuru*, long-term X-ray monitoring of Her X-1 has continued over the years and these have enabled studies of the ~ 35-day cycle of Her X-1. Some of these studies include the following: Using the Uhuru observations (Tananbaum et al., 1972; Giacconi et al., 1973; Jones & Forman, 1976), the features of the of the 35-day lightcurve, e.g. the high and low states, high state eclipses, absorption dips and

the tendency of the main high states to turn on near orbital phase 0.2 and 0.7 were discovered. Soong et al. (1990) used the HEAO 1 observation in the energy range 12 - 180 keV to study the long-term variability of the pulse profile of Her X-1. This study showed that the structural change of the accretion disc is likely the cause of the 35-day precession period and the observed short-term rapid variations of the pulse profile.

By studying the long term behaviour of the pulse period and precession cycle of Her X-1, Staubert et al. (2007) showed that there is a correlation between these periods, i.e. when the spin-up rate decreases, the 35-day turn-on becomes shorter. They suggested the variation in the mass accretion rate as the probable cause of this correlation. Parmar, Sanford & Fabian (1980) obtained detailed spectra of Her X-1 with the Ariel V satellite during turn-on and off states. They found that the obscuring region assumed to be responsible for the 35-day precession cycle lies well within the disc surrounding the neutron star. Choi et al. (1997) analysed the ASCA data of Her X-1 obtained during the extended low intensity state in 1993 and found that the eclipse ingress and egress during this low state show a smooth flux variation on a timescale of $\sim$3 hours. They interpreted this to mean that the X-ray emission region in the low state is extended because such long transition is not expected with only the atmospheric occultation of the X-ray source (Leahy & Yoshida, 1995). All these studies confirmed many of the X-ray phenomena first reported with the Uhuru observations and also added significant details and discovered new phenomena like eclipses during the low state (e.g. Parmar, Sanford & Fabian, 1980; Choi et al., 1997) and an extended low state (e.g. Ögelman & Trümper, 1988).

A number of scenarios have been proposed to explain the super-orbital period in X-ray binaries as discussed above and these include among others, e.g. precession of the magnetic axis of the compact object (Trümper et al., 1986), presence of a third body in the X-ray binary orbit causing

orbital precession and decay (Chou & Grindlay, 2001) and variation in the extend to which the companion overflows its Roche lobe as a result of stellar pulsation (Wehlau et al., 1992). However, a warped accretion disc (Gerend & Boynton, 1976; Petterson, 1977) precessing in a retrograde direction around the compact neutron star (Figure 3.3) (Roberts, 1974) seems to be the most likely candidate to explain the super-orbital period in Her X-1. The disc precession causes periodic obscuration of the central source causing variation on the 35-day period (Wijers & Pringle, 1999; Ogilve & Dubus, 2001). The next chapter, focuses on the 35-day cycle of Her X-1, which results from precession of a warped accretion disc.

Chapter 4

The 35-day Cycle of Hercules X-1

4.1 Introduction

Her X-1 shows strong variability on both short and long time scales. Of interest in this chapter is the 35-day cycle, the so-called super-period, that shows strong modulation in X-ray wavelengths. The 35-day cycle is also observed in the optical wavelengths (Gerend & Boynton, 1976) and is consistent with the model of a warped accretion disc shadowing the companion star (this is discussed in Chapter 5). As previously mentioned in Chapter 3, in the case of Her X-1, the 35-day cycle is believed to result from the occultation of the neutron star by a warped disc precessing around the central neutron star.

The 35-day periodicity is characterised by a main high state, called the main-on, lasting about 10 days and a short high state, called the short-on, lasting about 5 days. These high states are separated by a 10 day low state, called the off state (Giacconi et al., 1973; Mihara et al., 1991; Scott & Leahy, 1999) (see Figure 4.1 and 4.6). A further 10 day low state follows the short high state to complete the 35-day cycle. The transition from the off state to the main-on state lasts a few hours while the short-on state is entered into gradually (see Figure 4.6). Weak pulsations from the neutron star can be detected, which has been interpreted as scattered radiation from

the accretion disc corona (Pravdo et al., 1979; Mihara et al., 1991 and Coburn et al., 2000). The transition from the off state to the main-on state, called the turn-on, occurs at orbital phases $\phi_{\rm orb} = 0.2$ and $\phi_{\rm orb} = 0.7$ (Schandl 1996; Scott & Leahy, 1999). Schandl proposed that the turn-on at these orbital phases results from the accretion stream overflowing the disc. Klochkov et al. (2006) suggested that at these orbital phases the angle between the disc plane and the line of sight of the observer changes rapidly.

The intensity variation in the 35-day cycle of Her X-1 is attributed to the periodic obscuration of the central source by a warped accretion disc. Following the model proposed for Her X-1 (Scott, Leahy & Wilson, 2000), the turn-on to the main-on and short-on states starts when the outer disc rim opens the line of sight to the central neutron star, while the drop in flux at the end of these states starts when the inner parts of the disc start to cover the line of sight to the central neutron star (Figure 4.1). A schematic picture of a warped precessing disc is shown in Figure 3.3. Figure 4.1 shows the inner and outer disc edges as seen by an observer on the neutron star. The elevation of the observer is -5° (indicated by the dashed horizontal line). According to the Scott, Leahy & Wilson (2000) model an increase in the elevation of the observers line of sight, with respect to the outer disc plane, results in a decrease in the amount of obscuration of the neutron star.

The probable mechanisms responsible for disc warp and precession have already been discussed in Chapter 3. The X-ray spectra of Her X-1 at different phases of the 35-day cycle can be fitted using a constant-emission model and adding one or more absorption components which vary in column density over the 35-day period reaching a maximum value during the low states (Leahy, 2001; Still et al., 2001b). This supports the scenario that the 35-day period is due to accretion disc precession, periodically obscuring the accreting compact star.

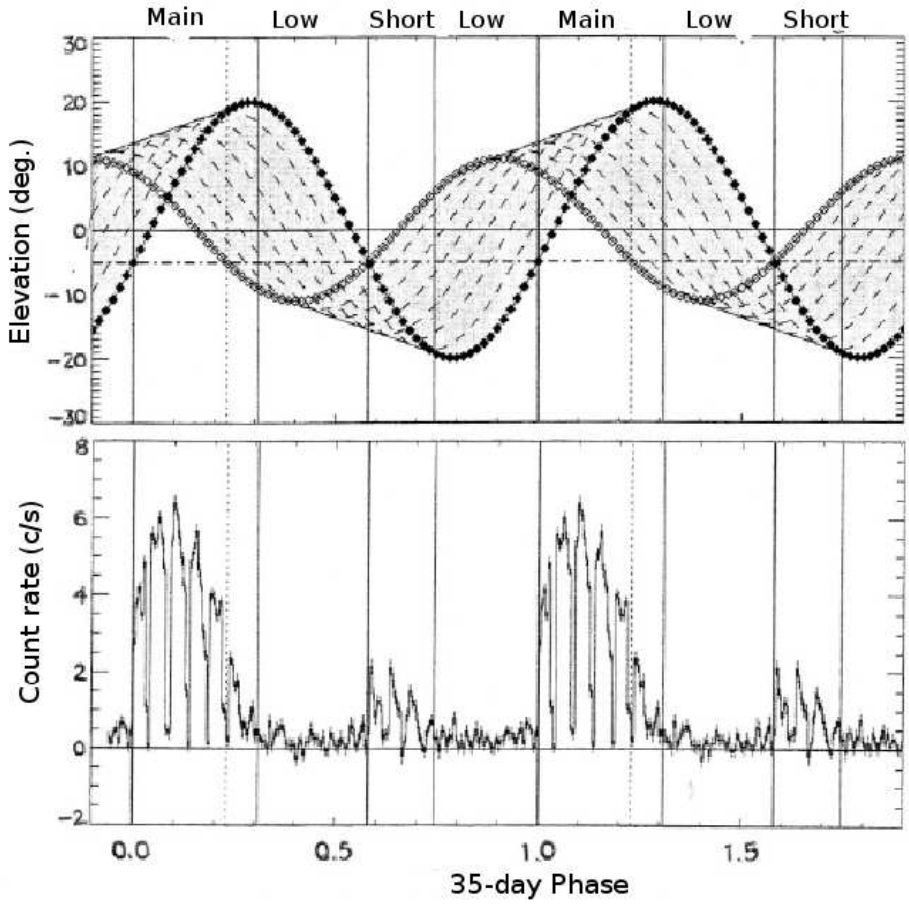

Figure 4.1: The rim of an accretion disc as seen by an observer on the neutron star. The outer and inner disc edges are indicated by filled and open diamonds respectively. Main, low and short represent the main-on, off and short-on states respectively . The bottom panel shows the variation of X-ray intensity of Her X-1 over the 35-day precession cycle (*Adopted from Scott, Leahy & Wilson, 2000*).

After the launch of the Rossi X-ray Timing Explorer (RXTE) (Levine et al., 1996), Her X-1 has been monitored continuously by the All Sky Monitor (ASM) on board RXTE in the energy range 1.5 - 12 keV. This has allowed the study of the systematics of the 35-day precession pe-

riod and the orbital lightcurves of Her X-1 (e.g. Scott & Leahy, 1999; Clarkson et al., 2003a; Still & Boyd, 2004; Kuster et al., 2005). Using the RXTE ASM count rates from Her X-1, Still & Boyd (2004) (Hereafter SB04) recalculated the precession ephemeris using cycles for a period of over 3.5 years. They also used the Compton Gamma Ray Observatory (CGRO) Burst And Transient Source Experiment (BATSE) (20 - 50 keV) one day average count rates data for the period between 1991 and 1999. SB04 showed using both RXTE ASM and CGRO BATSE data that each ALS is accompanied by a change in precession period and the subsequent period change is correlated to the accretion flux. This change in the precession period after each ALS was initially interpreted by Clarkson et al. (2003a) as a phase shift. Although it was initially suggested (e.g. Ögelman, 1987; Scott & Leahy, 1999) that the duration of the 35-day cycle of Her X-1 is not strictly periodic but shows a variation of 20, 20.5 or 21 times the binary orbital period, SB04 for the first time, showed that the precession period of Her X-1 is regular rather than random as previously suggested.

Since the discovery of the 35-day cycle of Her X-1, there are occasions where it failed to reach its high state, i.e. it missed a number of consecutive 35-day cycles, a state called the Anomalous Low State (ALS). The first ALS was detected in June 1983 (Parmar et al., 1985) and lasted up to March 1984. Subsequent ALS were observed in August 1993 (Vrtilek et al., 1994; Mihara & Soong, 1994); in the late months of 1997 (SB04), in April 1999 (Levine, 1999; Parmar et al., 1999; Coburn et al., 2000; Oosterbroek et al., 2000); while the most recent occurred in the late months of 2003 (Boyd & Still, 2004; Boyd, Still & Corbet, 2004). Each of these ALS lasts several 35-day cycles (Still et al., 2001a). The possible cause of the ALS seems to be a change in the state of the accretion disc or an increase in the vertical extent of the warp (Schandl & Meyer 1994; Schandl, 1996). Recent studies (Parmar et al., 1999; Coburn et al., 2000; Oosterbroek et al., 2001) show that the ALS is accompanied by rapid spin-down of the pulse period in which

the spin-down rate is faster than the spin-up rate during normal X-ray output. It is also known that X-ray pulsation is visible during the ALS. If the ALS is a result of a change in the extent or shape of the disc, then it is most probable that there is a change in the mass transfer rate too, i.e. this is an intrinsic change in the source property, not just a line of sight effect. SB04 showed that after each ALS, Her X-1 turns on with a different precession period and main-on state count rate, with the precession period being proportional to the main-on state count rate. These authors found that an increase (decrease) in the precession period corresponds to an increase (decrease) in the main-on count rate. SB04 predicted that Her X-1 would return from the 2003 - 2004 ALS with a new precession period and epoch averaged peak main-on flux, which they could not test immediately because there was not enough data by that time. Now that enough data has accumulated, the purpose of this chapter is to perform these tests. The results presented in this chapter are based on observations done with the ASM on board RXTE. Before presenting the results in Section 4.3, a brief overview of RXTE and the ASM is presented in the following section.

4.2 Observations

The Rossi X-ray Timing Explorer (RXTE) is a space telescope that was launched on December 30th 1995 from the NASA's Kennedy space centre using a Delta II rocket into a low-earth orbit at an altitude of 580 km. It has an orbital period of 90 minutes and inclination of 23°. RXTE has an observing period of about 60 - 80 percent of its orbital period because of a gap of 15 - 30 minutes resulting from Earth occultation and the South Atlantic Anomaly (SAA) passage (NASA website: http://rxte.gsfc.nasa.gov/docs/xte/appendix_f.html).

RXTE has three instruments on board (Figure 4.2): two pointed instruments, the Proportional

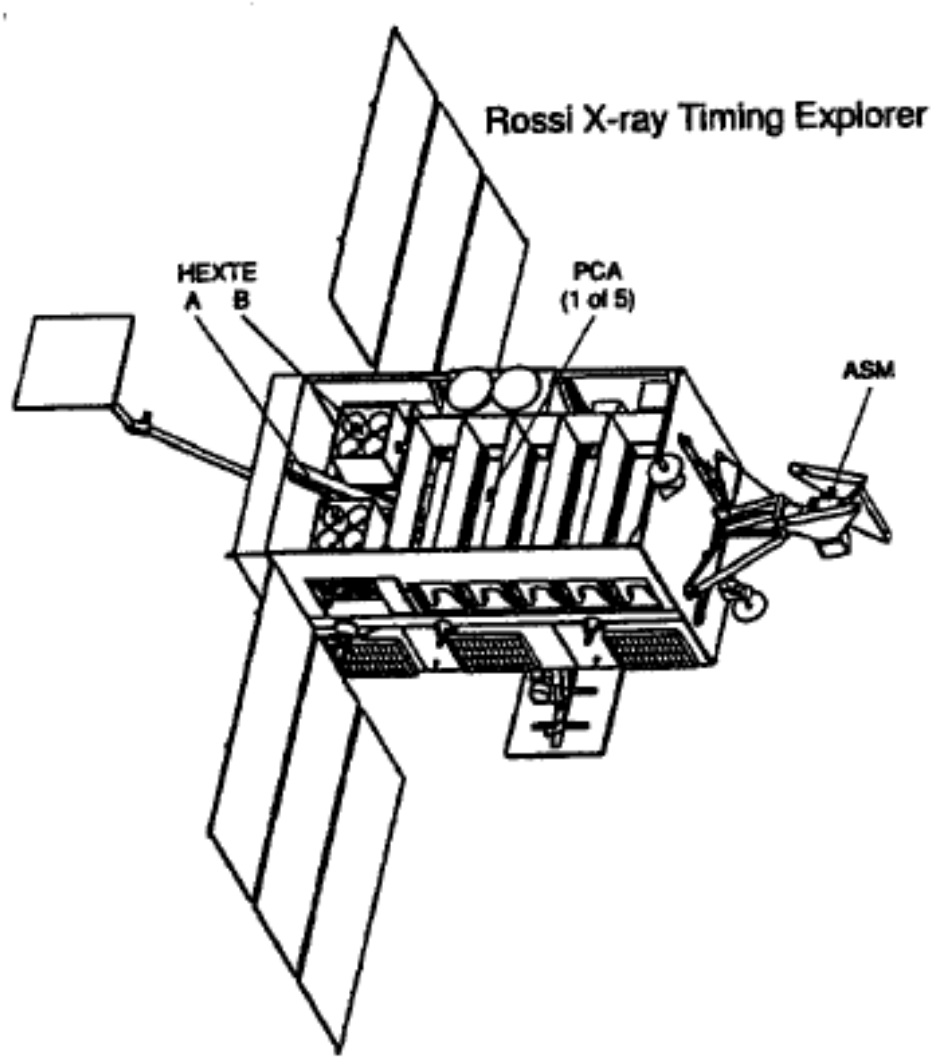

Figure 4.2: Schematic picture of RXTE showing the three instruments on board (*Adopted from Rothschild et al., 1998*).

Counter Array (PCA) and the High Energy X-ray Timing Experiment (HEXTE) which are co-aligned to provide 2 - 250 keV observations of individual sources (Swank et al., 1995) and the third instrument is the All Sky Monitor (ASM).

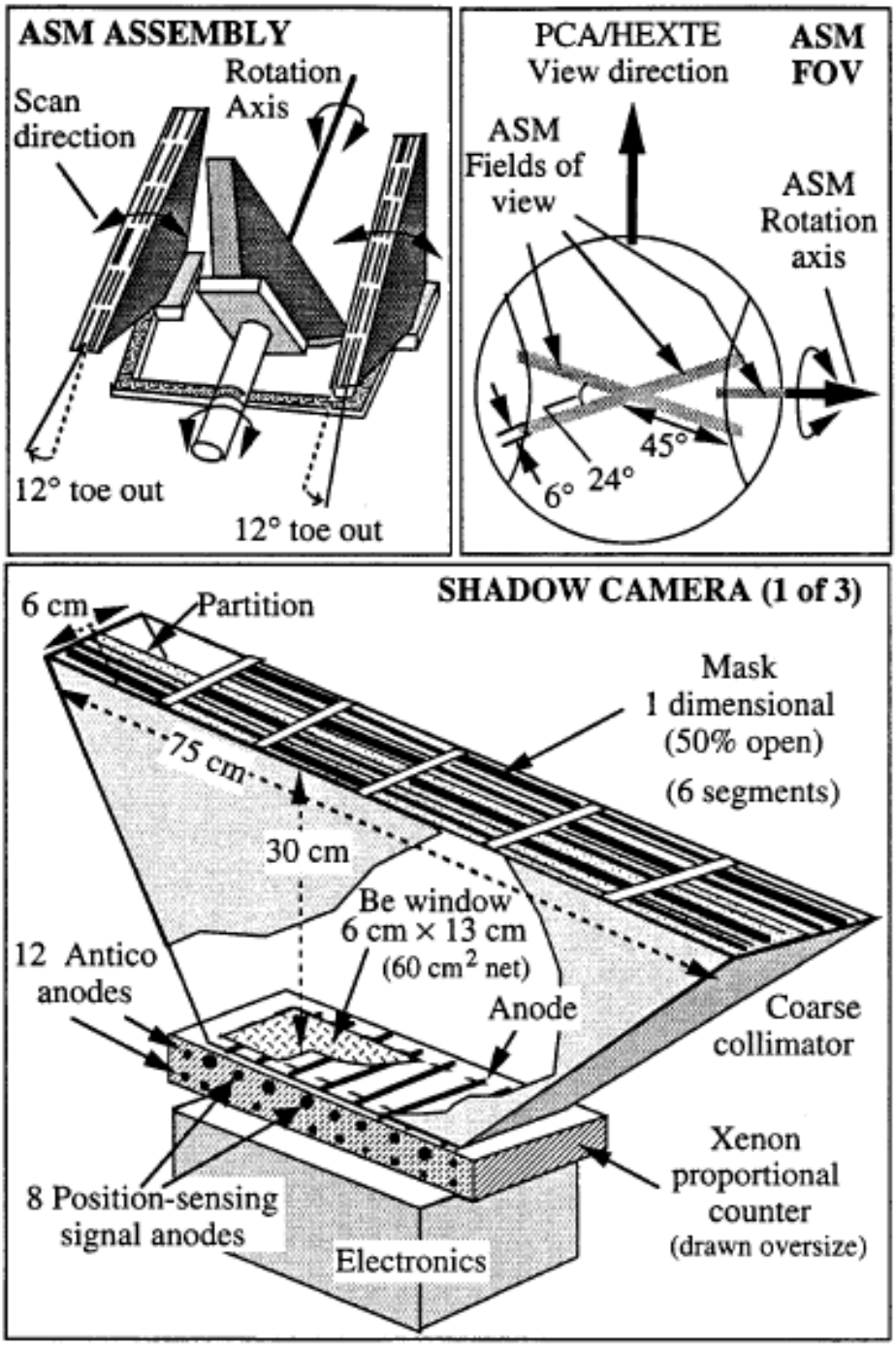

Figure 4.3: Schematic picture of ASM showing the relative orientation of the SSCs (see Levine et al., 1996 for a detailed discussion).

The ASM is a wide field detector that scans the sky every 90 minutes, i.e. every satellite orbit. It consists of three Scanning Shadow Cameras (SSCs) (Figure 4.3) that can be rotated independently by a motor (Levine et al., 1996). It has a field of view of $6^\circ \times 90^\circ$ (Levine et al., 1996), with a spatial resolution of $3' \times 15'$ (Doty, 1994). Each camera is sensitive to energies in the range $\sim$1.5 - 12 keV, which is divided into three energy bands corresponding to A $=$ 1.5 - 3 keV, B $=$ 3 - 5 keV and C $=$ 5 - 12 keV.

In each SSC a Position Sensitive Proportional Counter (PSPC) is mounted and this views the sky through a slit mask. The SSC is based on the principle that an X-ray source at infinity produces a shadow image of the slit mask on the entrance window of the PSPC. The position and flux of the X-ray source is constructed from the analysis of the displacement and intensity distribution of the shadow patterns (Doty, 1994). The ASM data are accumulated in series of ~ 90 s exposures called dwells and during each dwell the spacecraft maintains a fixed altitude and the orientation of each SSC is fixed in relation to the sky. The ASM data consists of dwells taken for each source per day with an exposure time of about 90 seconds once every 90 minutes. In this thesis, ASM count rates from Her X-1 are used to determine precession period after the 2003 -2004 ALS.

4.3 Results

As mentioned above, SB04 re-defined the accretion disc precession ephemeris for the eclipsing X-ray pulsar Her X-1, and predicted that Her X-1 would return from the 2003 - 2004 ALS with a new precession period and epoch averaged peak main-on flux. Therefore, for the purpose of comparison, the results obtained in this analysis (epoch 5) are added to the results of SB04.

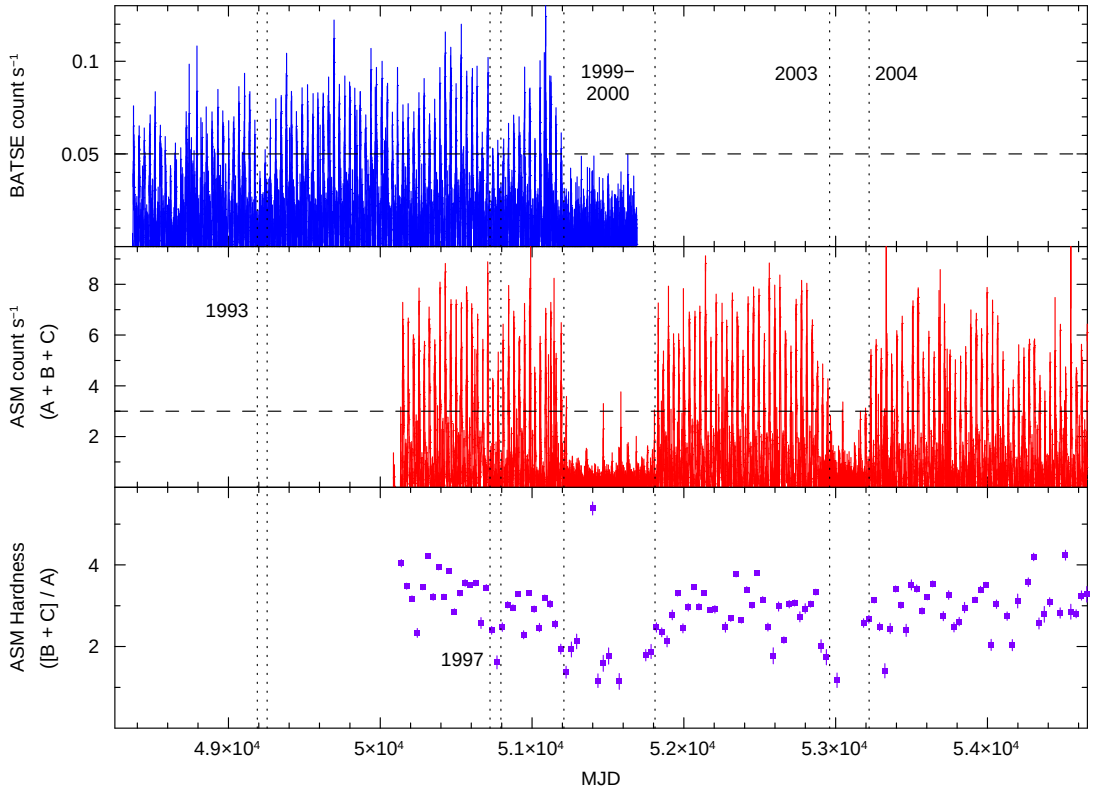

Figure 4.4: Lightcurve of RXTE ASM 24 hour average count rates from Her X-1 for the period 1996 to July 2008 shown in the middle panel. In the top panel is the CGRO BATSE one day average count rates between 1991 and 1999 (SB04) and the bottom panel is the ASM hardness ratio calculated from the daily dwells. In this Figure, the dotted vertical lines represent the start and stop times of each ALS, while the dashed horizontal lines represent the count rate threshold used to analyse the O - C.

A plot of the lightcurve of RXTE ASM (1.5 - 12 keV) 24 hour average count rates from Her X-1 from 1996 to the beginning of July 2008 is shown in the middle panel of Figure (4.4). From this figure, Her X-1 entered the fourth ALS in November 2003 and lasted up to August 2004 and is currently in a high state (by the time of this analysis, in July 2008). Using the three ASM energy bands, the hardness ratio was calculated as 35-day averages and is plotted in the third

panel of Figure (4.4) as a function of time, i.e. Modified Julian Date (MJD). To improve on the error margins, count rates in the dwells with errors $\geqslant$1 were filtered (rejected) as well as hardness ratios with errors $\geqslant$1. As seen from Figure 4.4, there is a clear indication of a close relation between the hardness ratio and the ASM count rates with the hardness ratio softening during the low states.

To determine the precession period after the fourth ALS (Epoch 5) the approach similar to that followed by SB04 was used. The turn-on times for the main-on states are not exactly periodic and therefore for the analysis in this chapter the mid-points of each main-on state, $T_{\rm mid}$, is taken as a reference point i.e. the reference ephemeris adopted (SB04) is

$$T_{\rm mid} = \text{MJD } 50986.7 + 34.79E_{35}, \tag{4.1}$$

where E_{35} is an integer, i.e. the precession cycle number. Using an arbitrary threshold of 3 counts s^{-1} for the current epoch, each data point greater than 3 counts s^{-1} were used to calculate and plot the "observed minus calculated" (O - C) curve of the precession cycle. This is presented in Figure 4.5. In this approach, the quantity subtracted from the ASM times to produce the O - C time series is the nearest $T_{\rm mid}$ to each daily dwell. Individual main-ons are represented by many data points in the O - C curve and the period is calculated from a linear least-square fit to the O - C diagram. This gives a period of 34.76 days with a statistical error of 0.001 day, i.e. $P_{35} = 34.760 \pm 0.001$ days. The derivative $\dot{P}_{35}$ is obtained from a quadratic fit to the O - C diagram and this gives a value of $\dot{P}_{35} = 6 \times 10^{-9}$ with a statistical error of 4×10^{-9}, i.e. $(\dot{P}_{35} = 6 \pm 4) \times 10^{-9}$. The value of $\dot{P}_{35}$ is consistent with zero, within the 1-σ error. Consequently it is no surprise that the quadratic fit yields a larger error. This therefore suggests that the linear fit is the best fit for the ephemeris. Therefore the precession ephemeris

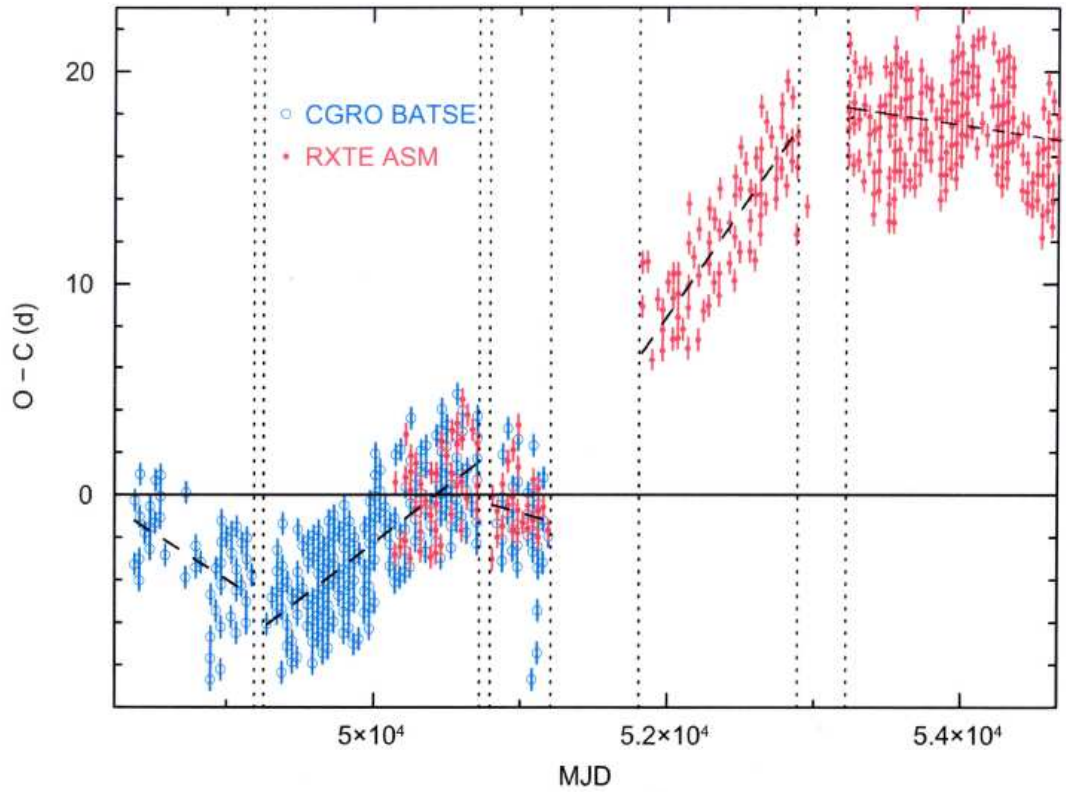

Figure 4.5: A plot of O - C time series of the main-on states in the Her X-1 precession cycle. The linear least-square fits to the O - C diagram are represented by the dashed lines for each epoch. Additional data obtained from SB04.

for the turn-on $T_{\rm on}$ for the current (fifth) epoch is given by

$$T_{\rm on} = \text{MJD } 53190(2) + 34.76E_{35}, \tag{4.2}$$

where a systematic uncertainty of two days is allowed.

Folding the data over the 35-day precession period and averaging it into 50 phase bins at intervals of 0.02, the count rates were plotted as a function of the precession phase, ϕ_{35} (Figure 4.6). This showed that the main-on turn-on occurs at approximately phase $\phi_{35} = 0.9$ although

in Figure 4.6 the turn-on is set at $\phi_{35} = 0$. SB04 determined the brightest flux attained during the 35-day cycle, by measuring the peak of a Gaussian fit of the folded lightcurve between $\phi_{35} = 0.0$ and $\phi_{35} = 0.4$. But the folded lightcurves shown in Figure 4.6 reveal that the 35-day cycles do not show symmetric shapes between $\phi_{35} = 0.0$ and $\phi_{35} = 0.4$. It is therefore appropriate to integrate the folded lightcurve over time (35-day cycle), i.e $F_{\rm int} = \int F dt$. This defines the Fluence (integrated flux). In this case the lightcurve between $\phi_{35} = 0.0$ and $\phi_{35} = 0.4$, i.e. the main-on, was considered for all the epochs and the values obtained for the integrated flux $F_{\rm int}$ are shown in Table 4.1. For comparison, $F_{\rm int}$ is plotted as a function of precession period in Figure 4.7. As was observed by SB04 there is a positive correlation between the precession period and flux $F_{\rm int}$.

4.4 Discussion

Using long baseline data from CGRO BATSE and RXTE ASM, SB04 determined the precession periods of Her X-1 for the first four epochs before the 2003 - 2004 ALS and found that each ALS was accompanied by a "simultaneous" change in precession period. A new precession period and flux have been obtained for epoch 5 (see Table 4.1), in agreement with the predictions of SB04. From the values of P_{35} and $F_{\rm int}$ shown in Table 4.1, it is clear that $P_{35} \propto F_{\rm int}$, which is a confirmation of the theoretical prediction of Wijers & Pringle (1999), that were based upon models of irradiation and feedback of accretion disc, $P_{35} \propto 1/L_{\rm disc}$, but only if $L_* \propto 1/L_{\rm disc}$ where $L_{\rm disc}$ and L_* represent the luminosity of the disc and neutron star respectively. This is easily attainable when the disc surface area incident to the X-ray is a function of the warp, and the warp increases with flux of the neutron star. From Figure 4.6 it is observed that the maximum flux during the short-on state is $\sim 15 - 20\%$ of the maximum main-on flux.

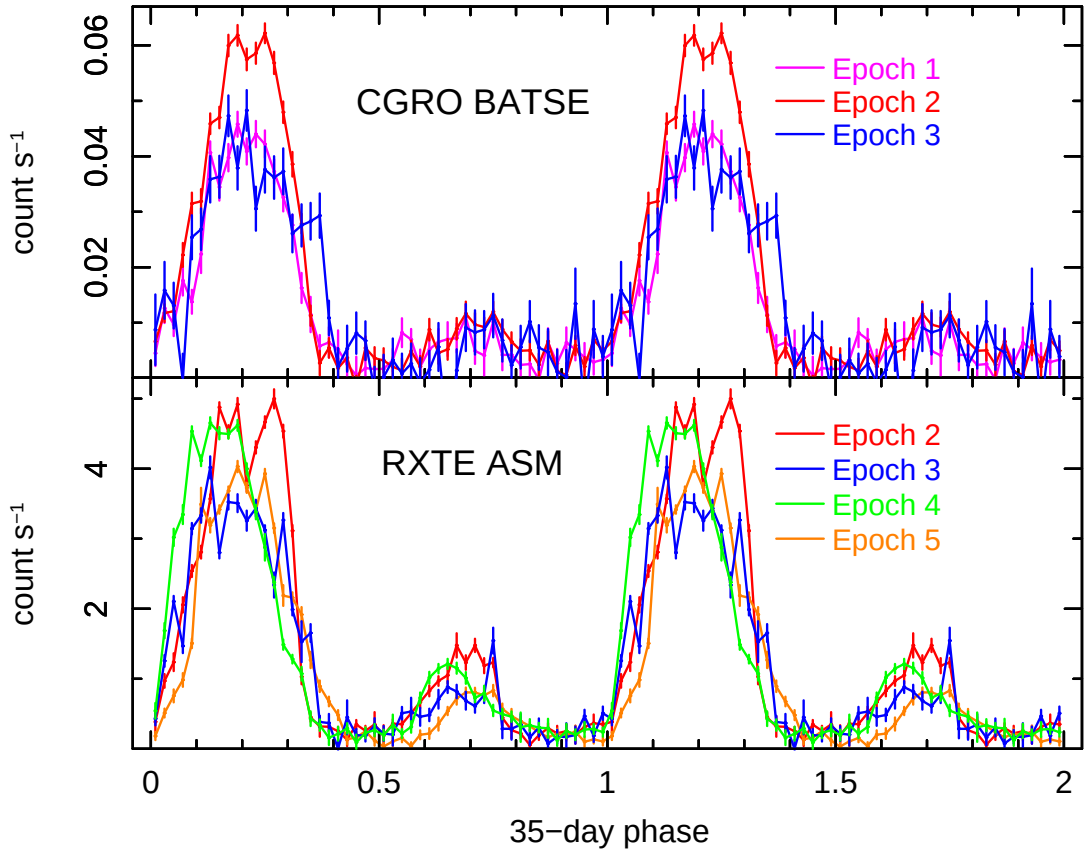

Figure 4.6: The 24 hour averages folded over the 35-day cycle using the appropriate 35-day ephemeris. Additional data obtained from SB04.

The mechanism behind the change in precession period and flux after the ALS is still a matter of debate. As mentioned above, the ALS probably results from an increase in the vertical extent of the disc or increase in the disc warp. Optical observations during the ALS indicate that the irradiation of the companion star (Delgado, Schmidt & Thomas, 1983; Margon et al., 1999) by X-ray flux from the central accreting neutron star has remained constant, indicating that the X-ray emission from the neutron star is not changed dramatically during the ALS. Still et al. (2001b) showed from spectral fits and lightcurve modelling of RXTE PCA pointings that during the ALS the X-ray output consists of X-ray reflections from the companion star. This may

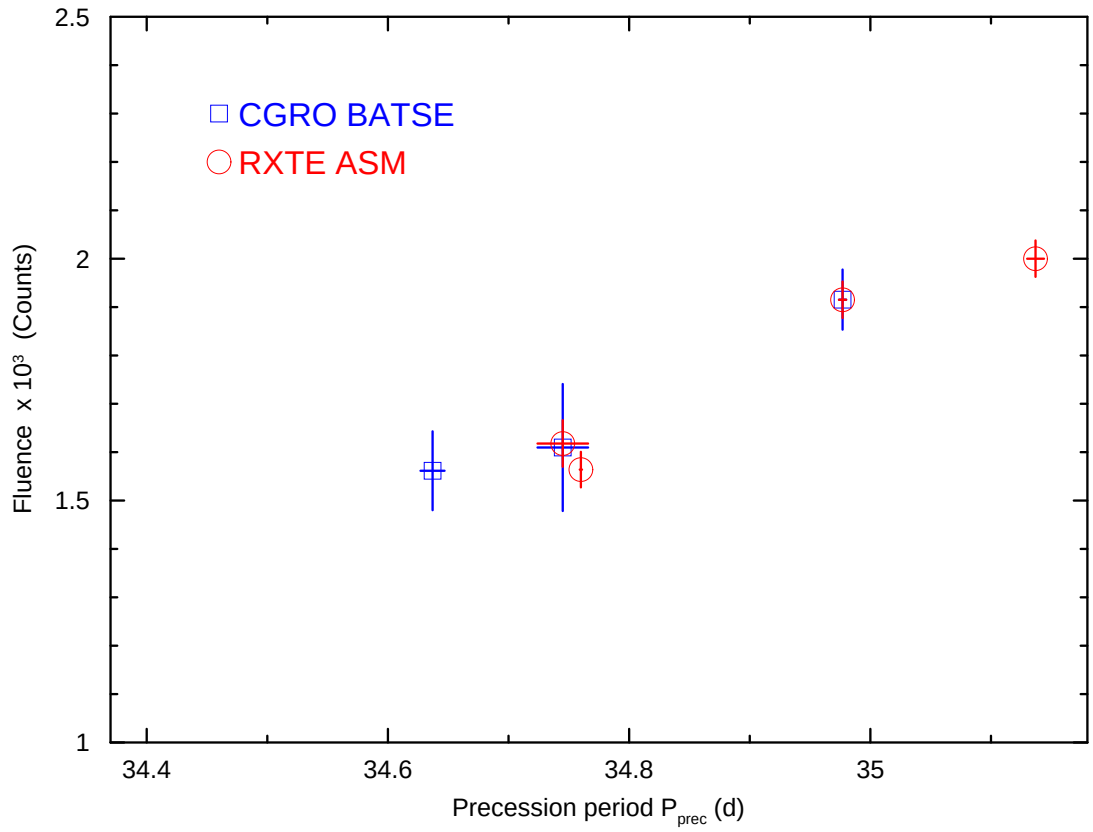

Figure 4.7: The Fluence (integrated flux) between $\phi_{35} = 0.0$ and $\phi_{35} = 0.4$ as a function of precession period. The CGRO BATSE flux has been scaled to fit the RXTE flux. Additional data obtained from SB04.

imply that the ALS results from the obscuration of the neutron star as a result of an increase in the disc wrap or vertical extent.

As mentioned earlier each ALS has been characterised by a period of enhanced spin-down (see Figure 4.8 for the spin history of Her X-1), that was interpreted in terms of increasing torque leading to an acceleration of the rotation of the inner disc. This may imply that in a constant neutron star magnetic field, the magnetospheric radius expands. The spin-down and expansion of the magnetospheric radius possibly results in magnetic shearing outside the corotation ra-

Table 4.1: Precession period P_{35}, derivative $\dot{P}_{35}$, and Fluence for five epochs of Her X-1 precession cycle.

	CYCLE		MJD		P_{35}	$\dot{P}_{35}$	Fluence ($F_{\rm int}$)
Epoch	Start	Stop	Start	Stop	(days)	(days day^{-1})	$\times 10^3$ Counts
1...	-75	-52	48,377	49,213	34.637 ± 0.010	$-(3 \pm 1) \times 10^{-7}$	0.018 ± 0.001
2...	-49	-8	49,282	50,708	34.977 ± 0.003	$(3 \pm 2) \times 10^{-8}$	0.022 ± 0.001^a, 1.91 ± 0.04^b
3...	-5	+6	50,813	51,195	34.745 ± 0.021	$-(7 \pm 7) \times 10^{-10}$	0.019 ± 0.002^a, 1.62 ± 0.05^b
4 ..	+26	+54	51,892	52,866	35.137 ± 0.007	1×10^{-7}	2.00 ± 0.04
5...	+64	+83	53,220	-	34.760 ± 0.001	$(6 \pm 4) \times 10^{-9}$	1.56 ± 0.04

Note: Cycle number is relative to MJD 50,986.7

[a] CGRO BATSE

[b] RXTE ASM

dius, resulting in enhanced MHD energy being fed to the disc. This may result in disc heating, leading to an increase in disc scale height and opacity. The spin-down in this case would imply a decrease in mass accretion rate (Ghosh & Lamb, 1979a,b). Decrease in mass accretion rate would in turn imply reduced mass transfer rate from the companion star (or reduced disc viscosity). Considering that an increase in disc warp which results in the ALS, as shown in Chapter 6, is caused by increased radiation pressure (e.g. Pringle, 1996, 1997), this would have implied increased X-ray flux, heating the accretion disc, as a result of increased mass accretion rate. This is in contradiction with the Ghosh and Lamb (1979) accretion disc torque theory. This probably suggests that there could be different mechanisms responsible for the anomalous low states in Her X-1. Radiation pressure is investigated in Chapter 6 and there is need for further investigation, in future, of the accretion disc torque as another probable mechanism.

As mentioned above, increased X-ray flux from the neutron star would imply increased ac-

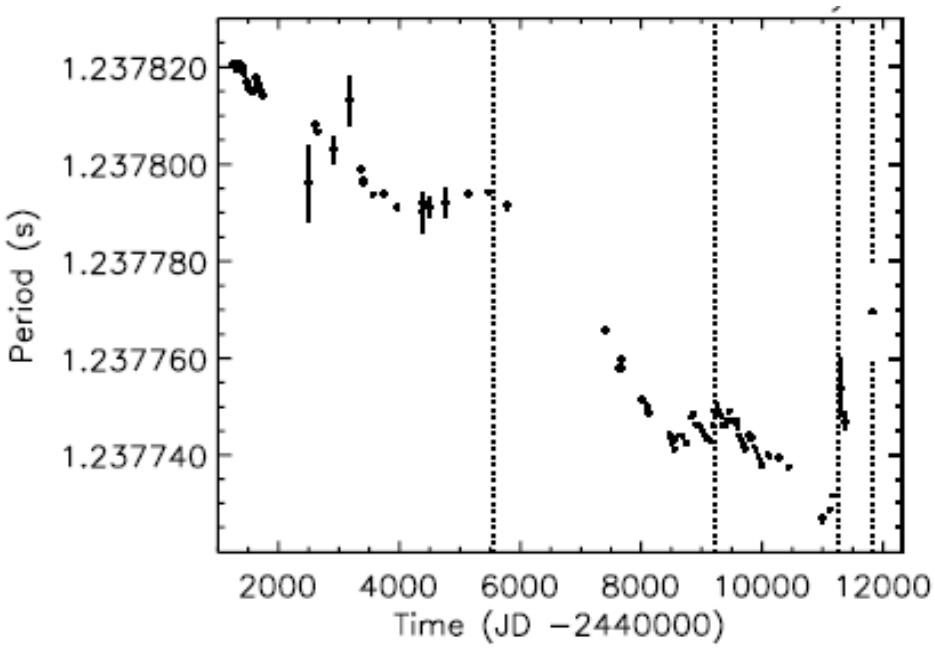

Figure 4.8: The spin history of Her X-1. The dashed vertical lines indicate the start and stop times of previous ALS of Her X-1. (*Adopted from Oosterbroek et al., 2001*).

cretion rate. However, there seems to be no indication that the mass accretion rate changes substantially during the ALS since optical observations detect a constant effect of continued strong X-ray heating of the companion star (Delgado et al., 1983; Mironov et al., 1986; Margon et al., 1999). This would imply that the spin-down torque during the ALS originates from approximately the same amount of mass transfer (Oosterbroek et al., 2001; Coburn et al., 2000) as during the high states. But according to the Ghosh & Lamb (1979) standard accretion torque theory, reduction in mass accretion rate (which results in reduced X-ray luminosity) results in a reduced gas (or ram) pressure in the accretion disc. This would in turn result in an increase in the magnetospheric radius and a change in the accretion torque causing the neutron star to spin-down. It is also expected that a reduction in mass accretion rate would result in a reduction in the inclination of the accretion disc (Coburn et al., 2000), either by changing the torque

of the accretion stream on the disc (Shakura et al., 1999) or by changing the radiative torque resulting from X-ray heating the accretion disc. Li & Wickramasinghe (1998) also proposed that the variations in the spin-down rate can be caused by changes in the structure of the outer magnetosphere of the neutron star and these changes may be accompanied by changes in the disc structure which produces the ALS.

From the above discussions the possible mechanism responsible for the ALS and at the same time the change in precession period after each ALS is still not clear and needs to be investigated further. However it is probable that the ALS and change in the precession period after each ALS could be interpreted as a change in the disc shape or vertical extent. In Chapter 6 more insight into the nature of the ALS and possibly the explanation for the change in the precession period will be given from the study of the spectral evolution of the ALS using RXTE and XMM-Newton observations. In the next chapter the focus will be on the optical and X-ray lightcurves of Her X-1.

Chapter 5

Orbital Lightcurve of Hercules X-1

5.1 Introduction

The X-ray binary pulsar Her X-1 shows a periodic intensity variation on a period of ~ 1.7 days, i.e. the binary period of the pulsar and the companion star. In this chapter, the optical and X-ray orbital lightcurves of Her X-1 are discussed. The optical and X-ray lightcurves of Her X-1 are constructed for different phases of the 35-day precession cycle. This is used to investigate the following:

(i) The shape of the accretion disc, from variations in the lightcurve profile over the 35-day precession cycle.

(ii) The source of the X-ray emission during the anomalous low state, by comparing the X-ray and optical lightcurves taken during the anomalous low state.

(iii) The change in the shape of the accretion disc, from the ratio of the normal high state flux to the anomalous low state flux.

5.2 Instruments and Observations

The data presented in this chapter were collected using the Proportional Counter Array on board RXTE and the superWASP-North observatory. In the following two sections a brief overview of the instruments used during the observations will be presented. The discussions on the proportional counter array are based on the RXTE technical appendix available at $http://rxte.gsfc.nasa.gov/docs/xte/appendix\_f.html$, while that on superWASP follows from $http://www.superwasp.org$, unless otherwise stated.

5.2.1 The Proportional Counter Array on board RXTE

The Proportional Counter Array (PCA) consists of five identical Xenon multi-anode Proportional Counter Units (PCUs), each with a field of view of 1° FWHM. Each PCU consists of a Propane Volume (PV) and a main Xenon chamber. While the Xenon chamber is used as the main detection volume for the source photons, the propane volume is used as a veto shield to reduce background. The Xenon chamber has four layers, out of which the upper three layers (L1, L2, L3/R1, R2, R3) (see Figure 5.1) are used for X-ray photon detection. The fourth Xenon layer (veto layer) is marked VX, in Figure 5.1. The top layer (first layer) is the most sensitive and produces the best signal to noise ratio. For faint sources with soft spectra, the detection probability is highest in the top layer and the contribution from the remaining layers is not significant compared to the overall detected count rate.

The PCA has a nominal energy range from 2 keV to 60 keV, temporal resolution of 1μs and total effective area of 6000 cm^2. The PCUs have shown unexpected breakdowns probably caused by sparks within the xenon layers. This has resulted in some PCUs being switched off, i.e. allowing them to rest, during science observations.

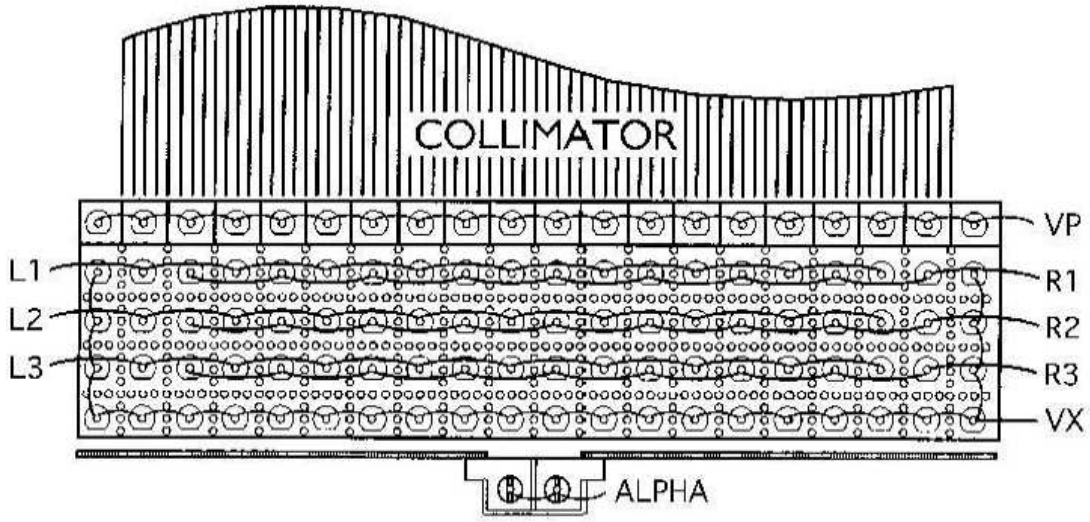

Figure 5.1: Schematic picture of the cross section of the PCA showing the propane volume, the Xenon chamber with four layers and the collimator. (*Adopted from Kuster, 2004 and references therein).*

Another challenge for X-ray satellites, which renders scientific observations with proportional counters useless, are the radiation and particle belts called Van Allen belts (van Allen Mcllwine & Ludwing, 1959). RXTE is in a low orbit, far below the lowest Van Allen belt found at a height of 1000 km and therefore cannot affect the operation of RXTE PCA. However, in regions where the configuration of the Earth's magnetic field is slightly different, e.g. off the East coast of Brazil (Kreykenbohm, 2004 and references therein), high energy particles captured inside the Van Allen belt can enter this region resulting in a very intense particle background called the South Atlantic Anomaly (SAA). The SAA is responsible for very high count rates in detectors like the PCU that can cause damage. During science observations, all the PCUs are therefore switched off during SAA passage to prevent them from being damaged.

For both the PCA and ASM, the Experiment Data System (EDS) is used for the on board processing of raw data. For the PCA, the EDS provides six data modes operated by six independent analysers, while two additional analysers are used for handling the ASM data. For the case of the PCA the final observational data is provided in six basic modes containing data from the same PCU processed by the EDS in the different modes.

Her X-1 was observed by RXTE from February 10, 2004 to February 11, 2004 and from February 22, 2004 to February 23, 2004. In this thesis data from the PCA is analysed. Tables 5.1 and 5.2 summarise the RXTE pointings during these periods of observation.

5.2.2 SuperWASP

The Wide Angle Search for Planets (WASP), also called superWASP, is a United Kingdom (UK) collaborative project aimed at searching for extra-solar planets. It also aims at discovering transient and moving optical objects and potentially dangerous near-Earth objects. The superWASP consists of two observatories which are robotically operated: the superWASP-North located at the observatorio del Roque de los Muchachos on the La Palma, Canary Islands and the superWASP-South located at the site of the South African Astronomical Observatory, just outside the town of Sutherland. The two observatories, i.e. superWASP-North and superWASP-South, are identical, each consisting of 8 wide-angle CCD cameras that simultaneously scan the night sky (see Figure 5.2).

SuperWASP-North was operated between 2004 and 2007 with cameras each having a 200 mm f/1.8 canon lens with Andor CCD array (Cameron et al., 2006), and a field of view of $7.8^{\circ} \times 7.8^{\circ}$ (Norton et al., 2007) with an angular scale of 13.7 arc sec per pixle. This results in a total field of view of ~ 500 square degrees per observation (Wilson et al., 2006). The system has the

Table 5.1: Summary of the RXTE pointings during the observation period February 10 to 11, 2004.

Pointing	Start Time (UT)	Stop Time (UT)	Mid orbital phase	PCUs on
1	2004-02-10T06:47:10	2004-02-10T07:22:08	0.213	4
2	2004-02-10T10:00:32	2004-02-10T10:31:08	0.291	4
3	2004-02-10T12:42:46	2004-02-10T13:40:08	0.357	4
4	2004-02-10T14:16:46	2004-02-10T15:15:08	0.402	4
5	2004-02-10T17:26:24	2004-02-10T18:24:08	0.479	4
6	2004-02-10T22:12:26	2004-02-10T23:07:08	0.596	2
7	2004-02-11T01:29:36	2004-02 11T03:51:08	0.694	2
8	2004-02-11T04:45:44	2004-02-11T05:26:08	0.753	3
9	2004-02-11T08:01:40	2004-02-11T08:34:08	0.832	4
10	2004-02-11T10:46:24	2004-02-11T11:44:08	0.904	2
11	2004-02-11T13:55:28	2004-02-11T14:53:08	0.981	3
12	2004-02-11T17:04:24	2004-02-11T18:02:08	0.059	3
13	2004-02-11T20:13:24	2004-02-11T21:11:08	0.130	4
14	2004-02-11T23:27:52	2004-02-12T00:10:08	0.210	2

capability to deliver photometry with accuracy better than 1% for object with V $\sim 7.0 - 11.5$, and is capable of monitoring the sky down to ~ 15th magnitude every 40 minutes. Her X-1 has magnitude of ~ 13.8 (Norton et al., 2007b) and therefore can be observed by superWASP. Each CCD consists of 2048×2048 pixels each of 13.5 μm in size (Pollacco et al., 2006). These devices are back illuminated and have a peak quantum efficiency of $> 90\%$. With exposure times of only 30 seconds the device is cooled to a temperature of -50°C at which the dark current is ~ 70 e/pix/h. The telescope follows the automated observing routine with a raster pattern sweeping from 3.5 hours east to 3.5 hours west of the meridian, and returns to a given

Table 5.2: Summary of the RXTE pointings during the observation period February 22 to 23, 2004.

Pointing	Start Time (UT)	Stop Time (UT)	Mid orbital phase	PCUs on
1	2004-02-22T06:44:32	2004-02-22T07:41:08	0.275	4
2	2004-02-22T09:53:24	2004-02-22T10:41:08	0.352	3
3	2004-02-22T13:02:24	2004-02-22T13:44:08	0.427	4
4	2004-02-22T16:13:52	2004-02-22T16:58:08	0.506	3
5	2004-02-22T19:20:38	2004-02-22T20:14:08	0.583	4
6	2004-02-22T22:29:20	2004-02-22T23:27:08	0.661	3
7	2004-02-23T01:45:20	2004-02-23T05:45:08	0.778	3
8	2004-02-23T07:56:52	2004-02-23T08:54:08	0.893	3
9	2004-02-23T11:05:20	2004-02-23T12:03:08	0.970	2
10	2004-02-23T14:15:00	2004-02-23T14:58:08	0.045	3
11	2004-02-23T17:23:48	2004-02-23T18:12:06	0.123	3
12	2004-02-23T22:07:28	2004-02-23T23:05:06	0.240	2

field every six minutes on average (Cameron et al., 2006). During the first year of operation, the superWASP-N observations were unfiltered and the transmission was effectively defined by the optics, detectors and atmosphere (Pollacco et al., 2006). At present broad band filters are used with a pass band from 400 - 700 nm. The system has the capability to survey the entire visible sky every 40 minutes (Pollacco et al., 2006), although the coverage is not uniform with some region of the sky better sampled than others (Cameron et al., 2006).

A data pipeline has been developed for superWASP to reduce data sets with a high level of automation. For a detailed discussion about the hardware and pipeline data reduction see Pollacco

et al. (2006). The superWASP pipeline data reduction uses the USNO-B1.0 catalog (Monet et al., 2003) as the photometric input catalog. Aperture photometry is then carried at the positions of all stars in the catalog brighter than a given limiting magnitude. In this approach, aperture photometry is performed within circular regions, centred on the source, of radius 2.5, 3.5 and 4.5 pixels. The aperture photometry routine then calculates the flux within this circular region on the predicted positions of the object in the catalog (Kane et al., 2004). The sky background is then calculated from an annulus around the source with inner radius of 13 pixels and outer radius of 17 pixels (Pollacco e al., 2006). A post-pipeline calibration is then performed. This process calibrates and removes four main trends in the photometry, i.e. effects of primary and secondary extinction, instrument colour response and the system zero-point. The reduced data are then stored in the the superWASP archive. The superWASP archive consists of three major classes of data (Pollacco et al., 2006): the bulk processed photometry (which were used in this thesis), the raw images and a WASP catalog which provides very basic information (e.g. co-ordinates of the object) about each object observed by superWASP.

5.3 Data Reduction and Results

5.3.1 The RXTE PCA data

The RXTE PCA data reduction was performed using the standard algorithms within **FTOOLS**. This is briefly discussed in this section. The PCA data configuration used to extract the source lightcurves presented here is the GoodXenon which records all good events detected in the xenon chamber with timing accuracy of 1 μs. Photons detected in all the xenon layers were used. Before extracting the lightcurves, the raw data was filtered for background contamination and data quality. This was done by defining the Good Time Interval (GTI), which gives infor-

Figure 5.2: A picture of the superWASP observatory showing the eight cameras (*Adopted from http://www.superwasp.org).*

mation about the status of the satellite and its instruments during the observation, i.e. the GTI is used to indicate periods of good data.

The GTI selection criteria is based on the detector background flux, source elevation and the times of SAA passage. All this information is found in the filter files which are supplied together with the data. The detector background contamination is the housekeeping value called the electron ratio. The electron ratio gives an indication of the amount of internal detector background flux caused by charged particles. Another source of background is the SAA passage which increases the background. The Earth's atmosphere absorbs X-rays and this has to be

taken into account within the GTI. The GTI was therefore constructed to filter the GoodXenon data for each visit as follows: electron ratio < 0.1, Earth's limb $< 10^{\circ}$ and off axis pointing $< 0.02^{\circ}$. The number of PCUs which were active during the observation varied from 2 to 4 (see Tables 5.1 and 5.2) and this was also indicated in the GTI file.

The background lightcurves were extracted from the PCA standard2 data mode using the same GTI as for the source lightcurves. For each visit the background models were subtracted and the data scaled by the number of active PCU's. The background subtracted lightcurves from all the visits were then summed-up using a bin size of 250 s. The resulting lightcurves are shown in Figure 5.3. This data was collected during the anomalous low state of Her X-1.

5.3.2 SuperWASP Data

Her X-1 was observed by superWASP-North several times per night during its operation from May 2004 to September 2004 and from April 2006 to August 2007. These periods covered both the most recent (2003 - 2004) anomalous low state and the current normal high state (fifth epoch) of Her X-1. The processed photometry data for Her X-1 from superWASP-North was used to construct the optical lightcurves of Her X-1.

To construct the orbital lightcurves of Her X-1 during the anomalous low state and the normal high state, the data were first folded over the respective precession periods, i.e. using the precession ephemeris for the turn-on for the fourth epoch (SB04)

$$T_{\rm on} = \text{MJD } 51821 + 35.10E_{35} \tag{5.1}$$

to fold the data during the anomalous low state, while for the high state (fifth epoch) the precession ephemeris obtained in Chapter 4 (Equation 4.2) was used. The orbital cycles were then

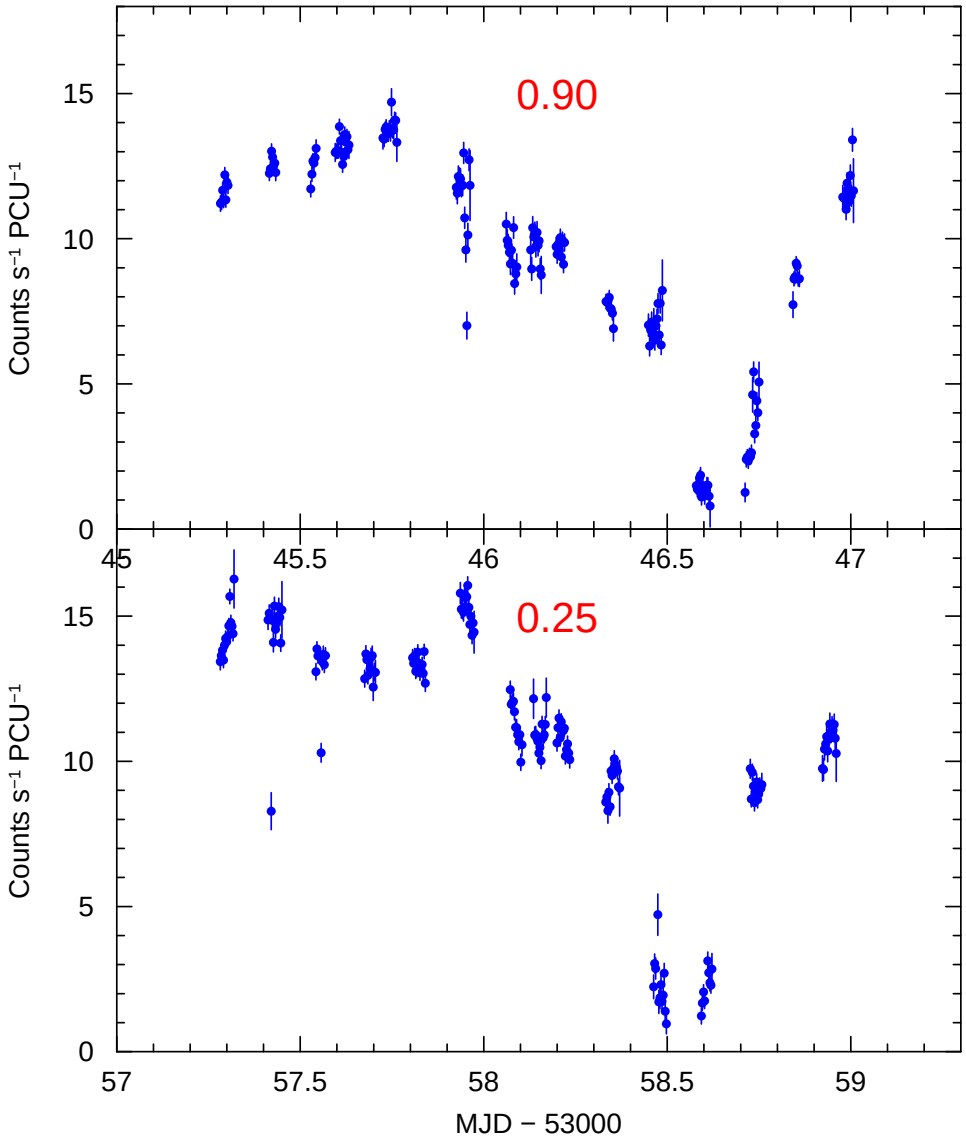

Figure 5.3: The Anomalous Low State X-ray lightcurve of Hercules X-1. The precession (mid-precession) phases are indicated in each panel.

folded after selecting the data based on the precessional phase bins. The orbital ephemeris used to fold the date is given by (Still et al., 2001a) (considering only the linear terms)

$$T_{\rm mid-ecl} = \text{MJD } 51004.729581 + 1.700167504E_{1.7}, \tag{5.2}$$

where $T_{\mathrm{mid-ecl}}$ represents the times of mid-eclipse and $E_{1.7}$ is the orbital cycle number. The data for each precessional phase bin were then averaged into 50 bins and plotted as a function of orbital phase. Figures 5.4 and 5.5 show the resulting lightcurves during the anomalous low state and the normal high state respectively.

The data as presented in Figures 5.4 and 5.5 do not clearly show the precessionally dependent variations in the orbital lightcurves. To show any variations, the following approach was used:

(i) The mean orbital lightcurves (Figure 5.6) for both the anomalous low state (SWASP ALS) and the normal high state (SWASP NHS) were constructed by folding the data for each state over the orbital cycle using the orbital ephemeris given in Equation 5.2.

(ii) The data for the individual precessional phase bins (Figure 5.4 and 5.5) were then subtracted from the respective mean orbital lightcurves (Figure 5.6).

(iii) The differences were then plotted as a function of orbital phase. This is shown in Figure 5.7 for both the anomalous low state (left) and the normal high state (NHS) (right).

Gerend and Boynton (1976) (hereafter GB76) accumulated a considerable amount of optical photometric data on Her X-1. These data were scanned and the mean orbital lightcurve constructed as described above. The resulting lightcurve is shown in Figure 5.8. This is plotted together with the superWASP anomalous low state mean orbital lightcurve (top panel) for comparison. In this case it is assumed that all the GB76 data covered the normal high state of Her X-1. The data for the individual precessional phase bins were then subtracted from the mean orbital lightcurves, as described above, and the differences plotted as a function of orbital phase. This was plotted along side the superWASP anomalous low state data for comparison (Figure 5.9).

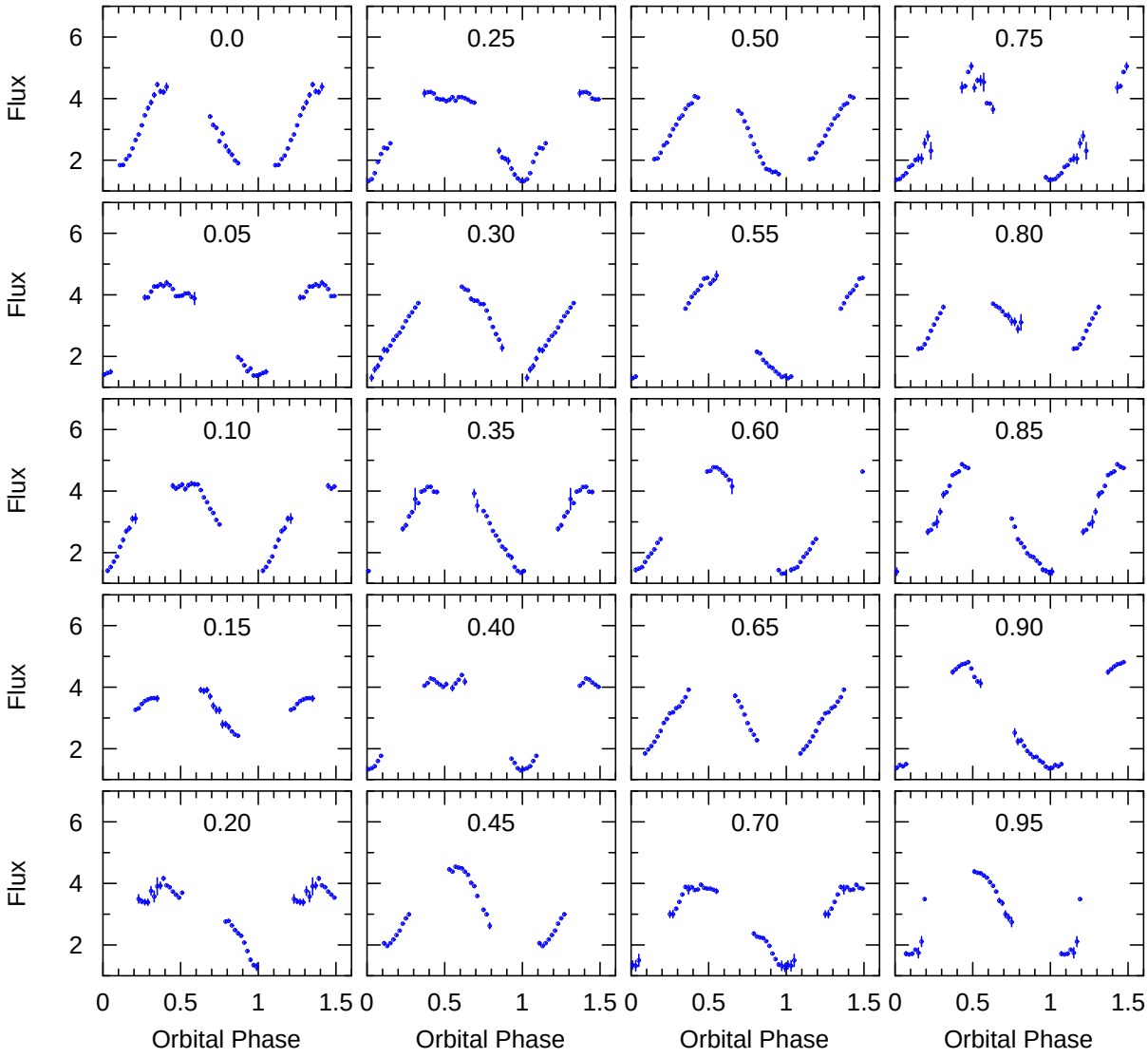

Figure 5.4: The Anomalous Low State optical lightcurves of Her X-1. The numbers in each panel indicate the precession (mid-precession) phase. The statistical errors on the data are very small that they may not be seen from the plots. The orbital cycle is plotted one and half times to show the primary eclipse.

5.3.3 Comparison of the ALS Optical and X-ray Lightcurves

The X-ray lightcurves (RXTE PCA data) were also folded over the orbital cycle following the same procedure described for the superWASP data above. The X-ray and optical lightcurves,

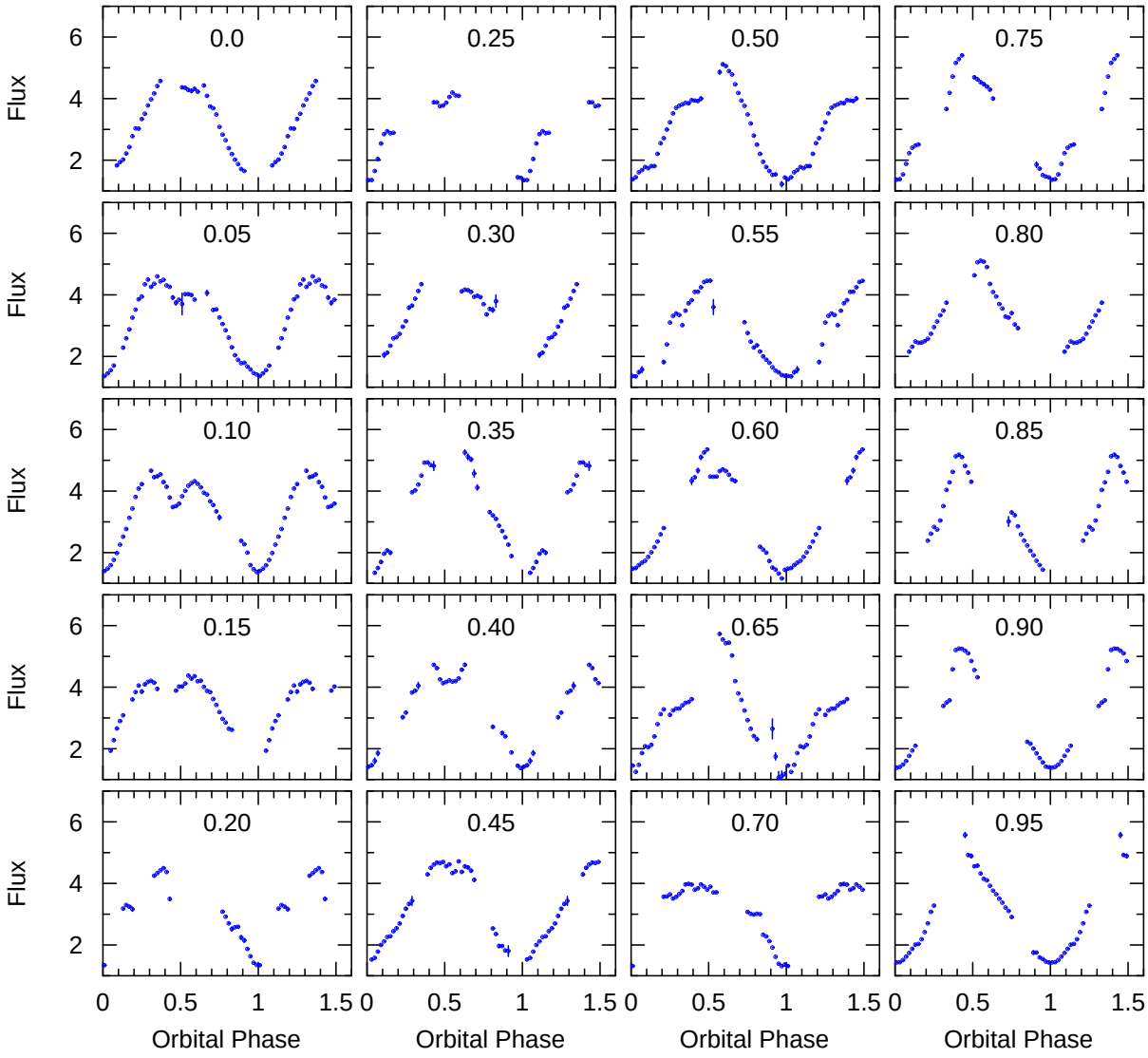

Figure 5.5: The normal high state optical lightcurves of Her X-1. The precession (mid-precession) phases are indicated in each panel. The statistical errors on the data are very small that they may not be seen from the plots. The orbital cycle is plotted one and half times to show the primary eclipse.

both during the ALS and covering the same precession phases, were then plotted as shown in Figure 5.10 and 5.11 for comparison. Since both data cover the ALS, this comparison can be

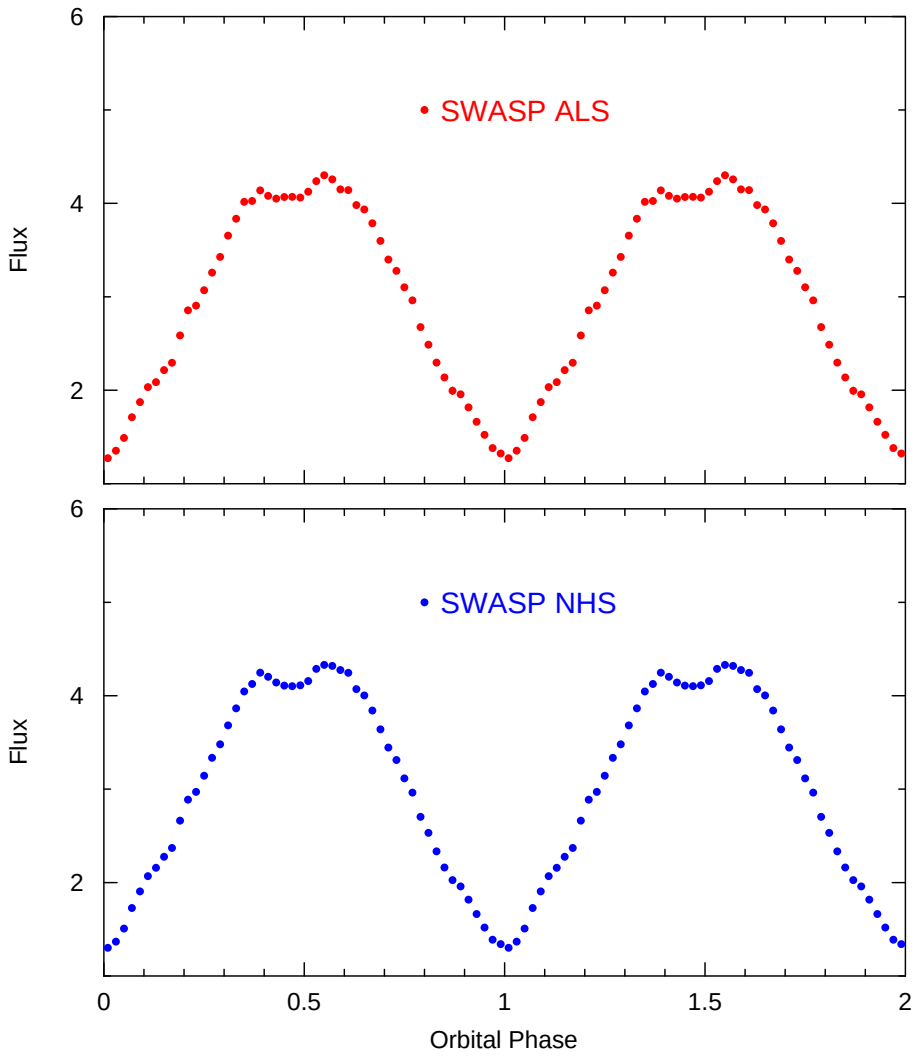

Figure 5.6: The mean orbital lightcurves of Her X-1 during the Anomalous low state (upper panel) and normal high state (lower panel). The statistical errors on the data are very small that they may not be seen from the plots. The orbital cycle is plotted twice for clarity.

used to trace the X-ray source during the ALS.

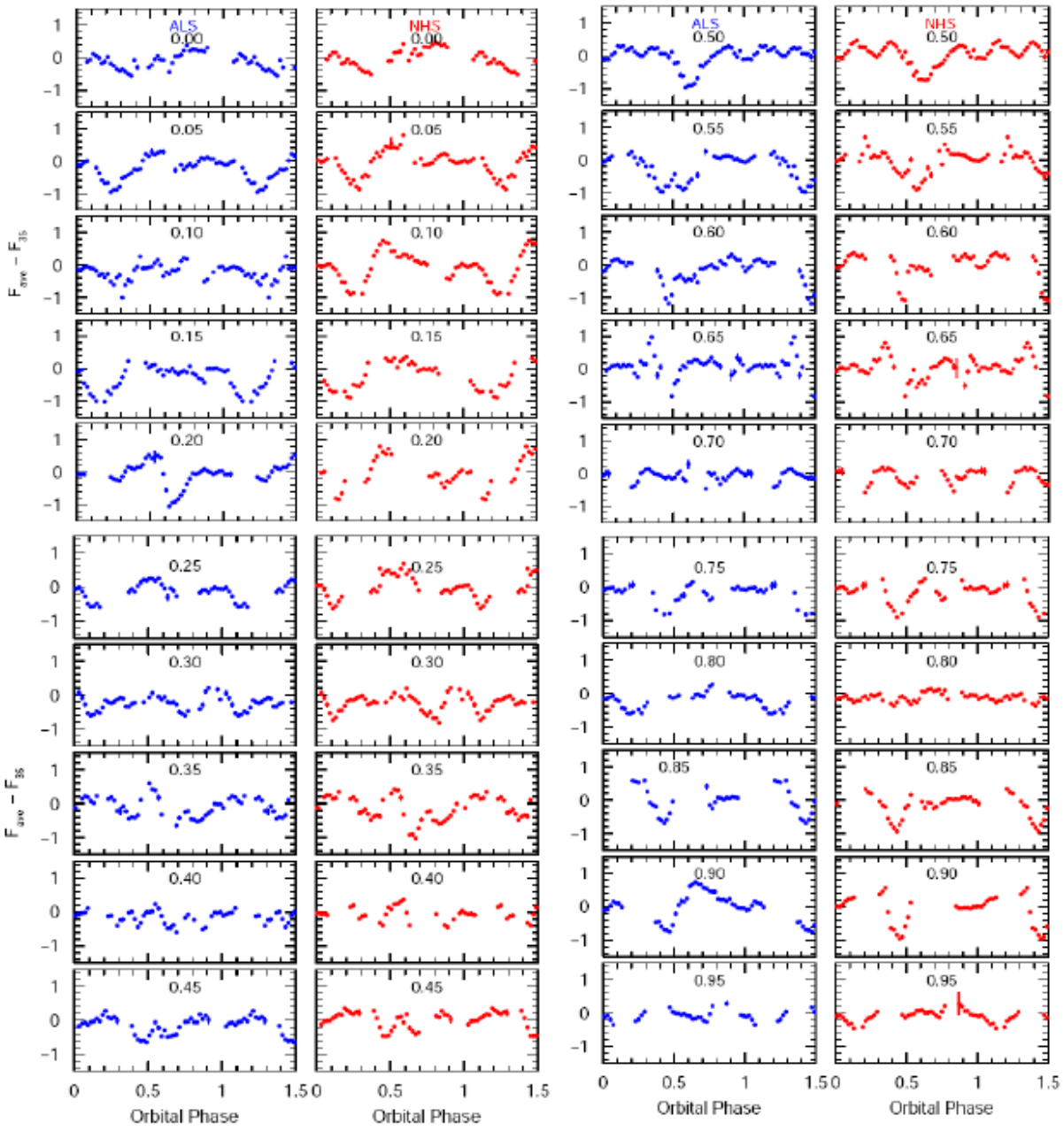

Figure 5.7: The difference plots ($F_{\rm ave} - F_{35}$, where $F_{\rm ave}$ is the flux of the mean orbital lightcurve and F_{35} is the flux of the individual precessional phase bins) for both the anomalous low state (blue colour) and normal high state (red colour). The precession phase is indicated in each panel.

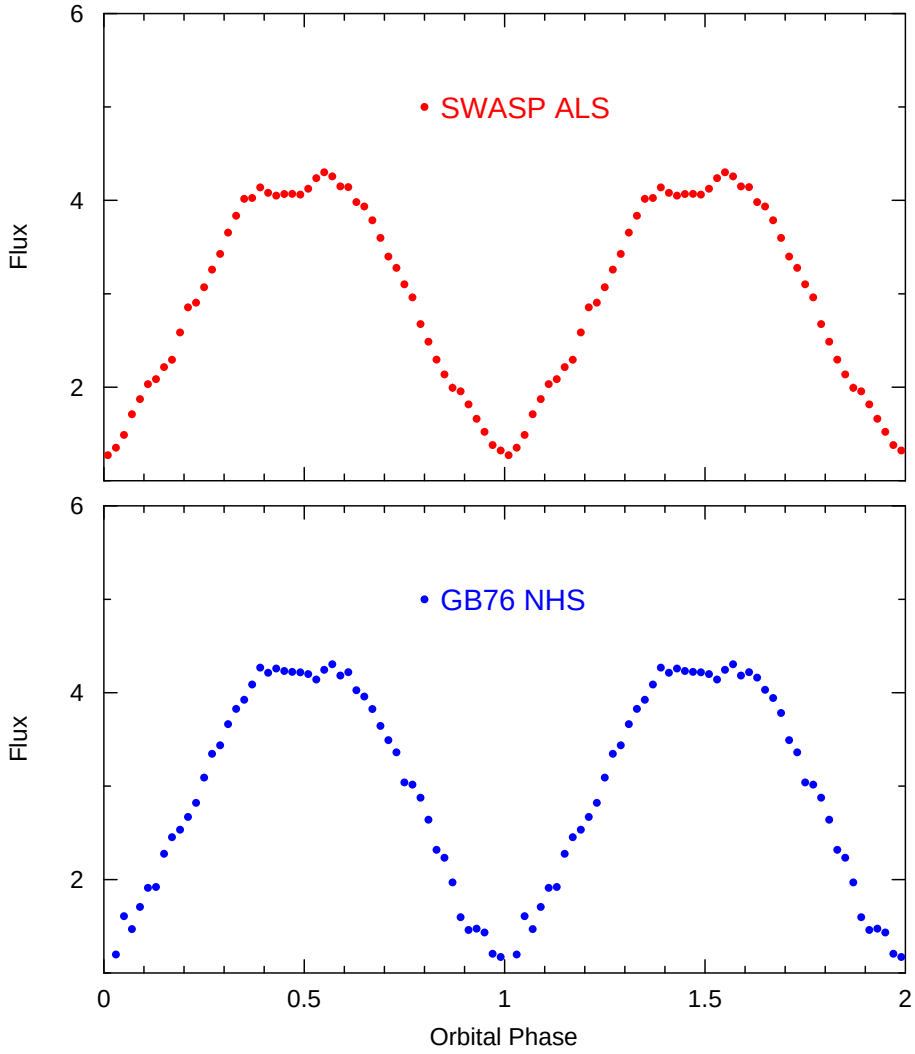

Figure 5.8: The mean orbital lightcurves of Her X-1 during the Anomalous low state (SuperWASP) (upper panel) and normal high state (GB76) (lower panel). The statistical errors on the data are very small that they may not be seen from the plots. The orbital cycle is plotted twice for clarity.

5.3.4 Comparison of the ALS and Normal High State Lightcurves

To show any evidence for systematic changes in the disc morphology over the 35-day cycle, the ratio of the flux between the the respective normal high state and anomalous low state

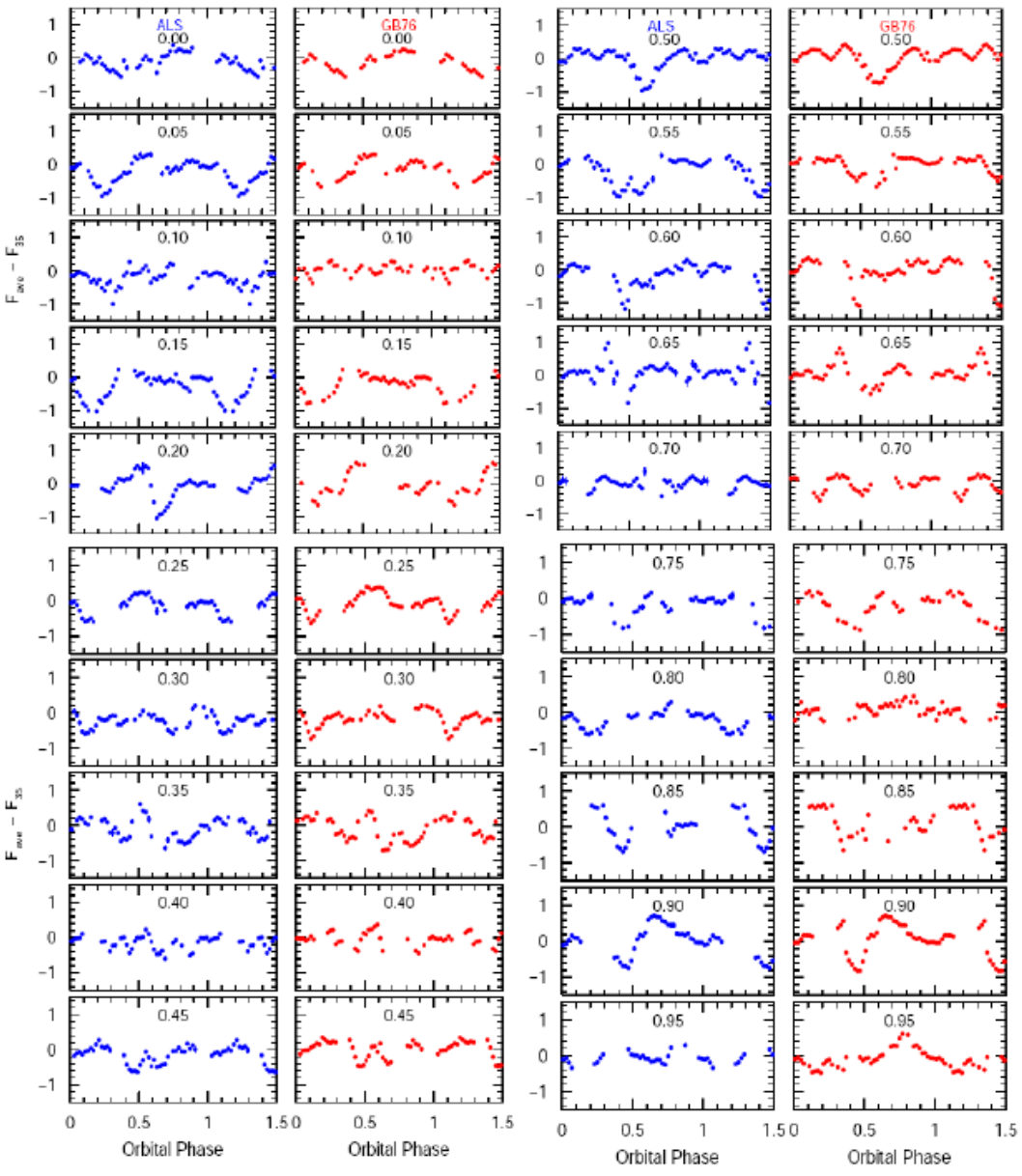

Figure 5.9: The difference plots ($F_{\rm ave} - F_{35}$) for both the anomalous low state (superWASP) (blue colour) and normal high state (GB76) (red colour). The precession phase is indicated in each panel.

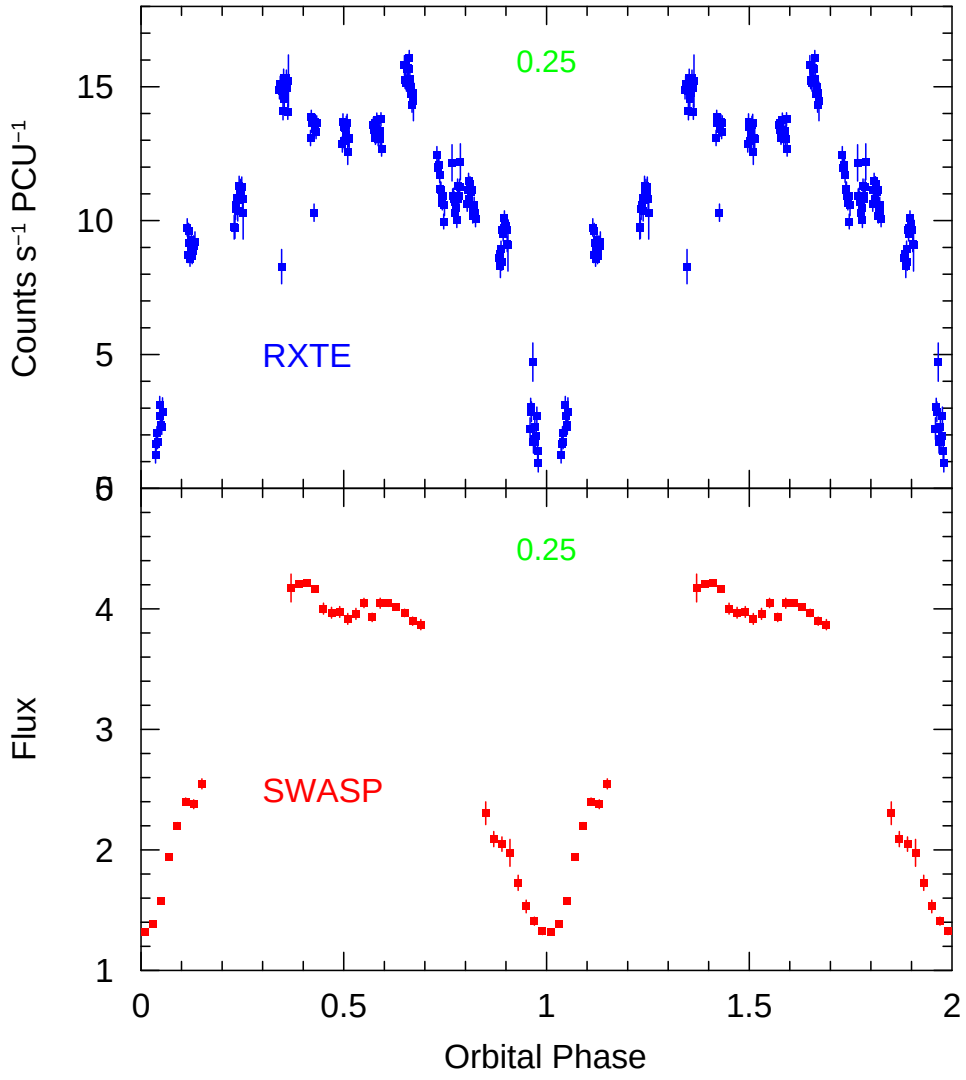

Figure 5.10: The Anomalous low state X-ray (top panel) and optical (bottom panel) lightcurves of Her X-1 covering precession phase $\phi_{35} = 0.25$. The orbital cycle is plotted twice for clarity.

precessional phase bins were calculated, i.e, $F_{\rm NHS}/F_{\rm ALS}$ where $F_{\rm NHS}$ and $F_{\rm ALS}$ represent the normal high state flux and anomalous low state flux respectively. These were plotted against the orbital phase as shown in Figure 5.12 .

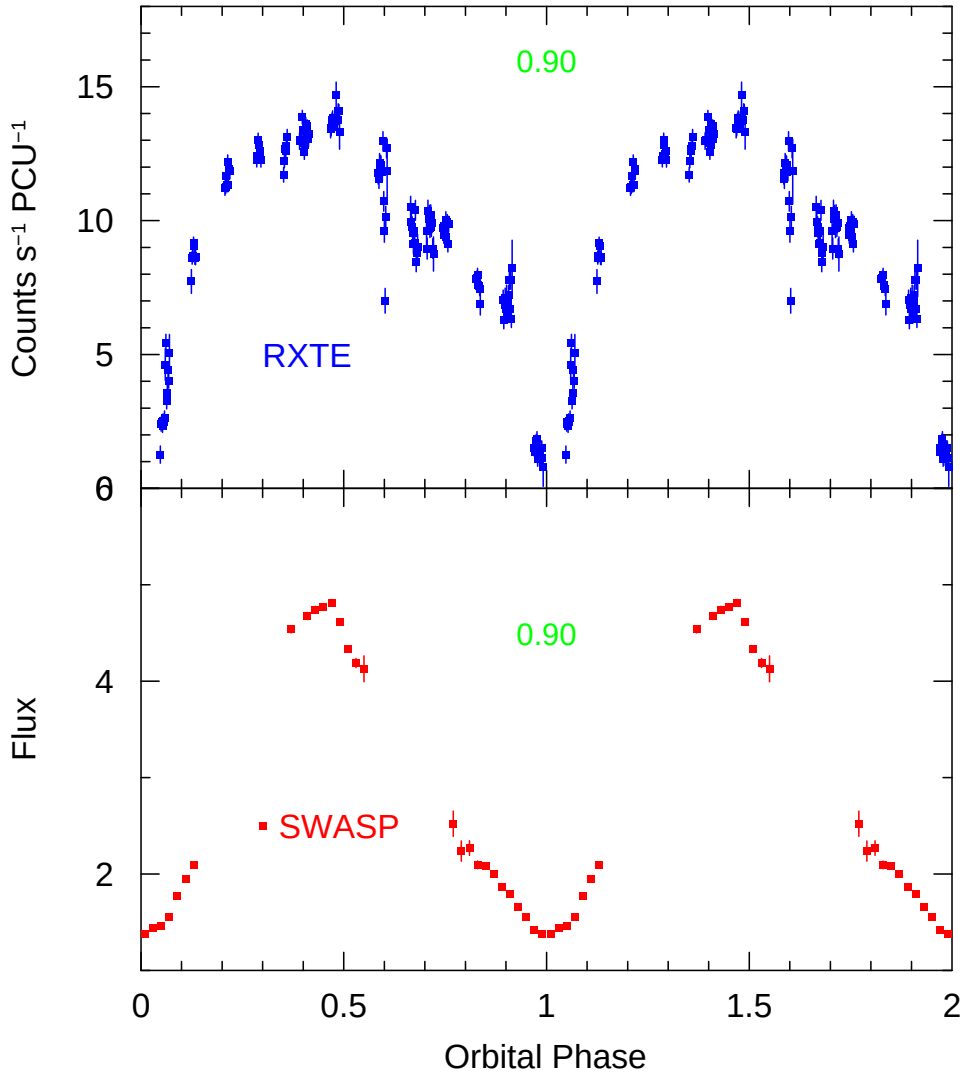

Figure 5.11: The Anomalous low state X-ray (top panel) and optical (bottom panel) lightcurves of Her X-1 covering precession phase $\phi_{35} = 0.90$. The orbital cycle is plotted twice for clarity.

5.4 Discussion

Her X-1 was observed between 2004 and 2007, covering both the ALS and the normal high state, with superWASP-North in the optical wavelength and in 2004 during its ALS with RXTE

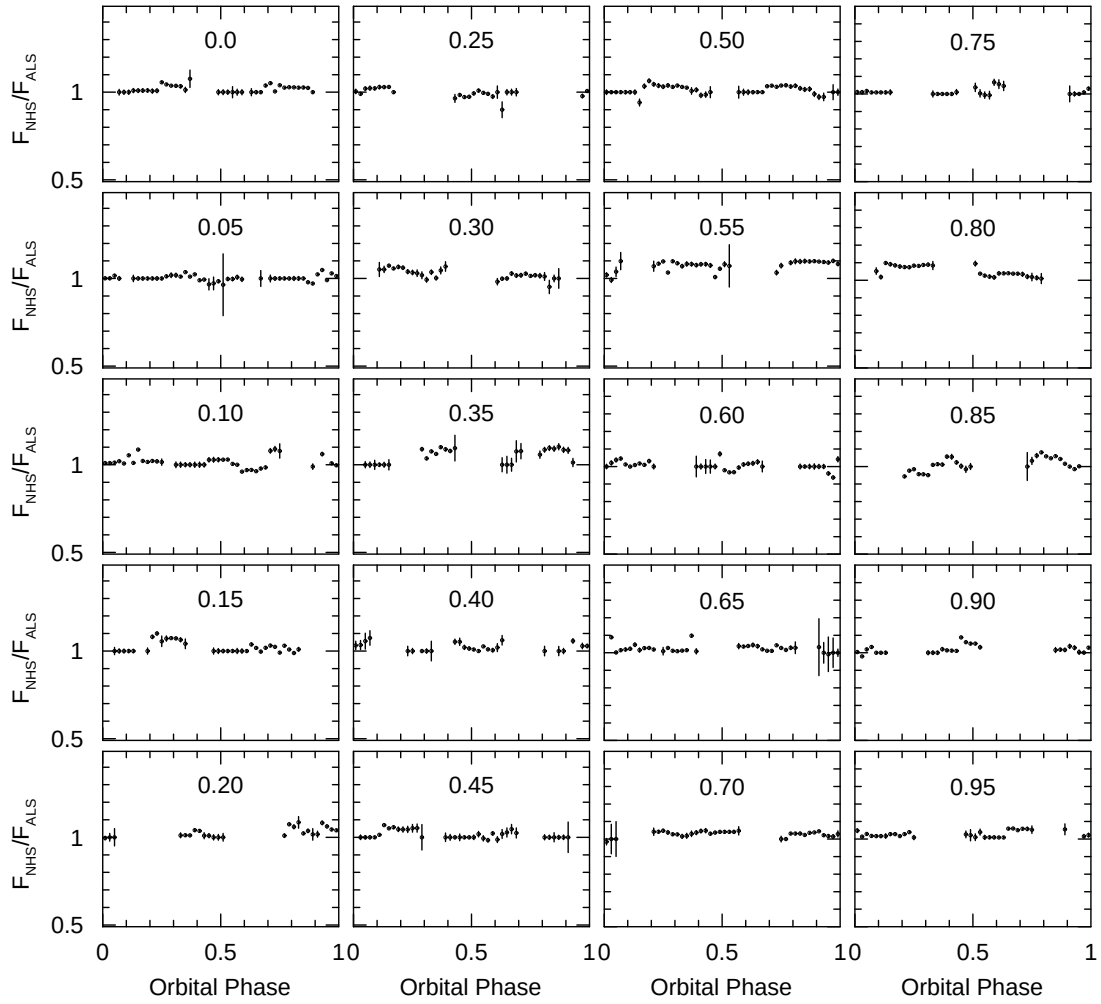

Figure 5.12: The ratio of the normal high state flux to the ALS flux of Her X-1. The precession phases are indicated in each panel.

in the X-ray wavelength. The optical flux of Her X-1 is dominated by emission from the companion star resulting from reprocessed X-rays from the irradiated face of the companion star, i.e. the X-ray flux from the compact neutron star is reprocessed to the optical wavelengths (Boynton et al., 1973; Howarth & Wilson, 1983; Still et al., 2001b). Some contribution to the optical flux originate from blackbody emission from the X-ray heated accretion disc (Cheng, Vrtilek & Raymond, 1995).

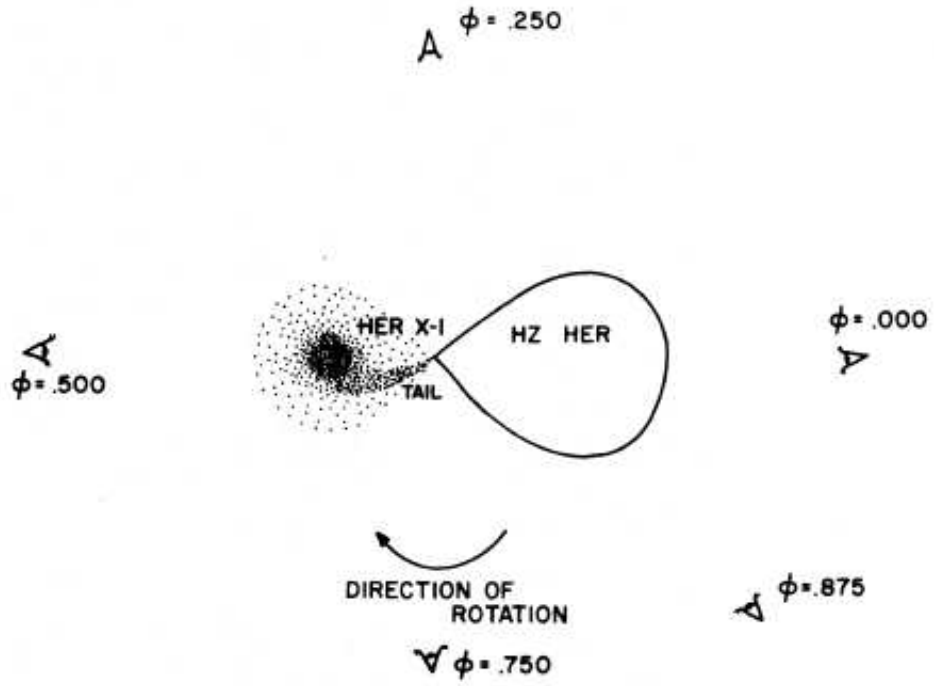

Figure 5.13: Schematic picture of Her X-1 showing the different viewing angles of the system (*Adopted from Grandi et al., 1974*).

The main source of orbital variability clearly seen in Figures 5.6 and 5.8 results from the changing aspect of the X-ray irradiated face of the companion star. As seen from these Figures, the flux is expected to be maximum at $\phi_{\rm orb} = 0.50$ when the X-ray irradiated face of the companion star is most visible and minimum at $\phi_{\rm orb} = 0.00$ when the back of the companion star is visible (see Figure 5.13), resulting in a primary eclipse between $\phi_{\rm orb} \sim 0.90$ and $\phi_{\rm orb} \sim 0.10$. The dips (secondary eclipse) observed at $\phi_{\rm orb} \sim 0.50$ are caused by the eclipse of the inner face of the companion star by the accretion disc, i.e. the accretion disc casts its shadow on the inner face of the companion star, resulting in reduction of flux at this orbital phase.

Figures 5.7 and 5.9 clearly show the precessionally dependent variations in the orbital lightcurves

of Her X-1. This results from the variation in the projected shadow of the accretion disc on the irradiated face of the companion star as it precesses around the neutron star. This can be interpreted as a change in the shape of the accretion disc precessing around the central neutron star. This is consistent with the observation by GB76 that the precession cycle of Her X-1 is also observed in the optical wavelengths.

The lightcurves plotted in Figures 5.10 and 5.11 show similarities between the X-ray and optical lightcurves of Her X-1. This may suggest that both the X-ray and optical flux during the ALS originate from the same source, i.e. both dominated by emission from the inner face of the companion star. The changes in the shape of secondary eclipse between the precession phases 0.25 and 0.90 (Figures 5.10 and 5.11) are substantial and indicate significant effects. It is also observed that the secondary eclipse at precession phase 0.25 (Figure 5.10) is deeper in the X-ray than in the optical. This could probably imply that there is additional contribution to the X-ray flux from the comptonised accretion disc corona at this precession phase ($\phi_{35} = 0.25$). The same effect is not seen in the optical probably because the X-ray corona and the optical disc have different localities, one is a hot skin above the inner disc while the other is more broadly distributed across the photosphere of the outer disc. Therefore it is no surprise that their detailed behaviour across the 35-day precession cycle is different.

Figure 5.12 shows the ratio of the normal high state flux to the anomalous low state flux. From this figure it is observed that this ratio is $\lesssim 0.1$, probably implying that there is insignificant change in the 35-day morphology of the lightcurves between the ALS and the normal high state of Her X-1. This can also be observed from the mean orbital lightcurves shown in Figures 5.6 and 5.8. This may further imply that there is a very slight change in the disc morphology, i.e. a very slight change in the disc warp or vertical extent, when Her X-1 changes state from normal

high state to anomalous low state. This may be expected since the high orbital inclination of Her X-1 may imply that a very small increase in the disc warp may be sufficient to obstruct the X-ray flux from the neutron star from the observer. Assuming the dominant engine behind the disc warp in Her X-1 is radiation pressure, it can be argued that a slight increase in radiation pressure results in the ALS. A slight increase in the radiation pressure would in turn imply a slight increase in X-ray flux from the central accreting neutron star that can produce sufficient radiation pressure to warp the disc, and hence causing the ALS.

This chapter focused on the orbital lightcurves of Her X-1 in both optical and X-ray wavelengths. The next chapter will focus on the X-ray spectrum of Her X-1 taken during the anomalous low state. The main aim will be to investigate if increase in radiation pressure is the probable cause of the ALS.

Chapter 6

The Anomalous Low State Spectrum of Hercules X-1

6.1 Introduction

In this chapter the spectra of Her X-1 taken during the most recent (2003 - 2004) anomalous low state are analysed. The probable cause of the anomalous low state in Her X-1 is believed to result from an increase in the extent of the disc warp or an increase in the disc vertical scale height, although the mechanism responsible is still a matter of debate. However, radiation pressure (Pringle, 1996, 1997; Malony & Begelman, 1997 and Wijers & Pringle, 1998, 1999) has been proposed as the most likely cause of the disc warp in Her X-1. The main focus of this chapter is to investigate whether the increase in the disc warp in Her X-1 is a result of an increase in radiation pressure. This chapter also aims at establishing the dominant sources of X-ray flux during the anomalous low state. The data presented here were observed with the RXTE and the XMM-Newton observatories. The RXTE has already been briefly discussed in the previous chapters and in the following section, only a brief overview of XMM-Newton will be presented.

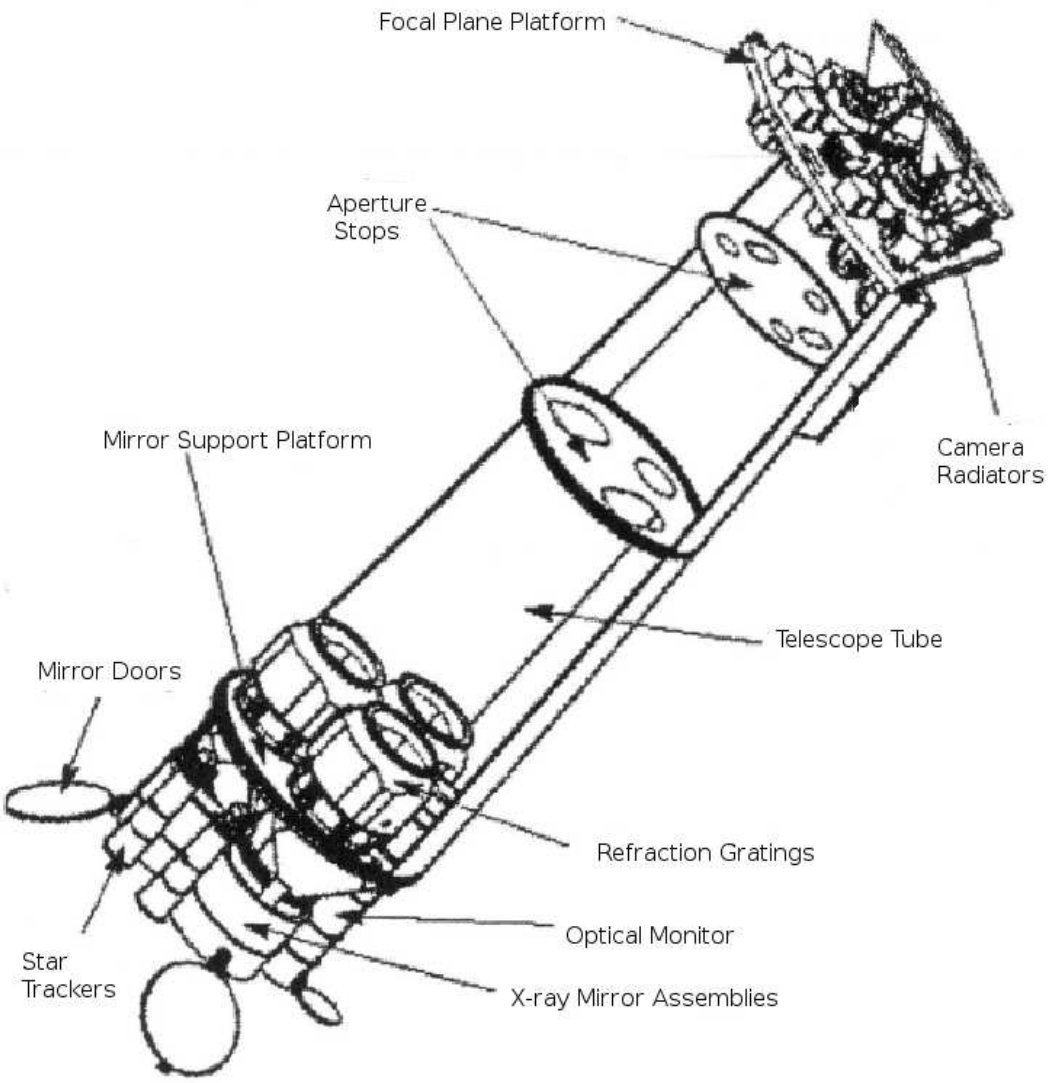

Figure 6.1: Schematic picture of an open view of the XMM-Newton observatory. (*Adopted from* http://sci.esa.int/science-e/www/object/).

6.2 The XMM-Newton Observatory

The X-ray Multi-mirror (XMM)-Newton observatory (Figure 6.1), a project of the European Space Agency, was launched in December 1999 into an orbit with a period of ~ 2 days (Jansen

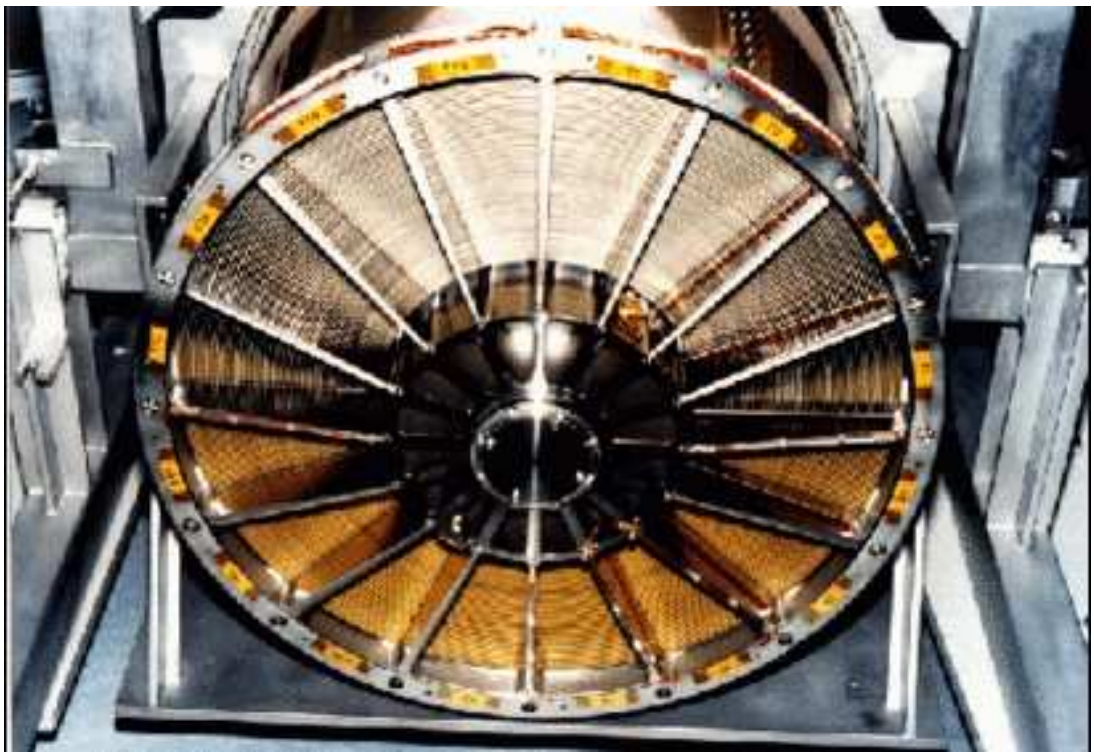

Figure 6.2: Picture of One of the three XMM-Newton mirror modules, seen from the back. (*Adopted from* http://sci.esa.int/science-e/www/object/).

et al., 2001). On board XMM-Newton are two Reflection Grating Spectrometer (RGS) cameras, three imaging cameras called European Photon Imaging Cameras (EPIC) and an Optical Monitor (OM) instrument. The EPIC has three broad-band imaging detectors with moderate spectral resolution. Two of the EPIC cameras use Metal Oxide Semi-conductor (MOS) Charge Coupled Device (CCD), i.e. EPIC-MOS detectors (Turner et al., 2001), and one contains p-n CCDs i.e. the EPIC-PN detector (Strüder et al., 2001). XMM-Newton has three X-ray telescopes with angular resolution of 4 - 6 arc sec (FWHM) and each telescope consists of 58 mirrors (Figure 6.2) of focal length 7.5 m and effective geometric area of 1500 cm^2 (Turner et al., 2001).

The EPIC instruments provide focal plane imaging and spectrometry for the X-ray telescopes,

one EPIC at the focus of each telescope. The two RGS instruments (de Herder et al., 2001) are fitted to two of the telescopes. During Science observations, all the three XMM-Newton instruments (RGS, EPIC and OM) are operated simultaneously. In the following section the EPIC-PN and EPIC-MOS instruments are briefly discussed since part of the data analysed here were obtained from observations done using these instruments. Most of the discussion on EPIC-PN is based on the paper by Strüder et al. (2001), while that on EPIC-MOS on the paper by Turner et al. (2001). For detailed discussions about these instruments the reader is referred to these papers.

6.2.1 The EPIC-PN

The EPIC-PN camera comprises of an array of 6×2 chips each having 64×200 pixels (Figure 6.3). The X-ray telescope in front of the EPIC-PN has an angular resolution of 6 arc sec (FWHM) at 1.5 keV and 8 keV (Strüder et al., 2001; Barcons, 2003). It has a pixel size of ~ 4 arc sec with a position resolution of 120 μm resulting in an equivalent resolution of 3.3 arc sec. This covers a field of view of about 30 arc min in diameter (Barcons, 2003) (see Figure 6.3). The camera has a high energy response ($> 90\%$ at 10 keV) as a result of the sensitive thickness of 300 μm.

The EPIC-PN has a filter wheel with six filter positions, four of which carry filters of different thickness. Since the EPIC CCDs are also sensitive to IR, visual and UV light, these filters are used to block any optical light. This is of importance particularly when the astronomical target has high optical to X-ray flux ratio resulting in the X-ray signal being contaminated by the optical flux. Of the remaining two positions, one is left open and the other closed by an aluminium plate of thickness 1 mm. This aluminium plate blocks the ionising radiation imaged through the mirror system. The operating temperature of the CCD is $-90°$C, although the thermal design

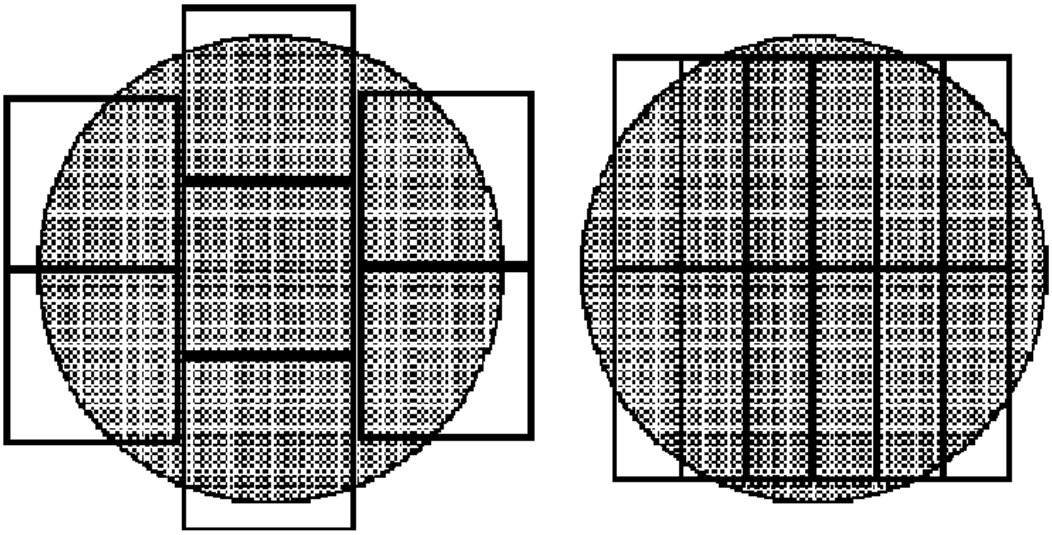

Figure 6.3: Schematic picture of the field of view of the two types of EPIC cameras. Left is the EPIC-MOS, while right is the EPIC-PN. The shaded circular region depicts a 30 arc min diameter covering the field of view. (*Adopted from* http://www.mssl.ucl.ac.uk/).

can enable the CCD temperature to go as low as $-140°$C while dissipating 0.9 W of the power in the focal plane.

For CCDs to be useful for simultaneous X-ray imaging and spectroscopic applications, the operations should be such that an X-ray photon must hit the detector without an overlap in time and position of another photon. For an X-ray camera readout to adopt to the source brightness, the CCD integration time should be shortened. This is done by reducing the area of the CCD to be readout. For the EPIC-PN camera, there are six readout modes (see Strüder et al., 2001 for detailed discussion).

6.2.2 EPIC-MOS

The EPIC-MOS camera has seven CCDs in the focal plane, each with 600×600 pixels. The CCDs are arranged as shown in Figure 6.3. The arrangement of the CCDs is such that one is central, at the focal point of the optical axis of the telescope, and the remaining six are stepped towards the mirror by 4.5 mm to nearly follow the focal plane curvature. This improves the focus for off axis sources. The imaging area of each CCD is $\sim 2.5 \times 2.5$ cm, covering a focal plane of 62 mm in diameter (~ 28.4 arc min) for a mosaic of seven. The EPIC-MOS has the same filter arrangement as the EPIC-PN.

The MOS-CCDs have a basic readout speed of 2.6 s on all the seven CCDs in each camera. This readout speed can be changed if the source observed is very bright or if there is need for fast timing observations. However, currently two readout window modes are implemented, i.e. the large window mode (300 $\times$ 300 pixels), with an integration time of 0.9 s and the small window mode (100 $\times$ 100 pixels) with integration time of 0.3 s. The MOS-CCDs image the entire field of view and give an energy and position of all the X-ray photons detected. The flux and spectrum of the X-ray source are then extracted from the images.

In general, the EPIC instruments have the capability to measure the energy of individual photons and is sensitive in the energy range 0.2 keV to 15 keV. They can detect X-ray sources as faint as $\sim 10^{-15}$ erg cm^{-2} s^{-1} in the 0.5 keV - 2 keV band in a few tens of kilo seconds. To cover the full field of view, the EPIC cameras are arranged such that the EPIC-PN is at 45° to the two EPIC-MOS. With this arrangement the grating diverts half of the flux out of the EPIC beam, with about 44% (allowing for structural obscuration) of the original flux reaching the two MOS cameras. The EPIC-PN has an unobstructed beam.

Table 6.1: Summary of the XMM-Newton observations of Her X-1 during the 2003 - 2004 Anomalous low state.

Observation	Start Time (UT)	Stop Time (UT)	Mid Orbital Phase
1	2004-02-09T02:12:20	2004-02-09T05:50:52	0.55
2	2004-02-11T01:53:01	2004-02-11T05:31:31	0.72
3	2004-02-23T01:20:10	2004-02-23T05:14:35	0.75

6.3 Observations

Her X-1 was observed with RXTE as previously discussed in Chapter 5 (see Tables 5.1 and 5.2 for a summary of the observations). During the same period XMM-Newton observations of Her X-1 were also scheduled. Summary of the XMM-Newton observations is shown in Table 6.1. In this chapter, data from the RXTE PCA and the three European Photon Imaging Cameras (i.e the two EPIC-MOS and the EPIC-PN) are analysed.

6.4 Data Reduction

6.4.1 RXTE PCA Data

The RXTE PCA data reduction was done as explained in Chapter 5. The source spectra were extracted from the same GoodXenon data used to extract the source lightcurves and the background spectra extracted from the same standard2 data as discussed in Chapter 5. The response matrices were generated using the "pcarsp" tool found within the FTOOLS. In each case the same GTI constructed for extraction of lightcurves were used. For the spectral analysis, the

energy range 3 to 30 keV was considered, i.e. energy range < 3 keV was ignored because of uncertain background modelling and energy range > 30 keV was ignored because of poor counting statistics. An additional 2% systematic error (Wilms et al., 1999) was added to the statistical errors.

6.4.2 XMM-Newton Data

The extraction of science products from the Observation Data Files (ODFs) followed the standard procedures within the *XMM-Newton Science Analysis System*, Issue 4.0 and *An Introduction to the XMM-Newton Data Analysis*, Version 2.01. The calibration files, i.e. the Current Calibration Files (CCFs) were downloaded from the Science Operation Centre XMM-Newton calibration page (http://xmm.vispa.esa/ ccf/) and the calibration index files rebuilt from the CCFs using the "cifbuild" task.

The source spectra from each of the three EPIC instruments were extracted from a circular region centred on the source (Her X-1), while the background spectra were extracted from a region within an annulus drawn around the source (Figure 6.4).

The response matrices and ancillary response matrices were created for each spectrum using the "rmfgen" and "arfgen" tasks respectively, which are found within the XMM Science Analysis Software (XMM-SAS) which was used for data extraction. The data, i.e. spectra, were then grouped using the "grppha" task found within the FTOOLS, with a binning factor of 25 counts per bin. This grouping or binning is required in order to get sufficient counts per bin to make the chi-square (χ^2) spectral fitting a valid statistical process. For spectral analysis the energy range 0.2 keV to 12 keV was considered for the EPIC-MOS, while the range 0.2 - 15 keV was considered for the EPIC-PN.

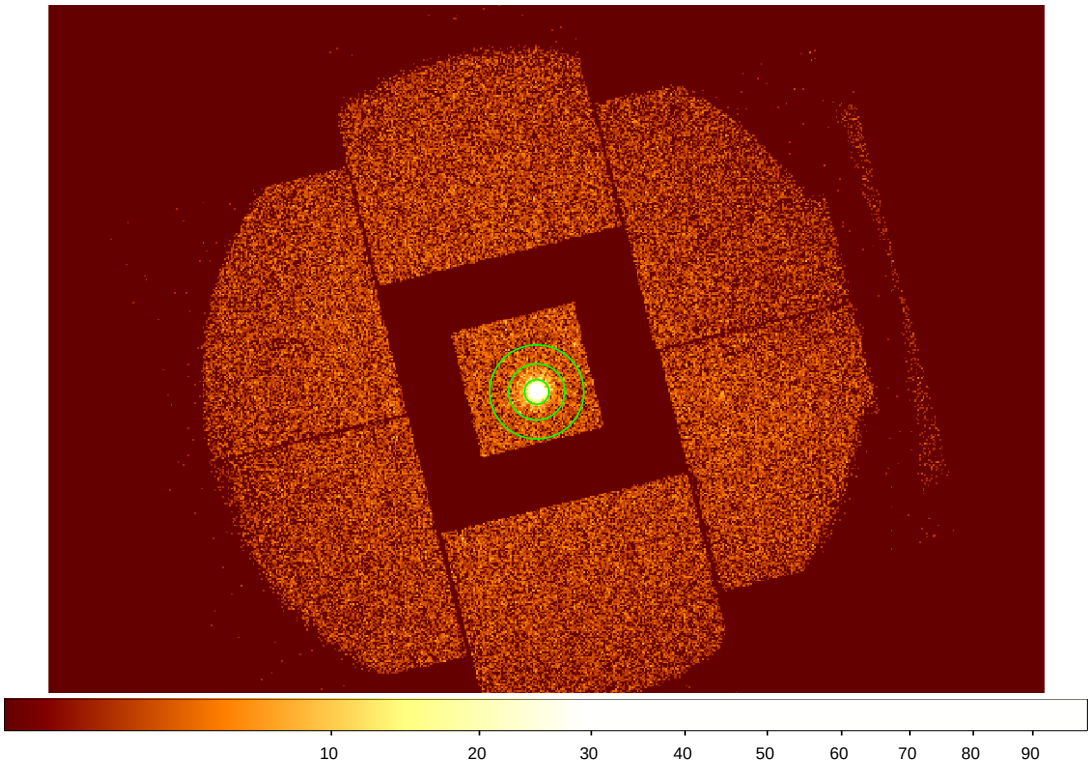

Figure 6.4: Picture showing the region of extraction of source spectrum (inner circle) and the background spectrum (annulus around the source) for the MOS1 instrument.

6.5 Spectral Analysis

The spectrometers used to obtain X-ray spectra do not give the actual spectrum but rather photon counts within specific instrument channels. The relationship between the observed spectrum $N(I)$ and the actual spectrum $S(E)$ is given by the equation (Arnoud, Dorman & Gordon, 2005 and references therein)

$$N(I) = \int_0^\infty S(E)R(I,E)\ dE, \tag{6.1}$$

where $R(I,E)$ is the detector response function and is proportional to the probability that an incident photon with energy E will be detected in channel I.

The major aim of spectral analysis is to compare the observed photon spectra of astrophysical objects to theoretical model spectra in order to deduce physical parameters of the observed object from the data. The approach is normally to choose a model spectrum and fit it to the observed spectrum. The model spectrum is usually described in terms of some physical parameters. For each model spectrum chosen, a predicted count spectrum is computed and is then fitted to the observed spectrum. This process is repeated while varying the physical parameters of the model spectrum until a minimum deviation is obtained between the model and observed spectra. The values of the parameters, in the case where minimum deviation is obtained, are called the best-fit parameters.

The goodness of a fit, i.e. best-fit, is determined by the χ^2-statistics defined by (see Arnoud, Dorman & Gordon 2005, and references therein for a detailed discussion)

$$\chi^2 = \sum_{I=1}^{N} \frac{(C_{\rm obs}(I) - C_{\rm model}(I))^2}{(\sigma(I))^2}, \tag{6.2}$$

where $C_{\rm obs}(I)$ is the total number of counts in channel I of the background subtracted observed spectrum, $C_{\rm model}(I)$ the number of counts in channel I of the model spectrum and $\sigma(I)$ the variance of the observed data in channel I. The parameter $\sigma(I)$ can be estimated by $[C_{\rm obs}(I)]^{1/2}$. More conveniently the reduced chi-square, χ^2_ν, is used and is given by

$$\chi^2_\nu = \frac{\chi^2}{N_{\rm dof}}, \tag{6.3}$$

where $N_{\rm dof}$ is the number of degrees of freedom, which is calculated as the number of channels minus number of model parameters.

The χ^2_ν has the expectation value of one (see Lampton, Margon & Bowyer (1976) for detailed discussion). For values of $\chi^2_\nu >> 1$, it implies a low probability that the model spectrum is

in agreement with the observed spectrum, while $\chi^2_\nu << 1$ implies the uncertainties ($\sigma(I)$) are incorrect, e.g. by over estimating the systematic error. In the fitting process, a set of parameters of the model spectrum which best describes the observed spectrum are obtained.

6.5.1 The Spectral Model for Her X-1

The X-ray spectrum of the X-ray binary Her X-1 has been well studied (e.g. Manchanda, 1977 and references therein; Trümper et al., 1977, 1978; McCray et al., 1982; White, Swank & Holt, 1983; Nagase, 1989; Mihara et al., 1991; Oosterbroek et al., 1997; Dal Fiume et al., 1998; Santangole et al., 1998; Oosterbroek et al., 2000; Still et al., 2001b; Kuster et al., 2005). In the energy range $\sim 2 - 20$ keV the high state intensity has successfully been fitted by a model consisting of a power law with high energy exponential cut-off (White, Swank & Holt, 1983; Dal Fiume et al., 1997 and references therein). The spectrum in the energy range 0.1 - 200 keV has revealed additional components, i.e. a low energy absorption consistent with the interstellar value (Dal Fiume et al., 1998), a ~ 0.1 keV blackbody which dominates the spectrum below ~ 1 keV (Mavromakis, 1993; Oosterbroek et al., 1997), Fe K emission line at 6.4 keV and 6.7 keV (Choi et al., 1994, 1997; Still et al., 2001b; Fabian et al., 2000 and Kuster et al., 2005) and high energy exponential cut-off $\gtrsim 10$ keV. A broad feature centred at 53 keV (see Figure 2.2) has been observed (Trümper et al., 1977). This broad feature has been interpreted as cyclotron emission (Trümper et al., 1977). The X-ray spectra of Her X-1 in the energy range 1 - 100 keV is shown in Figure 6.5 (see Manchanda, 1977 for detailed discussion).

The observed spectrum of Her X-1 seems to show three different components in the continuum (Dal Fiume et al., 1998; Santangole et al., 1998; Oosterbroek et al., 2000 and Still et al., 2001b). These components are a low energy excess modelled as 0.1 keV blackbody, power law and a high energy exponential cut-off. Also superimposed in the continuum are emission lines, e.g.

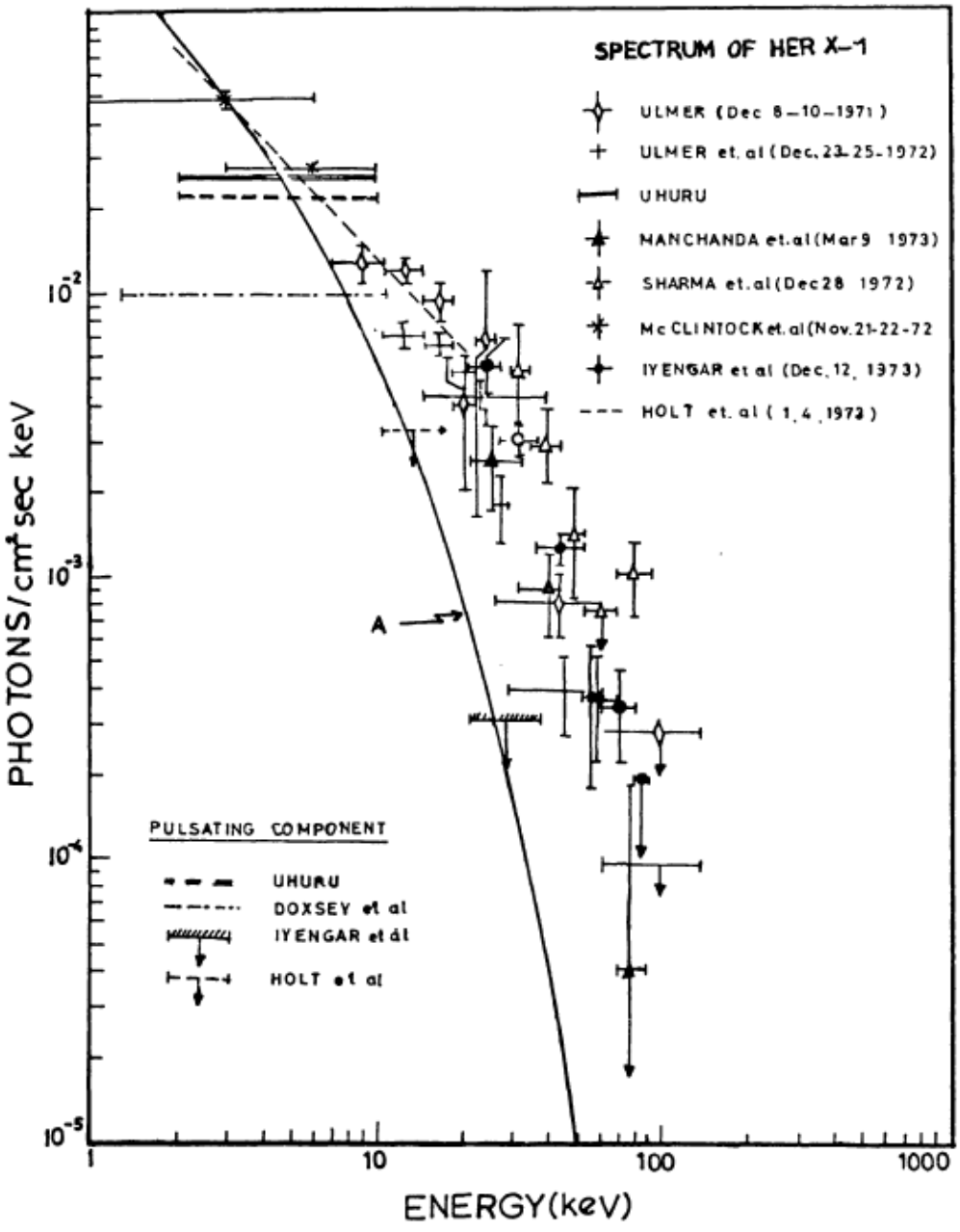

Figure 6.5: The X-ray spectrum of the X-ray binary Her X-1 in the energy range 1 - 100 keV. (*Adopted from Manchanda, 1977).*

iron emission lines at ~ 6.4 keV and ~ 6.7 keV (Choi et al., 1997; Still et al., 2001b; Fabian et al., 2002 and Kuster et al., 2005).

As already discussed in Chapter 5, the X-ray flux observed during the anomalous low state of Her X-1 originates from two distinct binary regions: the irradiated or inner face of the companion star and the accretion disc corona. Since one of the aims of this analysis is to separate the two components, i.e. the coronal component and the reflection component, it is appropriate to use a two component model to fit the anomalous low state spectrum of Her X-1. From the model fitting the physical parameters of the corona and reflection can then be derived.

The spectral models for Her X-1, during the anomalous low state, were fairly well established by Still et al. (2001b). In these models the emission originates from two binary regions: the accretion disc corona and the companion star. The coronal emission results from up-scattering of soft disc photons in a relatively hot medium. Still et al. (2001b) established a simple but physically realistic coronal model that is compatible with fits made by Coburn et al. (2000) in an earlier ALS of Her X-1. This model consists of a partial-covering cold absorber (i.e. contains both overall absorption represented by "WABS" and partial absorption represented by "PCFABS" in the XSPEC user guide), a power law with high-energy exponential cut-off (represented by "CUTOFFPL" in XSPEC user guide) and a Gaussian Fe emission line (represented by "GAUSS" in the XSPEC user guide). This coronal model can be expressed as

$$I_{\rm cor}(E) = P(E)\,\exp[-N_{\rm H}\sigma(E)]\left[A\,\exp\left(-\frac{E}{E_{\rm cut}}\right)E^{\alpha} + G(E)\right] \tag{6.4}$$

where $P(E) = f\,\exp[-N_{\rm H}\sigma(E)] + (1-f)$ and $G(E) = A\frac{1}{\sigma_{\rm k}(2\pi)^{0.5}}\,\exp\left[-\frac{(E-E_{\rm k})^2}{2\sigma_{\rm k}^2}\right]$,

with f representing the partial covering fraction, $N_{\rm H}$ the hydrogen column density, A the nor-

malisation, $\sigma(E)$ the photoelectric cross-section, $E_{\rm cut}$ the cut-off energy, $\sigma_{\rm k}$ the line width and α the power law photon index.

The emission from the companion star (reflection component) is a result of scattering of hard radiation from the compact accreting neutron star off the relatively cool atmosphere of the companion star or the accretion disc. Still et al. (2001b) observed that the reflection spectrum would suffer photoelectric absorption at energies < 10 keV, and have strong Fe Kα line and would be down-scattered at energies > 50 keV. Still et al. (2001b) developed a Compton reflection model, $\mathscr{L}(E)$, as an external multiplicative XSPEC package which was used to fit the reflection model. This reflection model assumes an isotropically radiating point source of a given energy spectrum and flux that irradiates a structure subtending an angle $\omega = 0.15\pi$ (Still et al., 2001b) on the sky with respect to the source. In developing this model, the surface of a Roche lobe-filling star is divided into small elements. Each element has an individual inclination angle with respect to the earth, and an individual grazing incidence angle and filling factor (i.e. the fraction of the sky occupied by a slab) with respect to the X-ray source. These parameters are then determined over a grid using Roche geometry and sum the reflection spectrum over all the surface elements visible to the observer. The parameters of the reflection model are stellar mass ratio $q = M_c/M_*$ where M_c and M_* represent the mass of the companion star and compact object respectively, orbital inclination, orbital phase, Fe K_α edge and Fe abundance which is adopted as solar. The model allows the fit to be made at any orbital phase, $\phi_{\rm orb}$. The mass ratio defines the shape of the companion star and the area of the pulsar sky each surface element occupies. The overall reflection model is represented by

$$I_{\rm refl}(E) = \exp[-N_{\rm H}\sigma(E)] \left[A \exp\left(-\frac{E}{E_{\rm cut}}\right) E^{\alpha} \times \mathscr{L}(E) + G(E) \right]. \qquad (6.5)$$

For detailed discussion of the Compton reflection model $\mathscr{L}(E)$ see Still et al. (2001b).

6.5.2 Spectral Fitting

RXTE PCA Spectra

The spectral fitting was performed following standard procedures in XSPEC version 12.2.1 (Arnaud, Darman, & Gordon, 2005). The coronal model (Equation 6.4) was fitted to the spectrum at $\phi_{\rm orb} = 0.130$. At this orbital phase the X-ray is presumably dominated by emission from the corona and any contribution from the reflection component is assumed to be insignificant. As already discussed, this emission results from up-scattering of soft disc photons in the relatively hot corona. In the fitting some parameters were fixed. This was done in order to reduce the excessive number of free parameter, thus enabling the column density and the covering fraction to be well constrained (Still et al., 2001b). The fixed parameters are: the interstellar column density at 5.1×10^{19} cm^{-2} (Dal Fiume et al., 1998), the power law slope at $\alpha = 0.9$ (Dal Fiume et al., 1998), i.e. the power law slope fixed at its high state value because the anomalous low state is assumed to result from obscuration of the central accreting neutron star rather than intrinsic source behaviour, and the emission line at 6.7 keV (Choi et al., 1997; Still et al., 2001; Kuster et al., 2005). This produced a reasonably good fit (Figure 6.6) yielding $\chi^2_\nu = 0.71$ for 49 degrees of freedom (dof).

Since one of the aims of this spectral analysis is to separate the coronal and reflection components, the coronal model (Equation 6.4) was fitted to the spectrum at orbital phase $\phi_{\rm orb} = 0.506$ (where emission by Compton reflection is assumed to dominate the spectrum) with all the parameters frozen at the values obtained from the phase $\phi_{\rm orb} = 0.130$ fit. This gave a poor fit yielding $\chi^2_\nu = 33.9$ for 58 dof (see Figure 6.7). This could probably be as a result of the flux at $\phi_{\rm orb} = 0.506$ being higher than that at $\phi_{\rm orb} = 0.130$. Keeping the flux as a free parameter still yielded a poor fit with $\chi^2_\nu = 2.45$ for 57 dof (Figures 6.7 and 6.8).

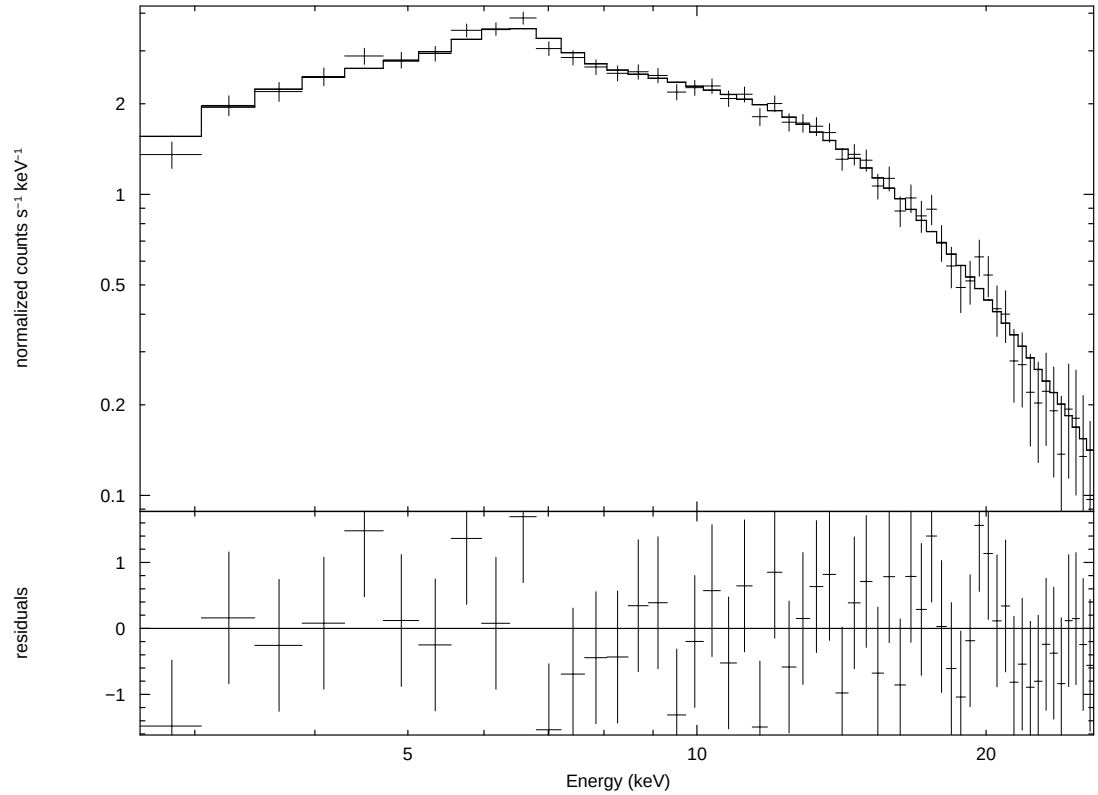

Figure 6.6: Top panel: RXTE PCA spectrum of Her X-1 at $\phi_{\rm orb} = 0.130$. Over lapping the spectrum is the best-fit coronal model (Equation 6.4). Bottom panel: The residuals i.e. data minus model.

The reflection model (Equation 6.5) was then added to the coronal model (i.e. a two-component model used) and the fit performed. The following parameters of the Compton reflection model $\mathscr{L}(E)$ were fixed: mass ratio at 1.57, inclination at $82°$, Fe abundance at 1.418 and Fe Kα edge at 7.11 keV. The orbital phase for the visit was also maintained as a fixed parameter. In fitting this two component model the initial approach was to freeze all the coronal parameters, but this gave a poor fit yielding $\chi^2_\nu = 2.9$. Keeping the parameters of the partial covering absorption (PCFABS) for the coronal model free, gave a reasonable fit yielding $\chi^2_\nu = 0.70$ for 52 dof (see

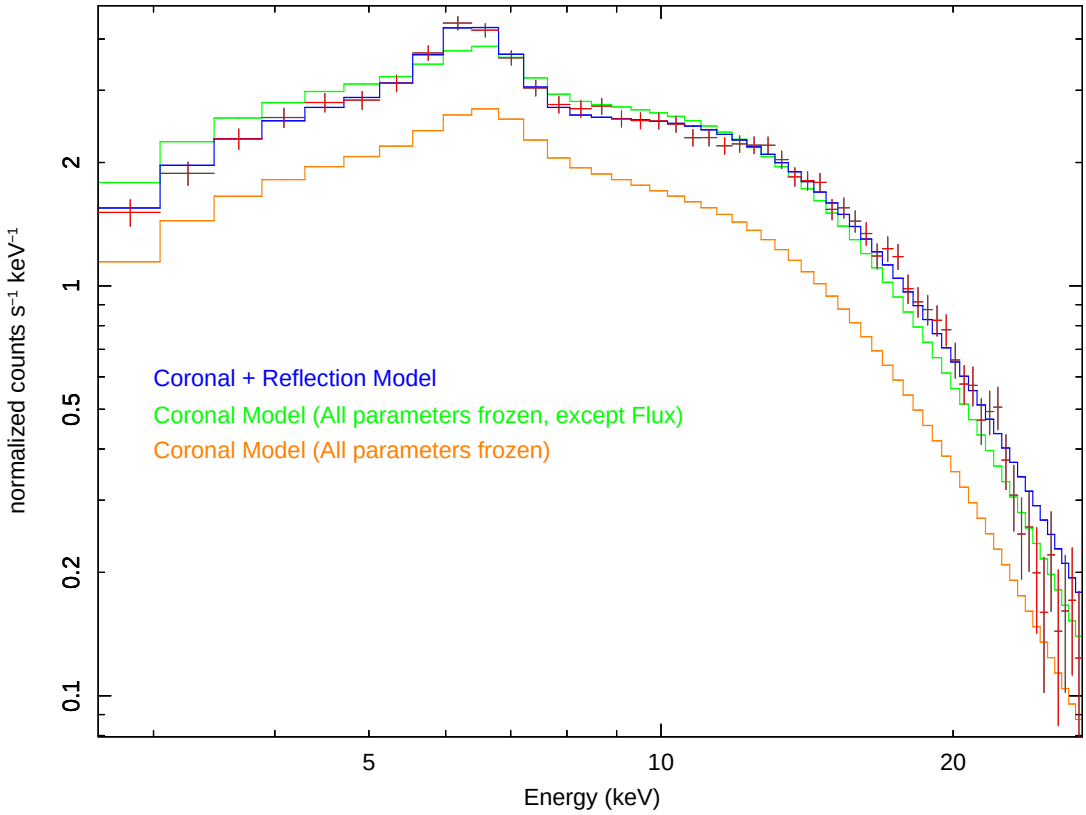

Figure 6.7: RXTE PCA spectrum of Her X-1 at $\phi_{\rm orb} = 0.506$ showing to the best fit coronal models and the two component (coronal + reflection) model.

Figures 6.7 and 6.9). This is expected because the corona seems to be varying. Table 6.2 gives the best fit parameters for the models. These models were fitted to the spectra of the other visits and the results are shown in Figures 6.10 and 6.11. A plot of the best-fit parameters for the RXTE PCA spectra for all the visits is shown in Figure 6.12. From this figure it is observed that the 3 - 30 keV flux from the companion star is modulated on the orbital period and has the same profile with the lightcurves shown in Figures 5.10 (top panel) and 5.11 (top panel) as expected. The Gaussian line strength A_k is also modulated on the orbital period. The coronal parameters, N_H and f, do not show any modulation on the orbital period as expected.

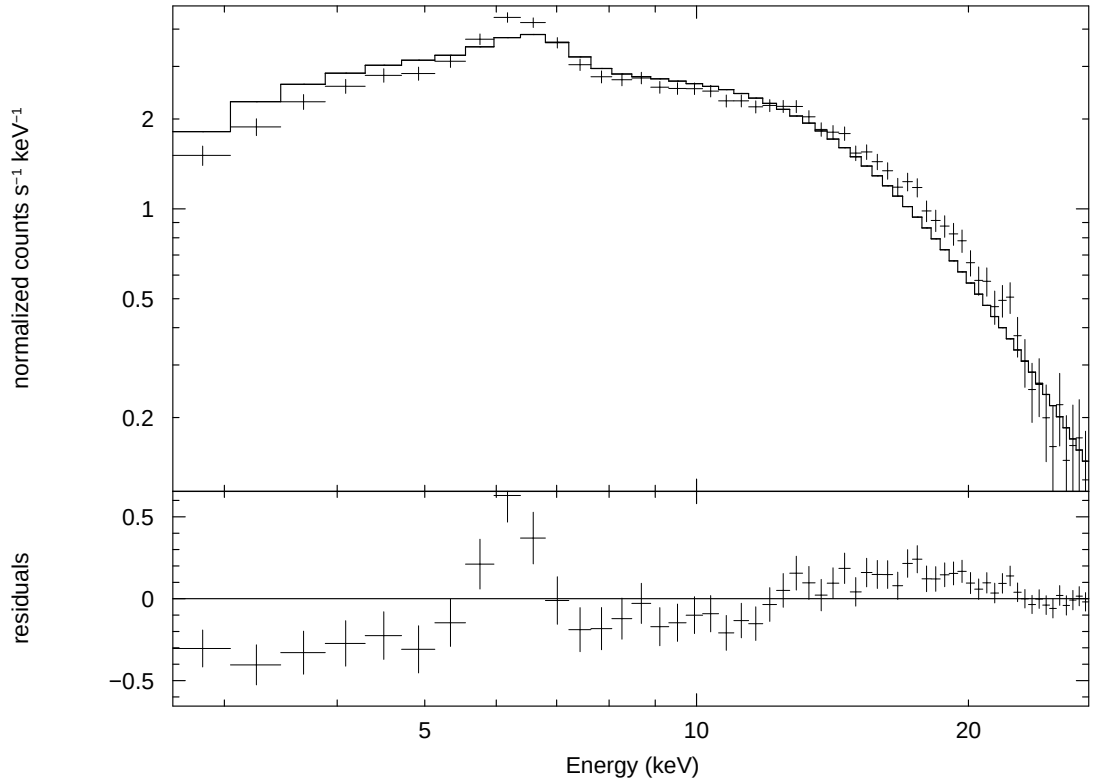

Figure 6.8: Top panel: RXTE PCA spectrum of Her X-1 at $\phi_{\rm orb} = 0.506$ showing to the best fit coronal model with all the parameters fixed at the values obtained from the $\phi_{\rm orb} = 0.130$ fit, except for the flux. Bottom panel: The residuals.

6.6 XMM-Newton and RXTE Spectra

The XMM-Newton and RXTE cover different energy bands, i.e. RXTE covers a higher energy band while XMM-Newton covers a lower energy band. Therefore to constrain the continuum better, the RXTE and XMM-Newton spectra were simultaneously fitted together. The idea of simultaneously fitting the RXTE and XMM-Newton spectra is also to extrapolate the model obtained using the RXTE PCA spectra to fit the soft X-ray (soft X-ray spectra obtained using XMM-newton). In this way the model obtained using the RXTE data is verified by the XMM-Newton data.

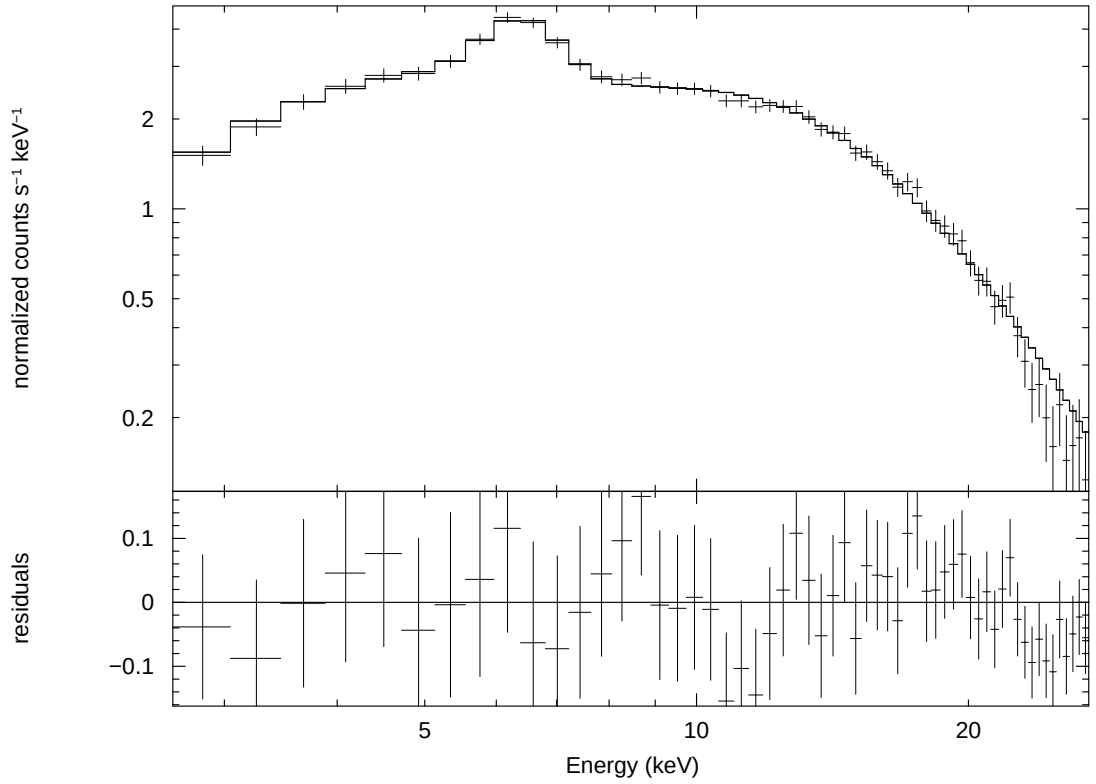

Figure 6.9: Top panel: RXTE PCA spectrum of Her X-1 at $\phi_{\rm orb} = 0.506$. Overlapping is the best-fit model, i.e. coronal model (Equation 6.4) plus reflection model (Equation 6.5). The residuals shown in the bottom panel.

In fitting the two data sets simultaneously, the two component model (i.e. Equations 6.4 and 6.5) was used. In addition an energy independent multiplicative factor (i.e. a constant factor) was included in the model and its value was fixed to one for the XMM-Newton data and kept as a free parameter for the RXTE data. This multiplicative factor is used to scale the two data sets. When fitting this model to the spectrum at $\phi_{\rm orb} = 0.55$, a poor fit, yielding $\chi^2_\nu = 3.49$ for 2351 dof, was obtained. The result of this fit shows an excess of soft X-ray component below about 0.7 keV (Figure 6.13). The soft X-ray excess was modelled by including a blackbody component

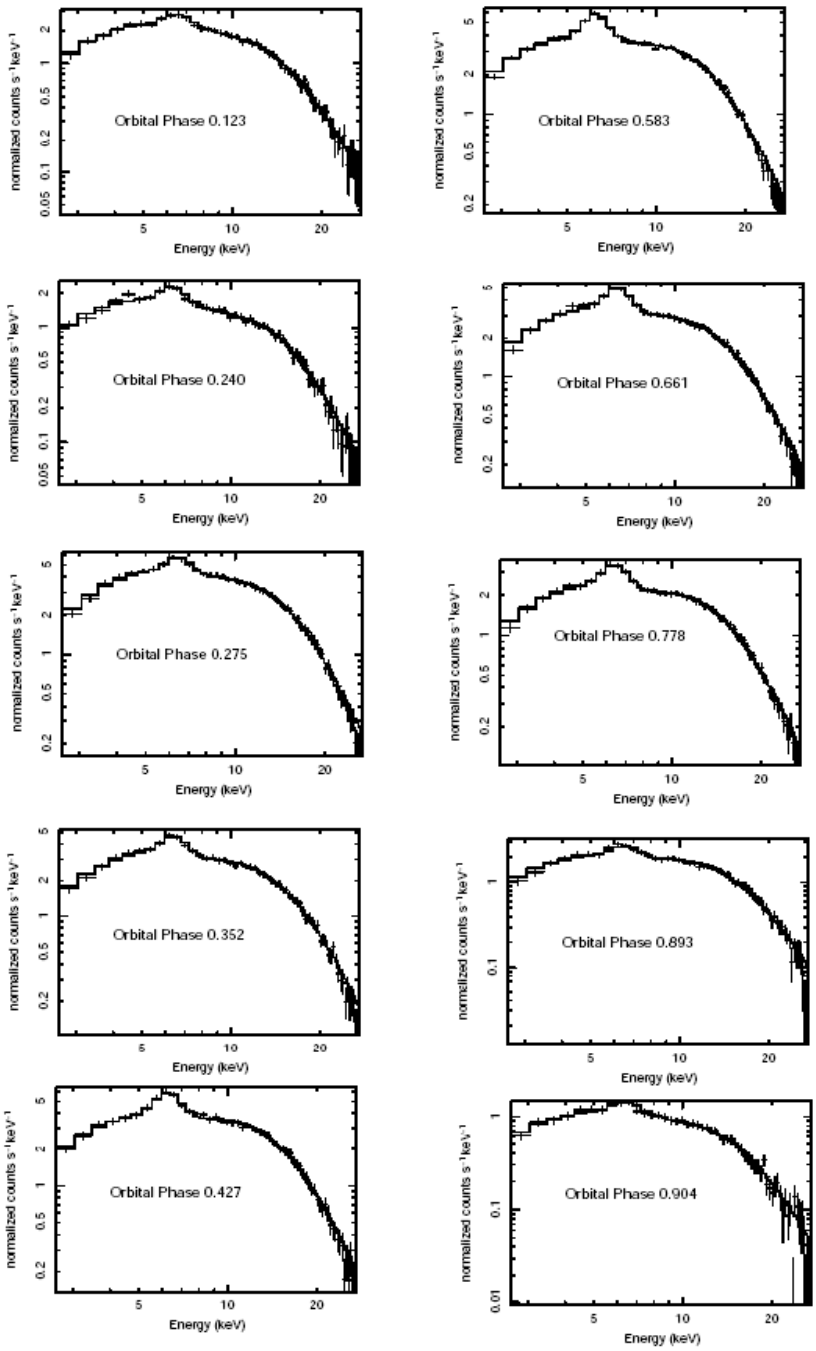

Figure 6.10: RXTE PCA spectra for the precession phase 0.25, except for orbital phase 0.904 which is from precession phase 0.90. Overlapping each spectrum is the best fit model. The orbital phases are indicated in each plot.

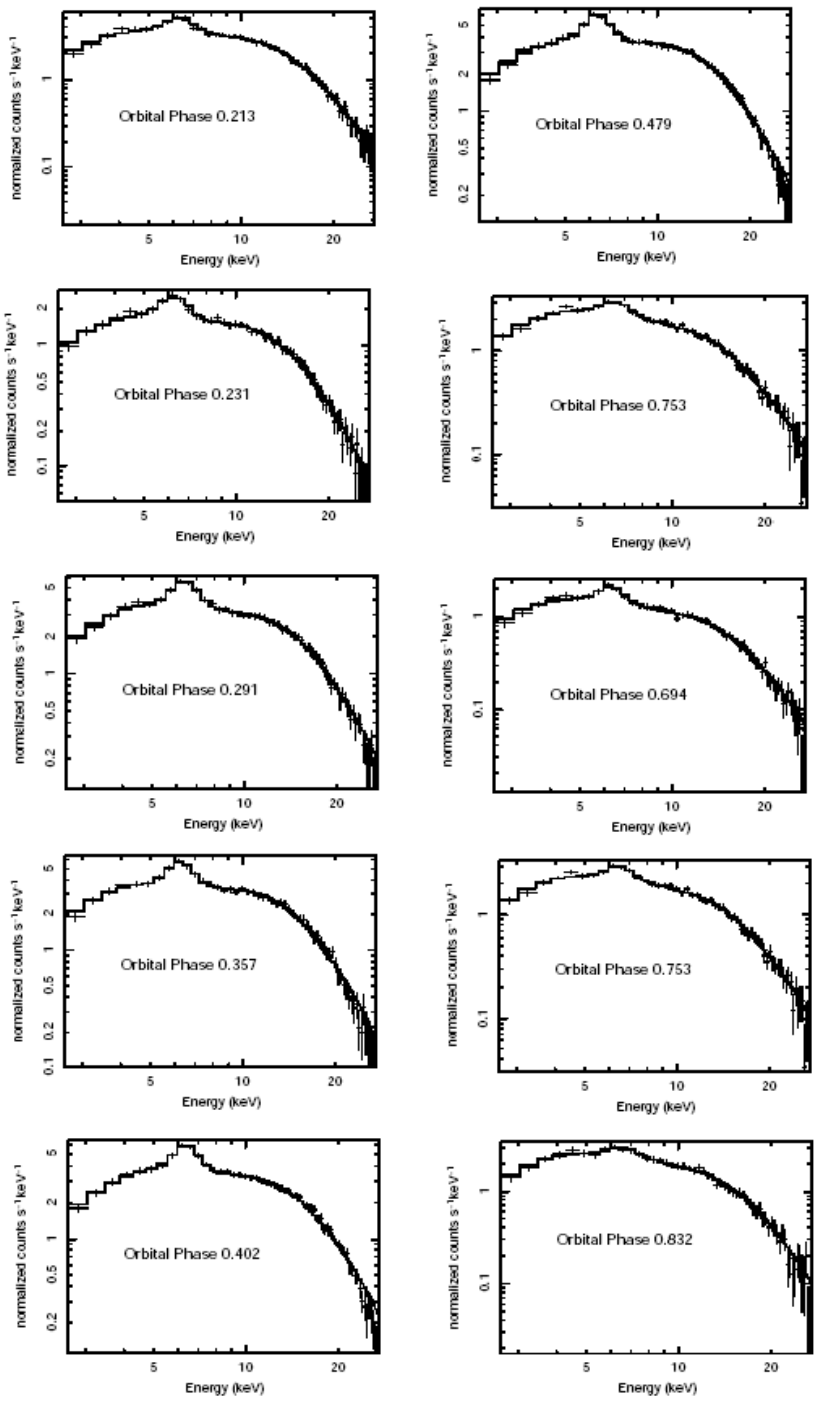

Figure 6.11: RXTE PCA spectra for the precession phase 0.90. Overlapping each spectrum is the best fit model. The orbital phases are indicated in each plot.

Table 6.2: Best-fit parameters for the coronal model and the two component model for the spectra at orbital phase $\phi_{\rm orb} = 0.506$. For the coronal model all the parameters are fixed at the values obtained from the phase $\phi_{\rm orb} = 0.130$ fit, except for the flux ($A_{\rm cor}$). The flux obtained at the $\phi_{\rm orb} = 0.130$ fit is 1.5 $\times 10^{-2}$ ph cm^{-2} s^{-1} keV^{-1}.

Parameter	Coronal Model	Reflection + Coronal Model
$N_{\rm H} \times 10^{22}$ cm^{-2}	88 ± 13	101 ± 20
f	0.77 ± 0.04	0.81 ± 0.02
$A_{\rm cor}$ (ph cm^{-2} s^{-1} keV^{-1})	$(2.4 \pm 0.2) \times 10^{-2}$	$(1.9 \pm 0.2) \times 10^{-2}$
$A_{\rm ref}$ (ph cm^{-2} s^{-1} keV^{-1})	-	0.19 ± 0.03
E_k (keV)	-	6.39 ± 0.02
A_k (ph s^{-1} cm^{-1})	-	$3.2 \pm 0.04 \times 10^{-4}$
χ^2_ν	2.45	0.70

with its own absorption term $(\exp[-N_{\rm H2}\sigma(E)])$. The blackbody component is given by

$$B(E) = \frac{A_{\rm bb} \times 8.0525E^2}{(kT)^4 \left[\exp\left(\frac{E}{kT}\right) - 1\right]}, \tag{6.6}$$

where kT is the blackbody temperature in keV and $A_{\rm bb}$ is the normalisation (see Arnaud, Dorman & Gordon, 2005 for detailed discussion). In the fitting, the blackbody temperature was fixed at a value of 0.1 keV (e.g. Santangelo et al., 1998 and Ramsay et al., 2002). This gave a fit (Figure 6.14) yielding a $\chi^2_\nu = 1.28$ with 2350 dof. Although a reduced chi-square of one is expected for the best fit, a value of $\chi_\nu = 1.28$ is reasonable. This model was then fitted to the spectra at $\phi_{\rm orb} = 0.72$ and $\phi_{\rm orb} = 0.75$ (Figure 6.15). The best-fit parameters for these fits are shown in Table 6.3. From the best fit parameters shown in Table 6.3, it is observed that there is no significant difference between the two absorbing terms, i.e N_H and N_{H2}.

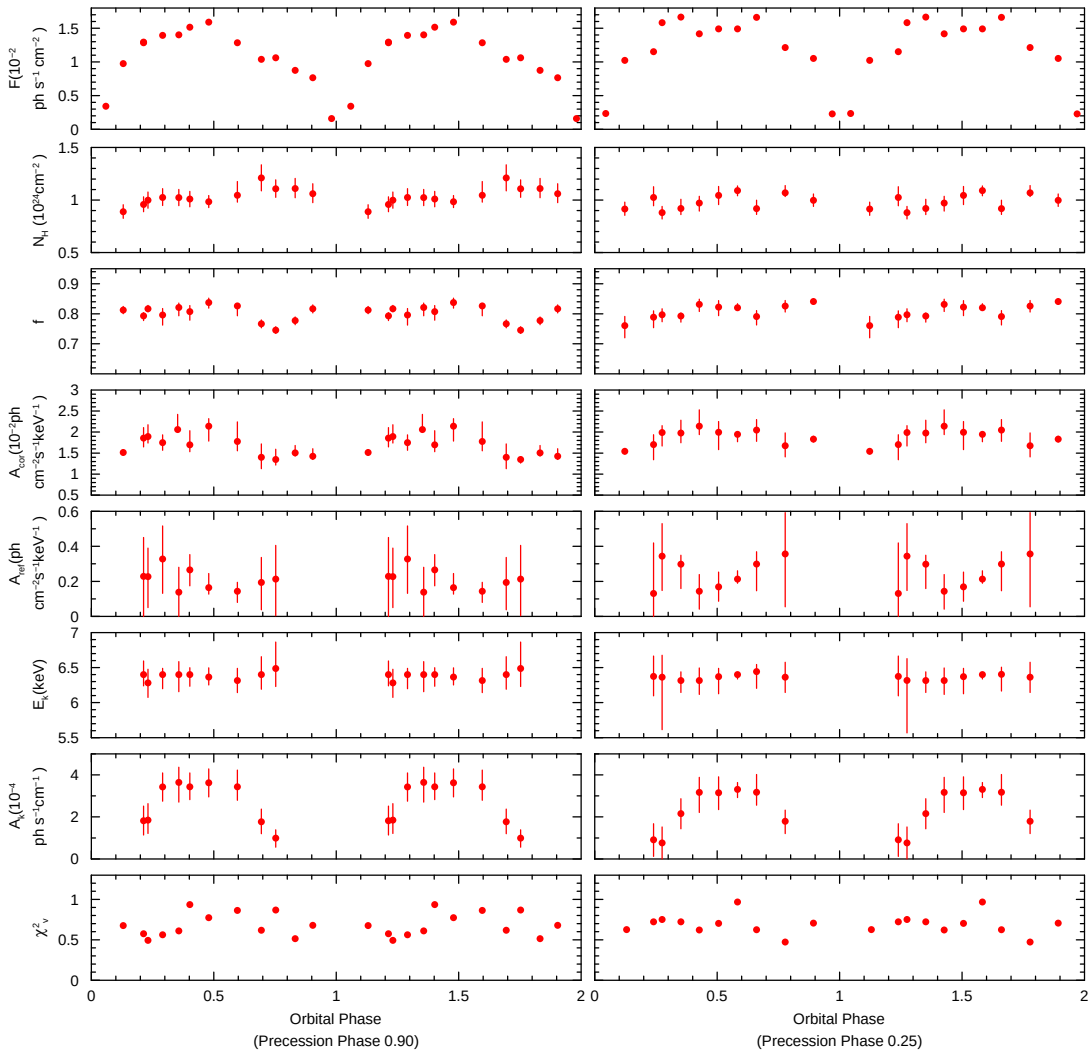

Figure 6.12: Plot of the best fit parameters. The parameters from the top panel are: The 3 - 30 keV flux, F, from the companion star, the neutral hydrogen column density $N_{\rm H}$, covering fraction f, the flux giving rise to the coronal component $A_{\rm cor}$, the hidden flux from the neutron star giving rise to the reflection component $A_{\rm ref}$, the line centre for ~ 6.4 keV Fe emission $E_{\rm k}$, the line strength of the ~ 6.4 keV line $A_{\rm k}$, and the reduced chi-square statistics χ^2_ν. The orbital phase is plotted twice for clarity.

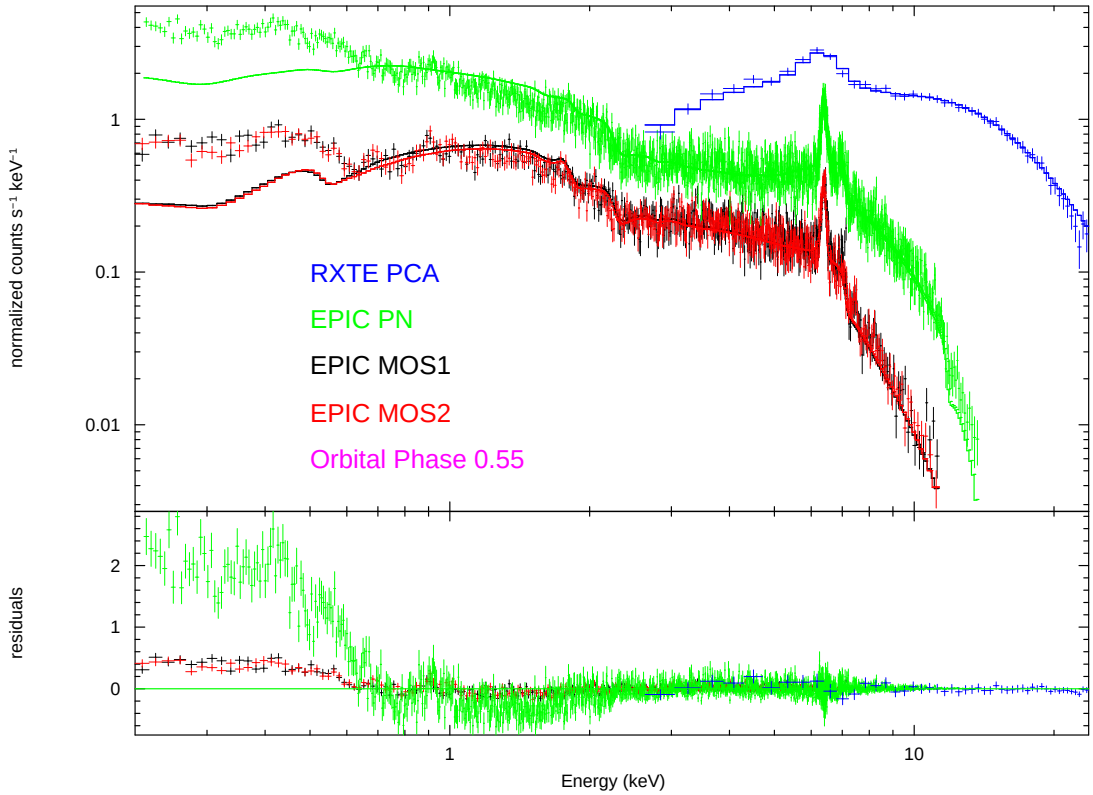

Figure 6.13: Top panel: RXTE PCA and XMM-Newton spectra of Her X-1 showing the soft X-ray excess below ~ 0.7 keV. Bottom panel: The residuals.

6.7 Discussion

The main focus of this chapter was to investigate if an increase in radiation pressure is the most likely cause of the change in the accretion disc warp resulting in the anomalous low state of Her X-1. This was done by measuring the hidden flux from the compact accreting neutron star during the anomalous low state and comparing it with the flux during the normal high state. The average value of the hidden photon flux (calculated from the values of $A_{\rm ref}$, see fifth panel from top in Figure 6.12), i.e. the intrinsic flux of the neutron star that gives rise to the reflection component, at 1 keV was found to be 0.23 ± 0.04 photons cm^{-2} s^{-1} keV^{-1}. From the simultaneous fitting of the XMM-Newton and RXTE spectra the average value of the hidden flux from

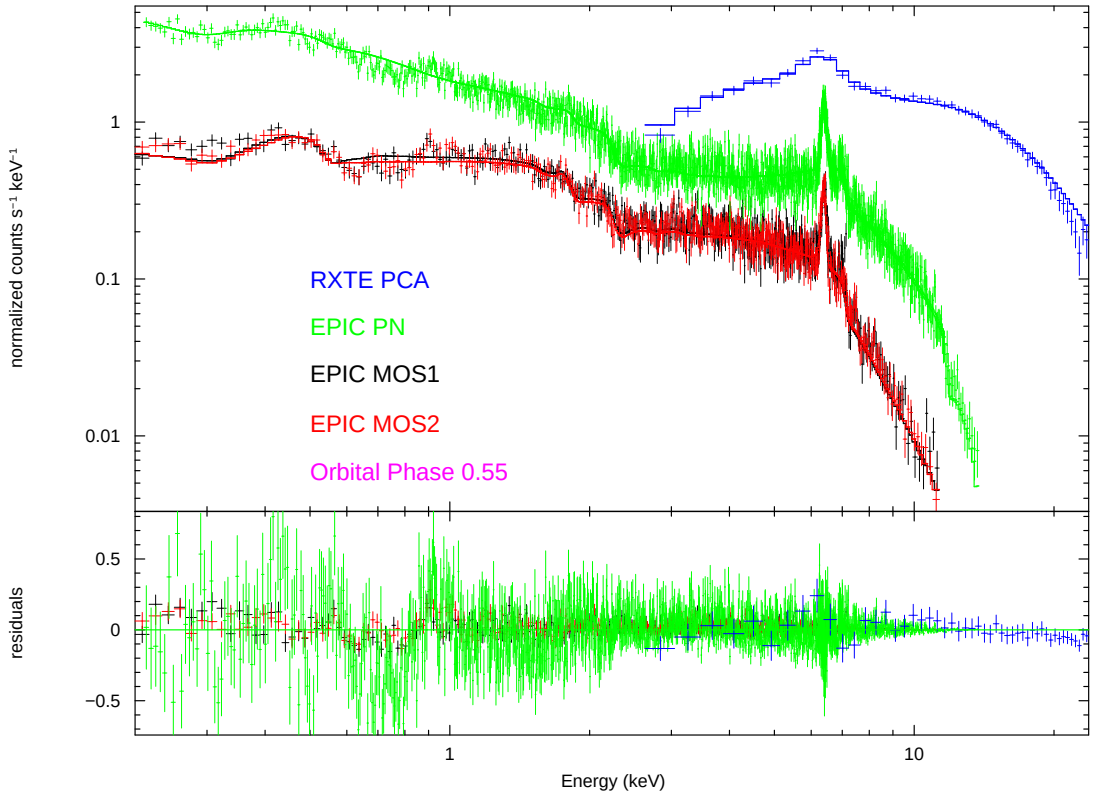

Figure 6.14: Top panel: RXTE PCA and XMM-Newton spectra of Her X-1. Overlapping the spectra is the best fit model when the blackbody component was added to the two model component. Bottom panel: The residuals.

the neutron star was measured to be 0.29 $\pm$ 0.02 photons cm^{-2} s^{-1} keV^{-1}, i.e. the average value of A_{ref} in Table 6.3. The typical flux of Her X-1 at 1 keV during the normal high state is 0.1 photons cm^{-2} s^{-1} keV^{-1} (Dal Fiume et al., 1998). This implies that Her X-1 was brighter by a factor of $\sim 2-3$ during the 2003 - 2004 anomalous low state compared to its brightness during the normal high state. When the spectral model was extrapolated to fit the soft X-ray (i.e. simultaneously fitting the RXTE and XMM-Newton spectra), a constant scaling factor of ~ 1.26 was obtained between the XMM-Newton and RXTE data. Although a constant scaling factor of 1 is expected to verify this result, a value of ~ 1.25 is still reasonable within the error

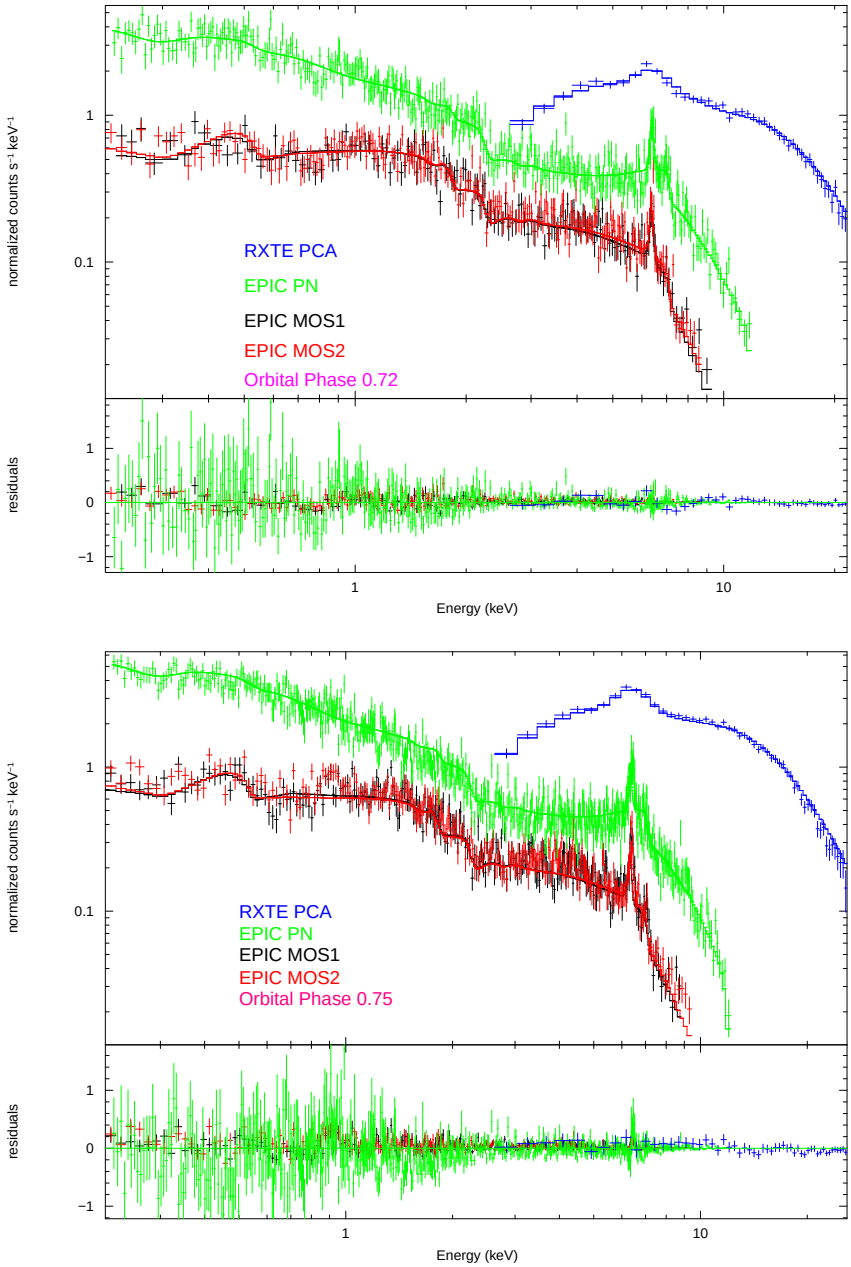

Figure 6.15: RXTE PCA and XMM-Newton spectra of Her X-1. Overlapping the spectra are the best fit models. The residuals are shown in the bottom panel of each plot.

Table 6.3: Best-fit parameters for the RXTE and XMM-Newton spectra of Her X-1 during 2003 - 2004 Anomalous low state.

Orbital phase	0.55 (2 PCUs)	0.72 (2 PCUs)	0.75 (3 PCUs)
const. factor	1.25 ± 0.30	1.26 ± 0.30	1.25 ± 0.20
$N_H \times 10^{22}$ cm^{-2}	153 ± 12	151 ± 20	152 ± 7
$N_{H2} \times 10^{22}$ cm^{-2}	160 ± 20	159 ± 17	161 ± 19
f	0.81 ± 0.01	0.79 ± 0.01	0.79 ± 0.01
A_{cor} (ph cm^{-2} s^{-1} kev^{-1})	$(7.53 \pm 0.3) \times 10^{-3}$	$(7.30 \pm 0.2) \times 10^{-3}$	$(7.93 \pm 0.03) \times 10^{-3}$
A_{ref} (ph cm^{-2} s^{-1} keV^{-1})	0.28 ± 0.02	0.30 ± 0.02	0.29 ± 0.01
A_k	$(1.2 \pm 0.1) \times 10^{-4}$	$(1.1 \pm 0.1) \times 10^{-4}$	$(1.3 \pm 0.2) \times 10^{-4}$
A_{bb}	$(2.43 \pm 0.6) \times 10^{-5}$	$(2.30 \pm 0.07) \times 10^{-5}$	$(2.51 \pm 0.20) \times 10^{-4}$
χ^2_ν	1.28	1.24	1.26

limits (see Table 6.3). This increase in flux would probably result in increased radiation pressure on the accretion disc causing an increase in the disc warp, hence resulting in the obscuration of X-ray flux from the compact source, therefore causing the anomalous low state.

The increase in radiation pressure could have resulted from increased mass accretion rate onto the compact object as a result of increased mass transfer rate from the companion star and/or increased disc viscosity. An increase in mass transfer rate in turn implies that the companion star should have overfilled its Roche-lobe. Given the duration of the anomalous low states observed in Her X-1, it is very unlikely that the companion star can overflow its Roche-lobe through the normal stellar evolution. However, the companion star can still overflow its Roche-lobe if the density of the material at the L1 point decreased as a result of increased X-ray flux heating the

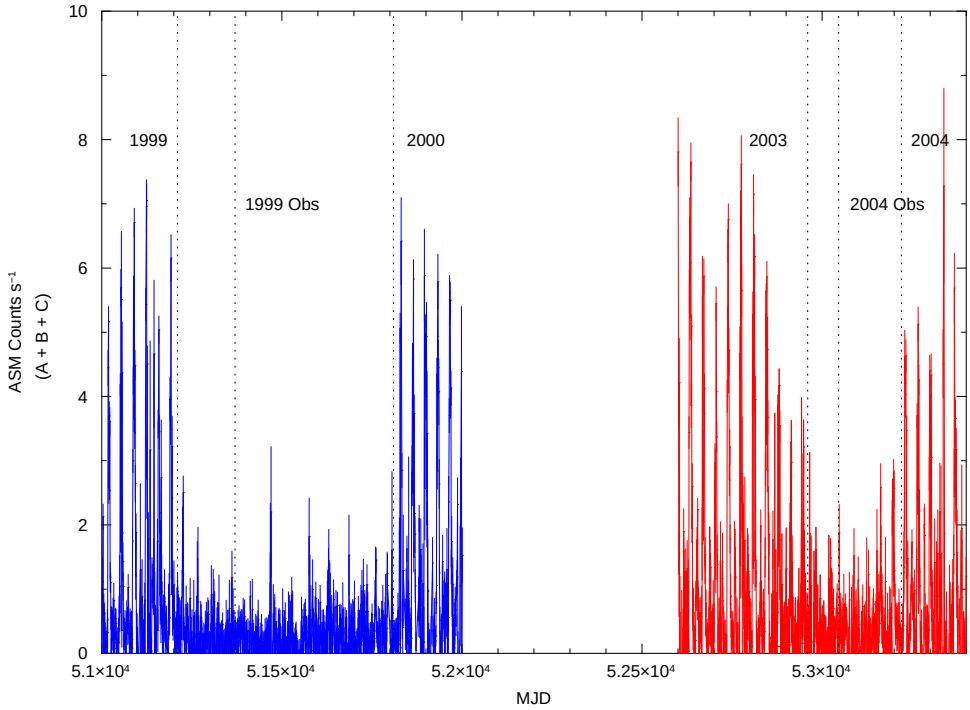

Figure 6.16: Lightcurve of Her X-1 showing the 1999 - 2000 and 2003 - 2004 anomalous low state. The vertical lines labelled "1999 obs" and "2004 obs" indicate the time when the data for analysis of these anomalous low state were collected, while the other vertical lines show the boundary of the two anomalous low states.

L1 region.

Still et al. (2001b) reported that the hidden photon flux from the neutron star at 1 keV during the 1999 - 2000 anomalous low state was $(0.9 \pm 0.09) \times 10^{-1}$ photons cm^{-2} s^{-1} keV^{-1}, suggesting that there was no significant change in the flux during the 1999 - 2000 ALS compared to the normal high state flux. This suggested that there was no significant increase in the radiation pressure. But the results obtained in this thesis indicated an increase in flux, hence increased radiation pressure. From the lightcurve shown in Figure 4.3 (see Figure 6.16 for an enlarged version) it is observed that there was a rapid drop in flux when Her X-1 entered the 1999 -

2000 anomalous low state, while the drop in flux was gradual when it entered the 2003 - 2004 anomalous low state. This could suggest that there are different mechanisms responsible for the different anomalous low states observed in Her X-1. One of the most probable mechanisms could be accretion disc torque (Ghosh & Lamb, 1978, 1979a,b and Wang, 1987).

It was also observed that the reflection component dominates the spectrum when the inner face of the companion star is facing the observer, i.e. at $\phi_{\rm orb} \sim 0.5$ (see Figures 5.6 and 5.8). This is as a result of Compton reflection from the inner face of the donor star. Although the reflection component is dominated by emission from the companion star, reflection has also been observed from other regions of the binary system, e.g. the accretion disc corona (Leahy, 1995). This reflection effect has also been observed in other X-ray sources, e.g. AGNs and stellar-mass black holes (White et al., 1988).

Chapter 7

Conclusions

Since the discovery of the 35-day cycle of Her X-1, it has entered the anomalous low state a number of times. The precession period of Her X-1 after the 2003 - 2004 anomalous low state has been re-calibrated. It was found that Her X-1 turned on after the 2003 - 2004 anomalous low state with a new precession period, i.e. $P_{35} = 34.760 \pm 0.001$ days, and main-on flux. This confirms the predictions of SB04. It was further observed that there is a positive correlation between the precession period and the main-on flux, which is a confirmation of the theoretical predictions of Wijers & Pringle (1999).

Using optical and X-ray data, the optical and X-ray lightcurves of Her X-1 were constructed. These lightcurves showed that the projected shadow of the accretion disc on the inner face of the companion star varies over the 35-day precession cycle. This is as a result of the change in the shape of the accretion disc over the 35-day period as it precesses around the neutron star, implying that the precession period is also observed in the optical wavelengths, consistent with observations of Gerend and Boynton (1976).

Comparison of the anomalous low state and normal high state lightcurves of Her X-1 have revealed that there is insignificant change in the 35-day profile of the lightcurves between these

two states of Her X-1. This suggests that the change in the disc shape between the anomalous low state and the normal high state is very small and any slight increase in the disc warp should be enough to obstruct the neutron star from the observer resulting in the anomalous low state. This would further imply that a slight increase in radiation pressure (the mechanism responsible for the warp) is sufficient to warp the disc resulting into obscuration of the neutron star.

It was shown that the X-ray emission during the anomalous low state consists of two components: reflection component from the inner face of the companion star and the coronal component from the accretion disc corona. Comparison of the anomalous low state optical and X-ray lightcurves suggest that the X-ray emission during the anomalous low state is dominated by emission from the companion star, which is also the dominant source of the optical emission from the system. Some contribution to the X-ray flux during the anomalous low state is from the accretion disc corona.

It was shown that Her X-1 was brighter by a factor of ~ 2 - 3 during the 2003 - 2004 anomalous low state compared to the normal high state brightness. This suggests an increase in the X-ray flux from the accreting neutron star, resulting in increased radiation pressure, being a possible mechanism responsible for disc warp in Her X-1.

In addition to radiation pressure being the engine behind the disc warp in Her X-1, there is a possibility that other mechanisms could cause the disc warp in Her X-1, justifying further investigation of other possible mechanisms behind the disc warp in the accretion disc in Her X-1. As already discussed, it has been observed that the anomalous low state is accompanied by a period of enhanced spin-down of the neutron star resulting from an accretion disc torque. The connection between the anomalous low state and enhanced spin-down of the com-

pact object is a very interesting phenomenon which definitely justifies an in-depth study.

References

Abraham Z., 2000, Astron. Astrophys. **355**, 915

Ann H.B., J. Korean Astron. Soc. 2007, **40**, 9

Arnorld K., Darman B., & Gordon C., 2005, An X-ray Spectral Fitting package, user Guide verson 12.2.1

Balbus S.A., & Hawley J.F., 1991, Astrophys. J. **376**, 214

Balbus S.A., & Hawley J.F., 1998, Rev Mod. Phys. **70**, 1

Balbus S.A., Hawley J.F. & Stone J.M., 1996, Astrophys. J. **467**, 76

Balucińska-Church M., Barnard R., Church M.J., et al., 2001, Astron. Astrophys. **378**, 847

Barcons X., 2003, astro-ph/0306411

Bardeen J.M., & Patterson J.A., 1975, Astrophys. J. **195**, L65

Basko M.M., & Sunyaev R.A., 1975, Astron. Astrophys. **42**, 311

Basko M.M., & Sunyaev R.A., 1976, Mon. Not. R. Astr. Soc. **175**, 396

Bate M.R., Bannell I.A., Clarke C.J., Lubow S.H., Ogilvie G.I., Pringle J.E., & Tout C.A.,2000, Mon. Not. R. Astr. Soc. **317**, 773

Beardmore A.P., Done C., Osborne J.P., & Ishida M., 1995, Mon. Not. R. Astr. Soc. **233**, 759

Beuermann K., 1988, in Polarised Radiation of Circumstellar origin, ed. G.V. Coyne, S.J.A.A Magalhães, T. Wichramasinghe (Vatican-Observatory, Vatican city), p.125

Belmont R., & Tagger M., 2005, Chin. J. Astron. Astrophys **5**, 43

Bildsten L., Chakrabarty D., Chiu J., Finger M.H., et al. 1997, Astrophys. J. Suppl. **113**, 367

Boroson B., Vrtilek S.D., Raymond J.C., & Still M., 2007, astro-ph 0705.4319

Boroson B., O'Brien K., Horne K., Kallaman T., Still M., Boyd P.T., Quaintrell H., & Vrtilek S.D., 2000, Astrophys. J. **545**, 399

Boyd P., & Still M., 2004, The Astronomer's Telegram, **228**, 1

Boyd P., Still M., & Corbet R., 2004, The Astromoner's Telegram, **307**, 1

Boynton P.E., Canterna R., Crosa L., Deeter J., & Gerend D., 1973, Astrophys. J., **186**, 617

Campbell C.G., 1997, Magnetohydrodynamics in Binary stars, Kluwer

Caproni A., & Abraham Z., 2004, Astrophys. J. **602**, 625

Caproni A., Livio M., Abraham Z., & Mosquera Cuesta H.J.M., 2006b, astro-ph/0608398

Caproni A., Abraham Z., & Mosquera Cuesta H.J., 2006a, Astrophys. J. **638**, 120

Caproni A., Abraham Z., & Mosquera Cuesta H.J., 2007, Mon. Not. R. Astr. Soc. **379**, 135

Cameron A.C., Pollacco D., Street R.A., Lister T.A., 2006, Mon. Not. R. Astr. Soc. **373**, 799

Casares J., 2005, astro-ph/0503071

Charles P.A. & Coe M.J., 2003, astro-ph/0308020v2

Cheng F.H., Vrtilek S.D., & Raymond J.C., 1995, Astrophys. J. **452**, 825

Choi C.S., Nagase F., Makino F., 2004, Astrophys. J. **437**, 449

Choi C.S., Seon K.I., Dotani T., & Nagase F., 1997, Astrophys. J. **476**, L81

Chou Y., Grindlay J.E., 2001, Astrophys. J **563**, 934

Chriatian D.J & Swank J.H., Astrophys. J. suppl. **109**, 177

Church M.J., 2001, Adv. Space Res., **2 -3**, 323

Church M.J., 2004 RevMexAA **20**, 140

Church M.J., & Balucińska-Church M., 1995, Astron. Astrophys. **300**, 441

Church M.J., & Balucińska-Church M., 2004, Mon. Not. R. Astr. Soc. **348**, 955

Church M.J., & Balucińska-Church M., Dotani T., et al., 1998, Astrophys. J. **504**, 516

Church M.J., & Balucińska-Church M., Inoue H., et al., 1997, Preceedings of an International Symposium on X-ray Astronomy ASCA Third Anniversary. eds F.Makino & M.Mitsuda, p.459

Clarkson W.I, Charles P.A., Coe M.J., et al., 2003a, Mon. Not. R.Astr. Soc. **343**, 1213

Clarkson W.I, Charles P.A., Coe M.J., & Laycock S., 2003a, Mon. Not. R.Astr. Soc. **343**, 1213

Clarkson W.I., Charles P.A., Coe M.J., Laycock S., Tout M.D., & Wilson C.A., 2003b, Mon. Not. R. Astr. Soc. **339**, 447.

Coburn W., Heindl W.A., Wilms J., Gruber D.E., et al., 2000, Astophys. J. **543**, 351

Crosa L., & Boynton P.E., 1980, Astrophys. J. **235**, 999

Dal Fuime D., Orlandini M., Cusumano G., et al, 1998, Astron. Astrophys. **329**, L41

Deeter J., Crosa L., Gerend D.,& Boynton P.E., 1976, Astrophys. J. **206**, 861

Delgado A.J., Schmidt H.U., & Thomas H.C., 1983, Astron. Astrophys. **127**, L15

Demianski M., & Inanov P.B., 1997, Astron. Astrophys. **324**, 829

den Herder J.W., Brinkman A.C., Kahn S.M., Branduardi-Raymont G., et al, 2001, Astron. Astrophys. **365**, L7

Done C., Osborne J.P., & Beardmore A.P., 1995, Mon. Not. R. Astr. Soc. *276*, 483

Doty J., 1994, The All Sky Monitor for X-ray Timing Experiments

Dove J.B., Wilms J., & Begelman M.C., 1997, Astrophys. J. **487**, 747

Elsner R.F., & Lamb F.K., 1977, Astrophys. J. **215**, 897

Endo T., Nagase F., & Muhara T., 2000, Publ. Astr. Soc. Japan **52**, 223

Fabian A.C., Vaughan S., Nandra K., Iwasawa K., Ballantyne D.R., Lee J.C., De Rosa A., Turner A., & Yong A.J., 2002, Mon. Not. R. Astr. Soc. **335**, L1

Fender R., 2003, in Compact Stellar X-ray Sources, ed. W.H.G. Lewin & M. van der Klis, Cambridge University Press

Frank J., King A.R., & Raine D., 1992, Accretion Power in Astrophysics, 2nd Edition, Cambridge University Press.

Frank J., King A.R., & Raine D., 2002, Accretion Power in Astrophysics, 3rd Edition, Cambridge University Press.

Gallimore J.F., Baum S.A., & O'Dea C.P., 2004, Astrophys. J. **613**, 794

Gansicke B.T., 1998, ASP Conference series **137**, 88

Gansicke B.T., Beuermann K., & de Martino D., 1995, Astron. Astrophys. **303**, 127

Gerend D.,& Boynton P.E., 1976, Astrophys. J. **209**, 562

Ghosh P., & Lamb F.K., 1979a, Astrophys. J. **232**, 259

Ghosh P., & Lamb F.K., 1979b, Astrophys. J. **234**, 296

Giacconi R., Gursky H., Kellogg E., Levinson R., Screier E., & Tananbaum H., 1973, Astrophys. J. **184**, 227

Giacconi R., Gursky H., Paolini F.R., & Rossi B.B., 1962, Phys. Rev. Lett. **9** 439

Goldreich P., & Tremaine S., 1978, Icarus **34**, 240

Gnedin Y.N., & Sunyaev R.A., 1974, Astron. Astrophys. **36**, 379

Grandi S.A., Hintzen P.M.N.O., Jensen I.B., et al. Astrophys. J. **190**, 365

Grimm H.-J., Gilfanov M., & Sunyaev R., 2002, Astron. Astrophys. **391**, 923

Hansinger G., & van der Klis M., 1989, Astron. Astrophys. **225**, 79

Hellier C., 2001, Cataclysmic Variables, How and why they vary, Springer-Praxis

Hirano T., Hayakawa S., Nagase F., Masai K., & Mitsuda K., 1987, Publ. Astron. Soc. Japan **39**, 619

Homer L, Charles P.A., Hakala P., Muhli P., Shih I.-C., Smale A.P., & Ramsay G., 2001, Mon. Not. R. Astr. Soc. **322**, 827

Howarth I.D., & Wilson B., 1983, Mon. Not. R. Astr. Soc. **202**, 347

Hutchings J.B., Cowley A.P., Mann R., Schmidtke P.C., & Crampton D., 2005, Astrophys. J. **130**, 210

Iben I.J., 1991, Astrophys. J. Suppl. **76**, 55

İnam S.C., & Baykal A., 2005, Mon. Not. R. Astr. Soc. **361**, 1393

Iping R.C., & Petterson J.A., 1990, Astron. Astrophys. **239**, 221

Jackson D., 1975, Classical Electrodynamics, 2nd Edition. Wiley & sons, New York

Jansen F., Lumb D., Altieri B., Clavel J., et al., 2001, Astron. Astrophys. **365**, L1

Jimenez-Garate M.A., Raymond J.C., Liedahl D.A., & Hailey C.J., 2005 **625**, 931

Jones C., & Forman W., 1976, Astrophys. J. **209**, L131

Joss P.C., & Rappaport S.A., 1979, Astron. Astrophys. **71**, 217

Joss P.C., & Rappaport S.A., 1984, Ann. Rev. Aston. Astrophys. **22**, 537

Kane S R., Collier Cameron A., Horne K., et al., 2004, Mon. Not. R. Astr. Soc. **353**, 689

Katz J.I., 1973, Nature Phys. Sci. **246**, 87

Katz J.I., 1980., Astrophys. J. **236**, L127

Katz J.I., Anderson S.F., Grandi S.A., & Margan B., 1982, **260**, 780

King A.R., 1988, Mon. Not. R. Astr. Soc. **29**, Astron. lett. **32** 804

Kippenhahm R., & Weigert A., 1990, Stellar Structure and Evolution, Spring-Verlgat, Berlin

Klochkov D., Shakura N., Postnov K., Staubert K., & Wilms J., 2006, astro-ph/0612790

Klochkov D., Staubert R., Tsygankov S., Lutovinov A., et al., 2007, astro-ph 0704.3062

Kryskenbohm I., 2004, PhD. Thesis

Krolik J.H., 1999, Active Galactic Nuclei, Princeton University Press

Kuijer J., & Pringle J.E., 1982, Astron. Astrophys. **114**, L4

Kumar S., 1986, in Theory of Accretion Discs, ed. F. Meyer, W. Duschl, J. Frank & E. Meyer-Hofmeister, 173

Kuster M., Wilms J., Stanbert R., Heindl W.A., Rothschild R.E., Shakura N.I., & Postnov K.A., 2005, Astron. Astrophys. **443**, 753

Kuulkers E., van der Klis M., & Vaughan B.A., 1996, Astron. Astrophys. **311**, 197

Kong A.K.H., Charles P.A., Kuulers E., 1998, NewA **3**, 301

Lachowicz P., Zdziaski A.A., Schwarzenberg-Czerny A., Boley G.G., & Kitamoto S., 2006, astro-ph/0508306

Lai D., 1999, Astrophys. J. **524**, 1030

Lai D., 2003, Astrophys. J. **591**, L119

Lang F.L., Levine A.M., Bautz M., Hauskins S., et al., 1981, Astrophys. J. **246**, L21

Lampton M., Margan B., & Bowyer S., 1976, Astrophys. J., **208**, 177

Larwood J.D., 1997, Mon. Not. R. Astr. Soc. **290**, 490

Larwood J.D., 1998, Mon. Not. R. Astr. Soc. **299**, 32

Larwood J.D., Nelson R.P., Papaloizou J.C.B., & Terquem C., 1996, Mon. Not. R. Astr. Soc. **282**, 597

Lasota J.P., Abramowicz M.A., Chen X., Krolik J., Narayan R., & Yi I., 1996, Astrophys. J. **462**, 142

Lavagetto G., Iaria R., D'Ai A., Di Salvo T., & Robba N.R., 2007, astro-ph 0710.4934

Leahy D.A., 1995, Astron. Astrophys. **113**, 21

Leahy D.A., 2001, Astrophys. J. **547**, 449

Leahy D.A., & Marshall H., 1999, Astrophys. J. **521**, 328

Leahy D.A., & Matsuoka M., 1989, ESASP **296**, 493

Leahy D.A., & Scott D.M., 1998, Astrophys. J. **503**, L63

Leahy D.A., & Yoshida A., 1995, Mon. Not. R. Astr. Soc. **276**, 607

Levine A., Bradt H., Cui W., Jernigan J., Morgan E., Remillard R., Shirley R & Smith D., 1996, Astrophys. J. **469**, L33

Levine A.M., 1999, IAU Circ. **7139**, 2 ed. Green D.W.

Levine A.M., & Jernigan J.G., 1982, Astrophys. J. **262**, 294

Lewin W.G.H., van Paradijs J., & Taam R.E 1993, Space Sci.Rev. **62** 223

Lewin W.G.H., van Paradijs J., & van den Heuvel J.P., 1995, X-ray Binaries, Cambridge Astrophysics Series, Cambridge M.A (Cambridge University Press)

Li J., & Wickramasinghe D.T., 1998, Mon. Not. R. Astr. Soc. **300**, 1015

Li X-D., 2003, IAU 8th Asia-Pacific Regional Meeting, ASP Conference series, **289**, 289: eds. S. Ikeuchi., J. Hearnshaw., & T. Hanawa

Lin D.N.C., & Papaloizou J.C.B., 1993, in Protostars and Planets III, ed. E.H. Levy, & J. Lunine Univ. Arizana Press, Tucson 749

Liu B.F., & Mineshige S., 2002, Astr. Soc. Japan **391**, 391

Liu Q.Z., van Paradijs J., & van den Heuvels E.P.J., 2007a, Astron. Astrophys. **469**, 807

Liu Q.Z., van Paradijs J., & van den Heuvels E.P.J., 2007b, Astron. Astrophys. **455**, 1165

Liu Q.Z., van Paradijs J., & van den Heuvels E.P.J., 2005, Astron. Astrophys. **442**, 1135

Longair M.S., 1992, High Energy Astrophysics Vol. 1, Cambridge University Press, Cambridge

Longair M.S., 1994, High Energy Astrophysics Vol. 2, Cambridge University Press, Cambridge

Lubow S.H., Ogilvie G.I., & Pringle J.E., 2002, Mon. Not. R. Astr. Soc. **337**, 706

Lubow S.H., & Shu F.N., 1975, Astrophys. J. **198**, 383

Lynden-Bell D., & Pringle J.E., 1974, Mon. Not. R. Astr. Soc. **168**, 603

Manchanda R.K 1977 Astrophys. Space Sci. **50**, 179

Margon B., 1984, Ann. Rev. Astron. Astrophys. **22**, 507

Margon B., Deutsch E.W., Leinhardt Z.M., & Anderson S.F 1999, IAU Circ., 7144

Malony P.R., & Begelman M.C., 1997, Astrophys. J. **491** L43

Malony P.R., Begelman M.C., & Nowak M.A., 1998, Astrophys. J. **504**, 77

Malony P.R., Begelman M.C., & Pringle J.E., 1996, Astrophys. J. **472**, 582

Margon B., 1984, ARA&A 22, 504

Markovic D., & Lamb F.K., 1998, Astrophys. J. **507**, 318

Martin R.G., Pringle J.E., & Tout C.A., 2007, astro-ph 0708.2034

McMcray R.A., Shull J.M., Boynton P.E., et al., 1982, Astrophys. J. **43**, 504

Merloni A., & Fabian C., 2001, Mon. Not. R. Astr. Soc. **321**, 549

Mestel L., & Spruit H.C., 1987, Mon. Not. R. Astr. Soc. **226**, 57

Middleditch J., & Nelson J., 1976, Astrophys. J. **208**, 567

Miller K.A., & Stone J.M., 2000, Astrophys. J. **534**, 398

Mihara T., Ohashi T., Makishima K., Nagase F., Kitamoto S., & Koyama K., 1991, Publ. Astr. Soc Japan **43**, 501

Mihara T., & Soong Y., 1994, in Proc. of the New Horizon of X-ray Astronomy, ed. Makino, University Academy press, Tokyo, 419

Mironov A.V., Moshkalev V.G., & Trunkovskii E.M., et al., 1984, Sov. Astron. **30**, 68

Miyoshi M., Moran J., Herrnstein J., Greenhill L et al., 1995, Nature **373**, 127

Monet D G., Levine S.E., Canzian B., et al., 2003, Astron J. **125**, 984

Murray J.R., Chakrabarty D., Wynn G.A., et al., 2002, Mon. Not. R. Astr. Soc. **335**, 247

Nagase F., 1989, Publ. Astron. Soc. Japan **41**, 1

Nelemans G., Jonker P.G., Marsh T.R., et al., 2003, Mon. Not. R. Astr. Soc. **348**, L7

Newman J.A., Eracleous M., Filippenko A.V., Halpern J.P., 1997, Astrophys. J. **485**, 570

Norton A.J., Wheatley P.J., West R.G., & Haswell C.A, 2007, Astron. Astrophys. **467**, 785

Ögelman H., 1987, Astron. Astrophys. **172**, 79

Ögelman H., & Trümper J., 1988, Mem S.A. Italiana 59, 169

Ogilvie G.I.,& Dubus G., 2001, Mon. Not. R. Astr. Soc. **320**,485

Ohashi T., Inoue H., Kawai N., et al 1984, PASJ 36, 719

Oosterbreok T., Parmar A.N., Martin D.D.E., & Lammers U., 1997, Astron. Astrophys. **327**, 215

Oosterbreok T., Parmar A.N., Dal Fiume D., Orlandini M., Santangelo A., & Del Sordo S., 2000, Astron. Astrophys. **353**, 575

Oosterbreok T., Parmar A.N., Orlandini M., Segreto A., Santangelo A., & Del Sordo S., 2001, Astron. Astrophys. **375**, 922

Paczyński B., 1976, in Structure and Evolution of Close Binary Systems, IAU Symp. eds. P.Eggleton, S. Milton, J. Whelan, Reidel, p.75

Paczyński B., 1977, Astrophys. J. **216**, 822

Padsiadlowiski Ph., Rappaport S., & Pfahl E.D., 2002 Astrophys. J. **565**, 1107

Papaloizou J.C.B., & Lin D.N.C., 1995, Astrophys. J. **438**, 841

Papaloizou J.C.B., & Pringle J.E., 1977, Astrophys. J. **438**, 841

Papaloizou J.C.B., & Pringle J.E., 1983, Mon. Not. R. Astr. Soc. **202**, 1181

Papaloizou J.C.B., & Terquem C., 1995, Mon. Not. R. Astr. Soc. **274**, 987

Parmar A.N., Oosterbroek T., Dal Fiume D., Orlandini M., Santangelo A., Segreto A., & Del Sordo S., 1999, Astron. Astrophys. **350**, L5

Parmar A.N., Pietsch W., McKechnie S., White N.E., Trümper J., Voges W., & Barr P., 1985, Nut. 313 119

Parmar A.N., Sanford P.W., & Fabian A.C 1980, Mon. Not. R. Astr. Soc. **192**, 311

Parmar A.N., & White N.E., 1988, Mem. Astron. Soc. It **59** 147

Paul B., Kitamoto S., & Makino F., 2000, Astrophys. J. **528**, 410

Petterson J., 1977, Astrophys. J. **218**, 783

Pollacco D.L., Skillen I., Cameron A.C., Christian D.J., et al., 2006, Publ. Astr. Soc. Pac. **118**, 1407

Pravdo S.H., Becker R.H., Bussard R.W. et al, 1979 in X-ray Astronomy, eds W.A. Baily, & L.E. Peterson, IAU/COSPAR, p.219

Pravdo S.H., Boldt E.A., Holt S.S., et al., 1978, Astrophys. J. Letter **215**, L61

Prendergast H.K., & Burbidge G.R., 1968, Astrophys. J. **151**, L83

Priedhorsky W.C., & Holt S.S., 1987, Space Sci. Rev. 45, 291

Priedhorsky W.C., & Terrel J., 1984, Astrophys. J. **284**, L17

Pringle J.E., 1992, Mon. Not. R. Astr. Soc. **258**, 811

Pringle J.E., 1996, Mon. Not. R. Astr. Soc. **281**, 357

Pringle J.E., 1997, Mon. Not. R. Astr. Soc. **292**, 136

Pringle J.E., & Rees M.J., 1972, Astron. Astrophys. **21**, 1

Ramsay G., Zane S., Jimenez-Garate M.A. Mario A., den Herder J.-W., & Hailey C.J., 2002, Mon. Not. R. Astr. Soc. **337**, 1185

Reig P., & Roche P., 1999, Mon. Not. R. Astr. Soc. **306**, 100

Reipurth B., & Bally J., 2001, ARA&A 39, 403

Reynolds A.P., Quaintrell H., Still M.D., Roche P., Chakrabarty D., & Levine S.E., 1997, Mon. Not. R. Astr. Soc. **288**, 43

Ricketts M.J., 1982, in Accreting Neutron stars, ed. W.Brinkmann & J. Trümper, 100

Rybicki G.B., & Lightmann A.P., 1979, Radiative Processes in Astrophysics, John Wiley, New York.

Roberts W.J., 1974, Astrophys. J. **187**, 575

Różańska A., Sobolewska M., & Czerny B., 2007, Mem S.A.It **78**, 390

Santangelo A., Del Sordo S., Piraino S., et al 1998, Nuclear Phys. B (Proc. suppl) **69**, 151

Sato N., Nagase F., Kawai N. et al, 1986, Publ. Astr. Soc. Japan, **38**, 731

Sarty G.E., Kiss László E., Johnston H.M., et al 2007, JAAVSO Volume 35

Schandl S., 1996, Astron. Astrophys. **307**, 95

Schandl S., & Meyer F., 1994, Astron. Astrophys. **289**, 146

Scheuer P.A.G., & Feiler R., 1996, Mon. Not. R. Astr. Soc. **282**, 291

Scott D.M., Leahy D.A.,& Wilson R.B., 2000, Astrophys. J. **539**, 392

Scott D.M., & Leahy 1999, Astrophys. J. **510**, 974

Shakura N.I., Prokhorov M.E., Postnov K.A., & Ketsaris N.A., 1999, Astron. Astrophys. **348**, 917

Shakura N.I., & Sunyaev R.A., 1973, Astron. Astrophys. **24**, 337

Shirakawa A., & Lai D., 2002a, Astrophys. J. **564**, 361

Shirakawa A., & Lai D., 2002b, Astrophys. J. **565**, 1134

Sillanpää A., Haarala S., Valtonen M.J., Sundelius B., & Boyrd G.G., 1988, Astrophys. J. **325**, 628

Smale A.P., & Lochner J., 1992, Astrophys. J. **395**, 582

Soong Y., Gruber D.E., Petterson L.E., & Rothschild R.E., 1990, Astrophys. J. **348**, 634

Spruit H.C., 2002, in The Neutron Star-Black hole connection, NATO ASI Elounda Vol. 567, ed. C. Houveliotou, J.E. Ventura & E.P. van den Heuvel, Springer

Stella L., & Vietri M., 1998, Astrophys. J. **492**, L59

Staubert R., Schandl S., Klochkov D., Wilms J., Postnov K., & Shakura N.I., 2007, astro-ph 0702528

Still M., & Boyd P., 2004, Astrophys. J. **606**, L135

Still M., O'Brein K., Horne K., Hudson D., Boroson B., Vrtilek S.D., Quaintrell H., & Fieder H., 2001a, Astrophys. J. **553**, 776

Still M., O'Brein K., Horne K., Boroson B., Titarchuk L.G., Engle K., Vrtilek S.D., Quaintrell H., & Fieder H., 2001b, Astrophys. J. **554**, 352

Storchi-Bergmann T., Nemman Da Silva R., Eracleous M., Halpern J.P., et al., 2003, Astrophys. J. **598**, 956

Strüder L., Briel U., Denmerl K., Hartmann R., et al., 2001, Astron. Astrophys. **365**, L18

Swank J.H., Jahoda K., Zhang W., Giles A.B., et al, 1995, in The Lives of Neutron Stars, eds. M.A. Alpar, U. Kiziloglu, J. van Paradijs, Kluwer Academic, p.525

Tananbaum H., Gursky H., Kellogg E.M., Levinson R., Schreier E., & Giacconi R., 1972, Astrophys. J. **174** L143

Terquem C., Eislöffel J., Paploizou J.C.B., & Nelson R.P., 1999, Astrophys. J. **512**, L131

Terquem C., & Paploizou J.C.B., 2000, Astron. Astrophys. **360**, 1031

Terquem C., Papaloizou J.C.B., & Nelson R.P., 1999, ASP Conference Series, 160, 71

Trowbridge S., Nowak M.A., & Wilms J, 2007, astro-ph 0708.0038

Trümper J., Kahabka P., Oegelman H., Pietsch W., & Voges W., 1986, Astrophys. J. **300**, L63

Trümper J., Pietsch W., Reppin C., et al., 1977, MitAG **42**, 120

Trümper J., Pietsch W., Reppin C., et al., 1978, Astrophys. J., **219**, L105

Tuner M.J.L., Abbey A., Arnaud M. Balasini M., et al, 2001, Astron. Astrophys. **365**, L27

van Allen J.A., Mcllwain C.E., & Ludwig G.H., 1959, J. Geophys. Rev. **64**, 271

van den Hauvel E.P.J., 1977, Ann. NY. Acad. Sci., **302**, 14

van den Hauvel E.P.J., Ostriker P.J., & Petterson J.A., 1980, Astron. Astrophys. **81**, 17

van Paradijs J., & MeClintock J.E., 1995, in X-ray Binaries, eds. W.H.G. Lewin, J. van Paradijs, & E.P.J. van Heuvel, Cambridge University Press, p.58

van Straaten S., van der Klis M., & Méndez M., 2003, Astrophys. J. **596**, 1155

Verbunt F., 1982, Space Sci. Rev. **32**, 379

Verbunt F., 1993, Ann. Rev. Astron. Astrophys. **31** 93

Vrtilek S.D., Mihara T., Primini F.A., Kahabka P., et al., 1994, Astrophys. J. **436**, L9

Vrtilek S.D., Quaintrell H., Boroson B., Still M., Fieder H., O'Brien K., & McCray R., 2001, Astrophys. J. **549**, 522

Wang Y.M., 1987, Astron. Astrophys. **183**, 257

Warner, B. 1995, Cataclysmic variable stars, Cambridge University Press

Wehlau A., Nemec J.M., Hanlan P., & Rich R.M., 1992, Astrophys. J. **103**, 1583

White N.E., Nagase F., & Parmar A.N., 1995, in X-ray Binaries (Cambridge Astrophysical series, Cambridge M.A): edited Lewin, Walter H.G., van Paradijs Jan. & van den Heuvel, Edward P.J., p1-57, Cambridge University Press

White N.E., Stella L., & Parmar A.N., 1988, Astrophys. J. **324**

White N.E., & Swank J.H., 1982, Astrophys. J. **253**, L61

White N.E., Swank J.H., & Holt S.S., 1983, Astrophys. J. **270**, 711

Wijers R.A.M., Pringle J.E., 1999, Mon. Not. R. Astr. Soc. **308**, 207

Wojdowski P.S., Woo J.W., Zhang S.N., 1998, Astrophys. J. **502**, 253

Wilkins D.C., 1972, Phys. Rev D. 5, 814

Wilms D.A., Enoch B., Christian D.J., et al., 2006, astro-ph/0607591

Wilms J., Nowak M.A., Dove J.B., Fender R.P., & di Matteo T., 1999, Astrophys. J. **522**, 460

Zane S., Ramsay G., Jimenez-Garate M.A., den Herder J.W., Still M., & Boyd P.T., 2005, asto-ph/0503240

Zdziarski A.A., 1999, High Energy Processes in Accreting Black holes, ASP Conference series, Vol 161, ed. J. Poutanen & R. Svenssin p.16

Zhang F., Li X.D., & Wang Z.R., 2004, Chin. J. Astron. Astrophys. **4**, 320

Ziolkowski J., 2002, astro-ph/0208455